

Microfabricated Surface Trap and Cavity Integration for Trapped Ion Quantum Computing

by

Andre J. S. Van Rynbach

Department of Electrical and Computer Engineering
Duke University

Date: _____
Approved:

Jungsang Kim, Supervisor

David J. Brady

John E. Thomas

Michael Gehm

Peter Maunz

Dissertation submitted in partial fulfillment of the requirements for the degree of
Doctor of Philosophy in the Department of Electrical and Computer Engineering
in the Graduate School of Duke University
2016

ABSTRACT

Microfabricated Surface Trap and Cavity Integration for Trapped Ion Quantum Computing

by

Andre J. S. Van Rynbach

Department of Electrical and Computer Engineering
Duke University

Date: _____

Approved:

Jungsang Kim, Supervisor

David J. Brady

John E. Thomas

Michael Gehm

Peter Maunz

An abstract of a dissertation submitted in partial fulfillment of the requirements for
the degree of Doctor of Philosophy in the Department of Electrical and Computer
Engineering
in the Graduate School of Duke University
2016

Copyright © 2016 by Andre J. S. Van Rynbach
All rights reserved except the rights granted by the
Creative Commons Attribution-Noncommercial Licence

Abstract

Atomic ions trapped in microfabricated surface traps can be utilized as a physical platform with which to build a quantum computer. They possess many of the desirable characteristics of such a device, including high fidelity state preparation and readout, universal logic gates, and long coherence times, and can be readily entangled with each other through photonic interconnects. The use of optical cavities integrated with trapped ion qubits as a photonic interface presents the possibility for order of magnitude improvements in performance in several key areas for their use in quantum computation. The first part of this thesis describes the design and fabrication of a novel surface trap for integration with an optical cavity. The trap is custom made on a highly reflective mirror surface and includes the capability of moving the ion trap location along all three trap axes with nanometer scale precision. The second part of this thesis demonstrates the suitability of small microcavities formed from laser ablated, fused silica substrates with radii of curvature in the 300-500 μm range for use with the mirror trap as part of an integrated ion trap cavity system. Quantum computing applications for such a system include dramatic improvements in the photon entanglement rate of up to 10 kHz, the qubit measurement time down to 1 μs , and the qubit measurement error rate down to the 10^{-5} range. The final part of this thesis describes a performance simulator for exploring the physical resource requirements and performance demands to scale a quantum computer to sizes capable of implementing quantum algorithms beyond the limits of classical computation.

To my wife, Cara, and my family: Mom, Dad, Georgine, and Chris.

Contents

| | |
|---|-------------|
| Abstract | iv |
| List of Tables | ix |
| List of Figures | x |
| List of Abbreviations and Symbols | xiv |
| Acknowledgements | xvii |
| 1 Introduction | 1 |
| 1.1 Quantum Computing with Trapped Ions | 4 |
| 1.2 Optical Cavities and Ion Trapping | 6 |
| 1.3 Quantum Computer Performance Simulation | 7 |
| 1.4 Thesis Organization and Summary of My Contributions | 8 |
| 2 Ion Trap Experimental Setup | 11 |
| 2.1 Introduction | 11 |
| 2.2 Atomic Structure | 11 |
| 2.3 Ion Trap Working Principles | 14 |
| 2.4 Surface Trap Design and Fabrication | 17 |
| 2.4.1 Trap Simulations | 25 |
| 2.4.2 Helical Resonator | 26 |
| 2.5 Ion Trap Infrastructure | 30 |
| 2.5.1 Lasers | 30 |

| | | |
|----------|--|-----------|
| 2.5.2 | Vacuum Assembly | 34 |
| 2.5.3 | Optical Imaging Designs | 38 |
| 3 | Laser Cooling of Trapped Ions in a Standing Wave | 40 |
| 3.1 | Experiment Background | 40 |
| 3.2 | System Design | 42 |
| 3.3 | Precise Measurements of the Ion Micromotion | 46 |
| 3.4 | Measuring the Ion Position in a Standing Wave | 52 |
| 3.5 | Charging Effects of the Mirror Surface | 65 |
| 3.6 | Ion Trap Outlook and Summary | 67 |
| 4 | Cavity Theory and Simulations | 69 |
| 4.1 | Integrated Ion Trap and Optical Cavity Design | 69 |
| 4.2 | Improved Collection of Photons | 74 |
| 4.3 | High Fidelity, Ultra-Fast State Readout | 84 |
| 4.4 | Summary of the Cavity Design | 87 |
| 5 | Cavity Testing and Characterization | 88 |
| 5.1 | Introduction | 88 |
| 5.2 | Super-Polished Mirror Measurements and Initial System Design . . . | 89 |
| 5.3 | Micromirror Laser Ablation | 92 |
| 5.4 | Cavity Optomechanical Design | 98 |
| 5.5 | Cavity Optical Modes | 100 |
| 5.6 | Multiscale Optical Simulations | 104 |
| 5.7 | Finesse Measurements and Simulations | 107 |
| 5.8 | Cavity Stability and Active Feedback Lock | 111 |
| 5.8.1 | Pound-Drever-Hall Technique | 114 |
| 5.8.2 | Digital Controller | 116 |

| | | |
|----------|---|------------|
| 5.9 | Cavity Stabilization Results | 117 |
| 5.10 | Fiber Coupling | 119 |
| 6 | Quantum Performance Simulator | 122 |
| 6.1 | QUIPSIM Overview | 124 |
| 6.1.1 | Fault Path Counter | 127 |
| 6.1.2 | Performance Simulation | 129 |
| 6.2 | Implementation of Quantum Operations | 130 |
| 6.2.1 | Single Qubit Gates | 131 |
| 6.2.2 | Two Qubit (CNOT) Gate | 132 |
| 6.2.3 | Cat State Preparation | 132 |
| 6.2.4 | State Preparation and Qubit Measurement | 133 |
| 6.2.5 | Error Correction | 137 |
| 6.2.6 | Fault Tolerant Toffoli Gate | 138 |
| 6.3 | Quantum Adder Circuits | 141 |
| 6.4 | Performance Evaluation | 142 |
| 6.5 | Summary of the Performance Simulator | 143 |
| 7 | Conclusions and Outlook | 146 |
| A | Digital PI Filter Code | 150 |
| | Bibliography | 152 |
| | Biography | 160 |

List of Tables

| | | |
|-----|--|-----|
| 4.1 | A summary of the relevant cavity parameters for our microcavity design. | 84 |
| 6.1 | A summary of the error rates for common FT operations performed in QUIPSIM. | 140 |

List of Figures

| | | |
|------|---|----|
| 2.1 | Energy level diagrams of $^{174}\text{Yb}^+$ and $^{171}\text{Yb}^+$ | 13 |
| 2.2 | The photolithography mask used in the mirror trap fabrication. | 17 |
| 2.3 | SEM and microscope pictures of the mirror trap. | 21 |
| 2.4 | A picture showing the packaged mirror trap on the CPGA. | 25 |
| 2.5 | Contour plots showing the electric potential from the RF and DC fields. . | 27 |
| 2.6 | A picture taken in the clean room when the vacuum chamber was opened for installing a new trap. | 28 |
| 2.7 | A picture of the outer copper shield and inner copper coil of the helical resonator. | 30 |
| 2.8 | The external cavity diode laser used for the 370 nm wavelength laser. . | 32 |
| 2.9 | A diagram of the hollow cathode lamp setup. | 34 |
| 2.10 | 399 nm spectroscopy for photoionization of Yb. | 35 |
| 2.11 | Pressure log for pumping the ion trapping chamber down to UHV low pressures. | 37 |
| 2.12 | Pictures of the ion trapping experimental setup. | 38 |
| 2.13 | Simulations using Zemax software of the imaging system used for imaging the ion onto a camera or PMT. | 39 |
| 3.1 | The ADA4870 evaluation board used to drive the tweaker electrode voltage. | 44 |
| 3.2 | Measurement of the tweaker electrode voltage. | 46 |
| 3.3 | A photon correlation histogram used to detect ion micromotion along the y-axis. | 48 |

| | | |
|------|--|----|
| 3.4 | Micromotion minimization using the parametric excitation method. | 50 |
| 3.5 | Simulations of the excess micromotion amplitude from displacing the ion using the DC electrodes without adjusting the RF null position. | 53 |
| 3.6 | A schematic of the standing wave experimental configuration. | 54 |
| 3.7 | The standing wave beam profile with Gaussian fits indicating a waist of $4.2 \mu\text{m}$ in the horizontal direction and $4.8 \mu\text{m}$ in the vertical direction. | 56 |
| 3.8 | A schematic of the convolution of the ion's motion, modeled with the function $r(z')$, with the spatially varying intensity field of the standing wave. | 57 |
| 3.9 | The sine fit to the tweaker voltage scan data for varying input attenuation power. | 59 |
| 3.10 | The measured photon counts from an ion near the standing wave node as a function of laser detuning, with fit curves found from the empirical model for several micromotion amplitudes. | 61 |
| 3.11 | The measured ion scattering rate as a function of laser detuning at the node and antinode. | 62 |
| 3.12 | The average photon scattering rate for various exposure times to the standing wave. | 63 |
| 3.13 | The ion scattering rate in a -20 MHz detuned standing wave as a function of the tweaker voltage with a convolution fit of the micromotion. | 64 |
| 3.14 | The charging rate of the mirror trap as a function of incident laser intensity. | 66 |
| 4.1 | A schematic of the hemispherical cavity showing the ion trap and cavity arrangement. | 78 |
| 4.2 | The beam size on the flat mirror w_0 and on the curved mirror w_1 as a function of cavity length for a $R = 365 \mu\text{m}$ cavity. | 79 |
| 4.3 | Simulation results for a $R = 5 \text{ mm}$ cavity. | 80 |
| 4.4 | Simulation results for $R = 300 - 600 \mu\text{m}$ micromirror cavities. | 81 |
| 4.5 | The effects of clipping loss on P_{extr} | 83 |
| 4.6 | The cavity state detection simulation results. | 86 |
| 5.1 | A microscope image of one of the substrates containing ablation spots. | 95 |

| | | |
|------|---|-----|
| 5.2 | Laser ablation spot characterization with the Zygo profilometer. | 97 |
| 5.3 | A computer rendering of the optomechanical setup for the cavity assembly. | 99 |
| 5.4 | A picture of the experimental setup used for testing the cavity. | 100 |
| 5.5 | The power spectral density of the noise vibrations of the cavity mounting structure. | 101 |
| 5.6 | Transverse mode frequencies of the cavity. | 102 |
| 5.7 | Images from a beam profiler showing the beam shape of the cavity mode. | 102 |
| 5.8 | Measurements of the cavity beam size as a function of distance with corresponding fits to an ideal Gaussian beam. | 103 |
| 5.9 | The lowest order cavity eigenmode can be found by repeated iteration of a plane wave through the cavity using the Fresnel propagator and the curved mirror propagator found from the profilometer measurements. | 106 |
| 5.10 | The cavity mode size found from the simulations is compared with an ideal Gaussian beam solution. | 108 |
| 5.11 | The measured intensity distribution of the cavity mode on the beam profiler compared with the intensity distribution found from the simulations. | 108 |
| 5.12 | The transmission signal used to calculate the finesse by scanning the cavity length. | 110 |
| 5.13 | Measured data of the cavity finesse as a function of length for three mirrors from the first batch of samples coated. | 112 |
| 5.14 | Measured data of the finesse as a function of cavity length for a micromirror from the second coating run. | 112 |
| 5.15 | Schematic of the optical and electronic system used for locking the micromirror cavities. | 113 |
| 5.16 | The error signal from the PDH technique. | 115 |
| 5.17 | The gain of the high voltage DAC output as a function of frequency. . | 117 |
| 5.18 | The integrated FPGA, DAC, ADC, and high voltage amplifier circuit board used to implement a digital control lock for the cavity. | 118 |

| | | |
|------|---|-----|
| 5.19 | The cavity lock performance in units of fluctuation distance and linewidth (κ) monitored over a period of several minutes. | 119 |
| 5.20 | The frequency spectrum of the noise on the cavity feedback signal. . . | 120 |
| 6.1 | Example run of the fault path counter for the Steane error correction block. | 129 |
| 6.2 | Code organization for the QUIPSIM program. | 130 |
| 6.3 | Preparation of a cat state with an example of error propagation through the circuit. | 133 |
| 6.4 | FT measurement of the $g_2 = IXIXIXX$ stabilizer of the Steane code using a 4- qubit cat state. | 134 |
| 6.5 | Typical state measurement in the Z basis. | 136 |
| 6.6 | Fault tolerant circuit for the Toffoli gate. | 140 |
| 6.7 | Logical error probability of the FT Toffoli gate as a function of the physical error probability. | 141 |
| 6.8 | Simulation results of QRCA and QCLA circuits. | 143 |
| 6.9 | The overall adder failure probability for various physical error probability levels as a function of adder size for FT QCLA. | 144 |

List of Abbreviations and Symbols

Symbols

| | |
|---------------|----------------------------|
| \mathcal{F} | Finesse |
| \mathcal{L} | Total mirror losses |
| T_i | Transmission of mirror i |
| L_i | Losses of mirror i |
| ν_f | Cavity free spectral range |
| $\delta\nu$ | Cavity linewidth |

Abbreviations

| | |
|------|-----------------------------|
| AC | Alternating Current |
| ADC | Analog to Digital Converter |
| AR | Anti reflection |
| Au | Gold |
| CAD | Computer Aided Design |
| CCD | Charge Coupled Device |
| CPGA | Ceramic Pin Grid Array |
| CPO | Charged Particle Optics |
| CW | Continuous Wave |
| DAC | Digital to Analog Converter |
| DC | Direct Current |

| | |
|--------|--|
| DDS | Direct Digital Synthesizer |
| ECDL | External Cavity Diode Laser |
| ELU | Elementary Logic Unit |
| EM | Electromagnetic |
| EMM | Excess Micromotion |
| FFP | Fiber Fabry Perot |
| FPC | Fault Path Counter |
| FPGA | Field Programmable Gate Array |
| FT | Fault Tolerant |
| HCL | Hollow Cathode Lamp |
| HDL | Hardware Description Language |
| HR | Highly Reflective |
| IPA | Isopropyl Alcohol |
| ME | Modular Exponentiation |
| MIST | Multi-functional Integrated Systems Technology |
| NA | Numerical Aperture |
| NEG | Non-Evaporable Getter |
| NV | Nitrogen Vacancy |
| OP AMP | Operational Amplifier |
| PCB | Printed Circuit Board |
| PDH | Pound Drever Hall |
| PI | Proportional Integral |
| QC | Quantum Computation |
| QCLA | Quantum Carry Look-ahead Adder |
| QECC | Quantum Error Correcting Code |
| QED | Quantum Electrodynamics |

| | |
|---------|-------------------------------|
| QFT | Quantum Fourier Transform |
| QI | Quantum Information |
| QRCA | Quantum Ripple Carry Adder |
| QUIPSIM | Quantum Performance Simulator |
| RAM | Random Access Memory |
| Rb | Rubidium |
| RF | Radio Frequency |
| RoC | Radius of Curvature |
| RWA | Rotating Wave Approximation |
| SEM | Scanning Electron Microscope |
| SM | Single Mode |
| SMIF | Shared Multi User Facility |
| SNR | Signal to Noise |
| SW | Standing Wave |
| TCE | Trichloroethylene |
| TEC | Thermo Electric Cooler |
| TEM | Transverse Electro Magnetic |
| Ti | Titanium |
| TiSub | Titanium Sublimation |
| TLE | Two Level Emitter |
| UHV | Ultra High Vacuum |
| UV | Ultra Violet |
| Yb | Ytterbium |

Acknowledgements

The journey in pursuit of a Ph.D., which has culminated in the writing of this thesis, has been one filled with many ups and downs, straight paths and forks in the road, and triumphs and struggles. I can say wholeheartedly it was well worth all the effort. I am grateful for all the people who helped me get to this point, as it was by no means a solo journey. Firstly, I would like to thank my advisor, Professor Jungsang Kim. His steadfast determination and passion for quantum information science has inspired me over the course of my research to push the boundaries of what is thought possible. Although I am grateful for the many equations and useful facts I learned from him, I am most grateful to him for teaching me the right way to be an engineer and scientist. This is a skill I will carry with me the rest of my career.

Much of my learning during my time at Duke has come from my fantastic lab mates, especially those that entered the lab at the same time I did, Stephen Crain and Daniel Gaultney. I truly appreciate the time they both took out of their work to help me with whatever questions I had. I was fortunate to work with some other excellent students, including Emily Mount, who among other things taught me the importance of attention to detail, Rachel Noek, whose early work set the foundations for the cavity trap project which became the main topic of my thesis, and Muhammad Ahsan, with whom I worked closely on the computer science aspect of quantum computing. I would like to thank Dr. Peter Maunz whose tremendous ion trapping experience and patience for teaching offered me invaluable guidance

during the course of this research. I also appreciate the opportunity to work with other great MIST lab members, including Dr. Geert Vrijsen, Dr. Byeong-Hyeon Ahn, Tripp Spivey, Clinton Cahall, Chao Fang, and Yuhi Aikyo. I want to especially thank Richard Nappi of the Duke Physics machine shop for his advice and invaluable help with the many parts I machined over the years. I want to thank those friends and colleagues from my time at UC Santa Barbara, especially Dr. Simon Trebst.

This thesis would not have been possible without the overwhelming support of my family. I am grateful to my Dad, for his guidance and unwavering support through all the trying times of this journey; to my Mom, who gave me my love for science and inquisitive nature; to my sister, Georgine, who is a great role model I could always look up to; and to my brother, Chris, for being my best friend. I am also thankful for the wonderful friends who helped me along the way, especially those at the Duke Catholic Center, to Robbie Kirk, and to those friends and coaches from the Duke hockey team.

I would like to acknowledge my funding sources during my time in graduate school, including the Intelligence Advanced Research Projects Activity (IARPA) and the Defense Advanced Research Projects Agency (DARPA).

Lastly, and most of all, I would like to thank my wonderful wife, Cara. This thesis would not have been possible without her love, support, patience, prayers, and encouragement.

1

Introduction

The field of quantum information science has grown tremendously in the last several decades as the allure of harnessing the mysteries of the quantum world for practical use has spurred major research projects aimed at bringing this goal to fruition. Simply put, quantum information science seeks to achieve an extremely challenging feat: to create and control arbitrarily large quantum states which cannot be modeled or represented by anything in the classical world in which we are accustomed. The demands of the current digital age for ever faster ways to process large data has led many researchers to consider future computing paradigms beyond conventional silicon based electronics. Towards this end, quantum computation has emerged as a candidate to potentially outperform even the most powerful supercomputers in performing certain computations (Stajic, 2013). One important milestone in the field of quantum computation was the invention of Shor's Algorithm, which defined one of the first practical uses for a quantum computer. In his seminal work, Peter Shor demonstrated how a quantum computer could find the prime factorization of large integers in polynomial time, a challenge that even the fastest classical computer would find insurmountable for large numbers (Shor, 1994). This algorithm provided

tremendous momentum to the field as it was one of the first algorithms demonstrating the tantalizing potential of quantum computers, and has particular significance in that it could be used to break public key encryption schemes such as RSA (Steane and Rieffel, 2000).

Another important application of quantum computers is in the field of quantum cryptography, which emerged from a pioneering study on how the potential vulnerability of encrypted data could be made perfectly secure, in theory, using the properties of quantum mechanics. Two computer scientists, Charles Bennett and Gilles Brassard, published the first quantum cryptography protocol showing a provably secure method for encrypting and transmitting private key information over a network susceptible to eavesdropping (Bennett and Brassard, 1984). This method relies on the quantum property that it is impossible to create an identical copy of an unknown and arbitrary quantum state (i.e. the No-Cloning Theorem).

Although the existence of a quantum computer capable of solving classically intractable problems, such as prime factorization or private key decryption, may still be many years away, the presence of Shor’s algorithm has served to galvanize a generation of scientists and engineers to imagine what a quantum computer would actually look like. This is still an open question today as several candidate systems are vying to show their merit as the best physical platform with which to build a quantum computer, just as potentially new groundbreaking applications of such a device are still coming to light (Ladd et al., 2010). In particular, solving problems in quantum chemistry and quantum simulation has emerged as a viable and impactful use for a small scale quantum computer (Lanyon. et al., 2010).

The fundamental building block of a quantum computer is called a “qubit.” The qubit is the quantum analog of the classical bit, whereby the binary states 0 and 1 become quantum states with distinct wavefunctions, usually denoted in the bra-ket notation as $|0\rangle$ and $|1\rangle$. The qubit differs in a fundamental way from binary logic in

that it allows for a purely quantum phenomenon of *superposition*. In a superposition state, the qubit $|\psi\rangle$ can exist simultaneously in two distinct quantum states with complex amplitudes a and b written as $|\psi\rangle = a|0\rangle + b|1\rangle$. The magnitude squared of the coefficients, $|a|^2$ and $|b|^2$, gives the probability of measuring the qubit to be in the $|0\rangle$ or $|1\rangle$ state, respectively. This probabilistic interpretation of the wavefunction amplitudes is truly fundamental to what it means to be a quantum object.

A second uniquely quantum property of qubits, which turns out to be critically useful for quantum computation and quantum communication, is that of *entanglement*. This property can best be described by considering an example of an entangled quantum state, which is the composite of two qubits, written as $|\psi\rangle = (|00\rangle + |11\rangle)/\sqrt{2}$. This state is significant in that it cannot be factored into a product of two distinct quantum states; that is, for all possible single qubit states $|\psi_1\rangle$ and $|\psi_2\rangle$, $|\psi\rangle \neq |\psi_1\rangle|\psi_2\rangle$ (Nielsen and Chuang, 2000). This particular state is one of the four Bell states which form an orthonormal basis of two qubit states, which can each be distinguished by an appropriate quantum measurement. The property of entanglement does not exist in the non-quantum mechanical description of the classical world and is considered to be a fundamental property of nature. It plays a crucial role in the field of quantum communication, which is motivated by quantum cryptography protocols to develop long range quantum networks for teleporting quantum states and transferring information securely. For computational purposes, the complexity of a massively entangled quantum state of only $\sim 50 - 100$ qubits can surpass the capacity of classical information processing, even accounting for a continuation of the Moore's Law trend of the doubling of the computational power every one to two years (Ahsan et al., 2015).

The first challenge then for quantum computer hardware designers was to find suitable qubits to use for storing and processing quantum information. Some of the leading candidates to date include lithographically patterned quantum dots in

semiconductors (Petta et al., 2005), superconducting Josephson junctions (Devoret and Schoelkopf, 2013), nitrogen vacancy (NV) centers in diamond (Awschalom et al., 2013), neutral atoms (Williams, 2004), and trapped ions (Monroe and Kim, 2013). While trapped ion qubits are the focus of the research presented here, each potential qubit has its own set of advantages and disadvantages, and it is likely that the final form of a quantum computer will use a hybrid mix of several types of qubits which maximizes their relative strengths.

1.1 Quantum Computing with Trapped Ions

Trapped atomic ion systems have been investigated for many years for their usefulness as extremely accurate atomic clocks (Rosenband et al., 2008). Some of the most often studied ions include $^9\text{Be}^+$, $^{25}\text{Mg}^+$, $^{40}\text{Ca}^+$, and $^{171}\text{Yb}^+$. For quantum computing applications, a trapped ion qubit has many highly desirable properties which make it one of the leading qubit candidates in the field. Firstly, every atomic ion of the same element and isotope is identical in every way. The usefulness of this property can be contrasted to any qubit made through a microfabrication process, such as those in quantum dots or superconductors. Although great care is taken in such systems to make each device free of defects and exactly according to specifications, in reality, each process has a finite yield rate and slight variations between each device can lead to scalability challenges when expanding the systems to larger numbers of qubits. Secondly, the trapped ion is extremely well isolated from its environment. One of the most difficult challenges for storing quantum information is that any interactions a quantum state has with its surrounding environment can rapidly destroy the quantum state through a process called decoherence. Decoherence is a loss of the coherence, or relative complex phase, between the amplitudes of a quantum state in a superposition. In other words, information stored in a quantum state is vulnerable to quantum noise, which introduces random errors into the quantum state as

it interacts with its environment. In the absence of error correction (the subject of Chapter 6), the coherence time sets the maximum time scale for which information in a quantum state can be stored reliably. Since ions are trapped in an ultra high vacuum chamber and can be shielded from stray electromagnetic fields, relatively long coherence times of several tens of seconds have been achieved (Langer et al., 2005). Lastly, despite being well isolated from the environment, trapped ions are still readily addressable for storage, manipulation, and readout of quantum information through well defined atomic transitions on time scales much shorter than the coherence time.

Local quantum operations between trapped ion qubits in a single trap are achieved using their mutual Coulomb repulsion and shared motional modes. Several basic quantum algorithms have been demonstrated with 4-6 ions, including the Deutsch-Jozsa algorithm and factoring using Shor’s algorithm (Gulde et al., 2003; Monz et al., 2016). Efforts to scale these systems to larger sizes has led to the development of surface traps with a two dimensional electrode structure made from standard micro-fabrication techniques. These traps allow for more complex electrode configurations than traditional macroscopic traps, providing the capability for trapping long chains of ions and shuttling them between different segments of the trap. Recent work has confirmed the utility of such traps for performing high fidelity logic gates (Mount et al., 2015). The primary goal of surface traps is to allow for improved scalability of ion trapping technology. Scalability here refers to the way the overhead and system complexity for operating a quantum computer grows with increasing number of qubits. Surface traps allow for a much lower marginal overhead cost for combining many individual ion traps into a quantum computer. The fabrication of a custom surface trap is the subject of Chapter 2 of this thesis.

1.2 Optical Cavities and Ion Trapping

A major advantage of trapped ion qubits for the scalability of quantum computing is the relative ease with which they can be connected via photonic interconnects. In particular, this property has important applications in the field of quantum networks. A quantum network is a broad term used to describe everything from teleportation of a quantum bit all the way to a “quantum internet” (Kimble, 2008). In such a network, quantum information is generated, stored, and purified on the nodes of the network and distributed between nodes using entangled photons (Bennett et al., 1996). Trapped atomic ions at the nodes can provide the long lived memory needed to distribute and process information over the network. By distributing entanglement over several individual quantum processing units, one can potentially overcome a limitation on the total number of trapped ion qubits in a single processing unit to scale to $10^2 - 10^3$ qubit size systems.

Long distance entanglement of quantum nodes will need some sort of quantum repeaters along the way due to the transmission loss of optical fibers. A trapped ion in an optical cavity can serve as a quantum repeater, providing a further enabling technology for large scale quantum networks. One way of implementing a quantum repeater is to transfer a quantum state from one subsystem to another via a direct coupling along the optical channel. In practice, losses in transmission or scattering mean that it is not deterministic as to whether the entanglement was successful without performing some measurement operation (Keller et al., 2004). For a lossy channel, it is therefore more desirable to generate entanglement via a heralding method rather than direct state transfer. With a heralding method, the entanglement generation between remote ions is probabilistic, but detected photons announce when entanglement is successful, and the entangled ions can be subsequently used for deterministic quantum information applications (Kok et al., 2007).

Currently, one of the main challenges that must be overcome to make such a network possible is the relatively slow ion-photon entanglement generation rate. Existing demonstrations of remote ion entanglement via photon interference achieve an ion entanglement rate of around 5 Hz, which is on a timescale comparable to that of the qubit coherence (Hucul et al., 2015). Some work has been done on integrating a high numerical aperture mirror under the ion trap, which has been shown to provide roughly a factor of two improvement in the photon collection rate when compared with only using refractive optics (Merrill et al., 2011). The goal of my research is to increase the photon collection rate by several orders of magnitude by trapping an ion inside a resonant optical cavity, thereby increasing the photon collection rate and the entanglement transfer rate of quantum states. Having a means for fast generation of photonic interconnects between remote ion qubits is a critical component for incorporating scalability into trapped ion quantum computer architectures and for improving quantum communication (Monroe et al., 2014). The optical cavity we have developed for use with trapped ion qubits is the subject of Chapters 4 and 5 of this thesis.

1.3 Quantum Computer Performance Simulation

Questions about the practical uses of quantum computers and quantum networks have led to several studies of the physical resource and performance requirements a quantum computer would have (Meter and Oskin, 2006; Monroe et al., 2014). To address these questions as they relate to trapped ion quantum computing, we created a performance simulator to study the viability of various quantum computing protocols for use with a trapped ion quantum computer. A quantum computing performance simulator is needed to provide practical metrics for the effectiveness of executing theoretical quantum information processing protocols on physical hardware. In Chapter 6 I present the design and implementation of a tool to simulate

the execution of fault tolerant quantum computation by automating the tracking of common fault paths for error propagation through an encoded circuit block and quantifying the failure probability of each encoded qubit throughout the computation. The simulation consists of two parts. Firstly, it runs a fault path counter on encoded circuit blocks to determine the probability that two or more errors remain on the encoded qubits after each block is executed. Secondly, it combines errors from all the encoded blocks and estimates performance metrics such as the logical qubit failure probability anywhere in the circuit, the overall circuit failure probability, the number of qubits used, and the time required to run the overall circuit. We use common fault tolerant protocols on a universal hardware, assumed to be a network of qubits with full connectivity. This technique efficiently estimates the upper bound of error probability and provides a useful measure of the error threshold at low error probabilities where conventional Monte Carlo methods are ineffective. I also describe a way of simplifying the fault tolerant measurement process in the Steane code to reduce the number of error correction steps necessary. I present simulation results comparing the performance of quantum adder circuits, which constitute a major part of Shor’s algorithm.

1.4 Thesis Organization and Summary of My Contributions

This thesis is organized into seven chapters. Chapters 2 and 3 describe the main body of work concerning the building and testing of a custom made surface ion trap on a mirror. In chapters 4 and 5, I detail the design, simulation, and performance of novel micromirror optical cavities for integration with the mirror trap. In Chapter 6 I describe the implementation of a quantum computing performance simulator.

The field of ion trapping is highly collaborative in nature due to the sheer size and complexity of the experiments, and many of the results shown in this work were enabled by the contributions of other members of my lab or collaborators. I

will attempt to highlight here the primary contributions I made to each individual project, as well as those of my collaborators.

Chapter 2 describes the infrastructure needed for a trapped ion quantum computing experiment as we have implemented it. Initial trap fabrication attempts were conducted by Daniel Gaultney, and I used his process as a starting point to create my own custom fabrication process for the mirror traps. All the clean room fabrication, packaging, and assembly of the traps used for this thesis was done by me. I did all the cleaning, assembly, and machining of custom parts for the ultra high vacuum chamber used in this work, with the occasional assistance of others. The in-vacuum printed circuit board design was the work of Stephen Crain. The simulations of the electromagnetic trap fields was done with the assistance of Dr. Peter Maunz who ran the CPO simulations for the mirror trap while I performed the simulations to find the voltage solutions used in the experiments. The digital to analog (DAC) system used for the ion trapping experiments was made by Daniel Gaultney. The ion imaging lens was made by Caleb Knornschild. I made the helical resonator used in these experiments.

Chapter 3 describes the trap characterization and measurements of the ion displacement using the tweaker electrodes. The experiments, data analysis, and simulation results in this chapter were all my own work, with several important technical suggestions coming from Dr. Peter Maunz.

Chapter 4 describes the theoretical and computational analysis we did for cavity QED systems using the mirror trap. While I performed all the simulations and calculations shown in this chapter, several of the methods used were taken from early work in our group on the topic by Dr. Taehyun Kim and Dr. Peter Maunz. My analysis of the qubit state detection scheme was assisted by Dr. Geert Vrijen.

Chapter 5 describes the building and testing of the cavity micromirrors. While I assisted in the initial setup and testing of the laser ablation system, the actual

laser ablation of all the mirrors used in the experiments was done by Tripp Spivey. Processing the mirrors for coating and performing all the cavity experiments, data analysis, and simulations shown here was my own work.

Chapter 6 is about the performance simulator we made to quantify the performance metrics of running quantum error correction codes on simulated trapped ion quantum hardware. The initial code for this simulator was written before I joined the lab by an undergraduate student, Jefferey Hussmann. Subsequently, the code was worked on by several students before I took it over and made significant modifications to the structure and functions of the simulation tool. Owing to the fact that this work overlapped extensively with that of another student in our lab, Muhammad Ahsan, much of final form of the code, including the complete fault path counter results, comes from a close collaboration with Ahsan.

2

Ion Trap Experimental Setup

2.1 Introduction

This chapter describes the experimental apparatus used to trap $^{174}\text{Yb}^+$ ions with the mirror trap. This includes details of the mirror trap fabrication process, trap simulations, helical resonator, optical imaging system, UHV vacuum assembly, ytterbium flux oven, and the external cavity diode lasers. Performance results for the mirror trap are described in Chapter 3.

2.2 Atomic Structure

Singly ionized ytterbium (Yb) ions are used for all experiments and calculations shown in this thesis. The electronic structure of neutral Yb is $[\text{Xe}]4f^{14}6s^2$, containing two valence electrons in the $6s$ level. For trapping, the Yb is ionized with an energy gap of 6.254 eV to the continuum using a two photon process, where the first photon excites the transition from the 1S_0 ground state to the 1P_1 excited state at 751 526.6 GHz (398.9113 nm), and the second photon which excites the electron to the continuum is from our Doppler cooling light at 811 291 GHz (369.525 nm). Doppler

cooling, state detection, and optical pumping are all performed on the $^2S_{1/2} \leftrightarrow ^2P_{1/2}$ transition at this frequency. The $^2P_{1/2}$ energy level has a 0.5% chance of decaying to a low lying $^2D_{3/2}$ level, which has a 52.7 ms lifetime (Olmschenk et al., 2007a). The electrons in this state can be pumped back into the ground state using 935 nm light at 320 572 GHz. The basic requirement for trapping $^{174}\text{Yb}^+$ ions is therefore three lasers, one to assist with the photoionization (399 nm), one for Doppler cooling (370 nm), and one for repumping (935 nm). The most suitable isotope of Yb for use as a qubit in quantum information processing (QIP), however, is the $^{171}\text{Yb}^+$ ion. The qubit states of this ion are composed of its internal electronic states, where the $|0\rangle$ state is defined as the $^2S_{1/2}|F = 0, m_F = 0\rangle$ state and the $|1\rangle$ state is defined as the $^2S_{1/2}|F = 1, m_F = 0\rangle$ state. The qubit states have a frequency splitting of 12.6 GHz. The relevant energy levels for both Yb ions are shown in Fig. 2.1.

Trapped ions can be cooled using the Doppler cooling technique by which the ions can dissipate motional energy via an absorption and subsequent spontaneous emission of a photon. The linear momentum of the light ($\vec{p} = \hbar\vec{k}$) is transferred to the ion during a photon absorption always in the direction of the photon's propagation. Spontaneous emission is a probabilistic decay process with a timescale inversely proportional to the excited state linewidth, which for $^{174}\text{Yb}^+$ is 19.7 MHz, where the photon is emitted in a random direction over a 4π solid angle. For an ion oscillating in a harmonic trap, the frequency of the laser light will be Doppler shifted proportional to the ion's velocity. When the cooling laser is red detuned to frequencies \sim 2-80 MHz below the ion's transition frequency, the ion will only absorb photons when its velocity has a component opposite to the photon's propagation direction. As a result, the net momentum of the ion is reduced by absorption of the red detuned photons, while the random nature of the spontaneous emission in all directions does not impart a net time averaged momentum to the ion. This phenomenon is exploited for cooling trapped ions down to the Doppler cooling limit of the ion's motional energy

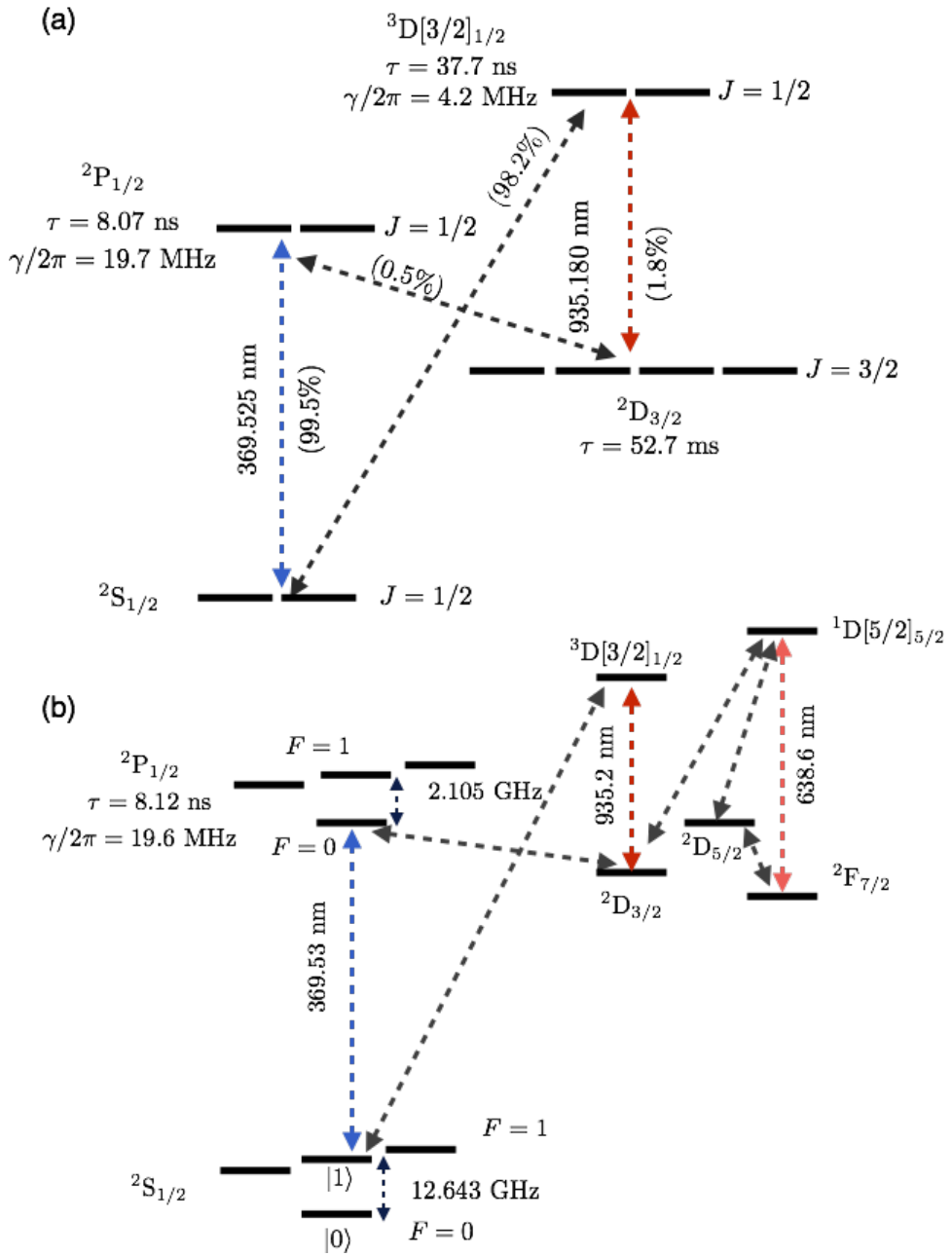


FIGURE 2.1: (a) The energy level diagram of $^{174}\text{Yb}^+$ (Burd et al., 2014). (b) The relevant energy levels of $^{171}\text{Yb}^+$ (Olmschenk et al., 2007b). Diagrams are not to scale.

in a harmonic trap, which is given by

$$E_D = k_B T_D = \frac{\hbar\gamma}{2} \quad (2.1)$$

for a spontaneous emission rate γ (Itano et al., 1995). For $^{174}\text{Yb}^+$, the Doppler energy is $E_D = 4 \times 10^{-5}$ meV corresponding to a Doppler temperature $T_D = 0.5$ mK. While the Doppler cooling temperature is limited by the spontaneous emission rate γ , several methods exist for cooling below the Doppler limit. These include sideband cooling and polarization gradient cooling (Diedrich et al., 1989; Wineland et al., 1992).

A high flux of naturally abundant Yb atoms for subsequent photoionization and trapping is created using a small atomic oven. This consists of a stainless steel tube with a diameter of 0.5 mm and a length about 20 mm which contains small flakes of solid Yb. The back of the tube is crimped closed and spot welded to a thin tantalum wire (2 mm in width) about 25 mm long. The tantalum is then attached to a wire which connects it to a current source outside the vacuum chamber. By driving around 1 A of current through the tantalum wire, the oven tube heats to around 600° C and the Yb evaporates and flows through the tube and out of the oven in a directed fashion. The ovens were tested and aligned by placing a glass slide at the location of the trap, heating up the tantalum for about 10-15 minutes, and looking for a darkened spot of Yb buildup on the glass slide to confirm that the atomic flux was pointed towards the ion trapping location.

2.3 Ion Trap Working Principles

An ionized atom can be trapped in a radio frequency (RF) Paul trap using a combination of an RF oscillating voltage and static direct current (DC) voltages. That a three dimensional trap cannot be made from static voltages alone is called Earnshaw's theorem, and hence both RF and DC fields are required for trapping ions.

The electrode geometry of the mirror trap is shown in Fig. 2.2, where the DC voltages from the segmented outer electrodes confine the ion along the axial direction (x-direction), while the RF voltage from the linear RF electrodes confines the ion in the radial directions (y-z plane). If the field from the RF electrodes oscillates fast enough compared to the ion's motion, then the ion effectively sees a time averaged electromagnetic (EM) field in the y and z directions. An electric potential from the RF field arises from the conservative ponderomotive force, which can confine the ion in the radial trap directions. This is a nonlinear force experienced by the ion in the presence of an inhomogeneous and oscillating EM field and is given by

$$\mathbf{F}_p = -\frac{e^2}{4m\omega^2} \nabla E^2 \quad (2.2)$$

for a field amplitude E oscillating at angular frequency ω , and an ion of mass m and charge e . The pseudopotential from which the ponderomotive force arises provides the harmonic trapping potential in the radial directions. The minimum of this pseudopotential is also where the RF field vanishes, which is called the RF null (or ion trap location). The DC fields which confine the ion in the axial direction will have a saddle shape with a local extrema called the DC null, at which point the DC field vanishes. The ideal trapping condition is to have the DC null overlap with the RF null such that at the trapping location there is no electric field. Any non-zero field at the pseudopotential minimum, whether due to stray fields from charging of the trap surface or to a mismatch between the DC null and RF null, will lead to excess micromotion. Micromotion is characterized by a driven motion of the ion responding to a non-zero RF electric field causing it to oscillate at the RF frequency (Berkeland et al., 1998). Excess micromotion is explored in more detail in Sec. 3.3.

The electric potential generated from the arrangement of electrodes in an ion trap

can be written generically as

$$U(x, y, z, t) = \frac{U_0}{2}(\alpha x^2 + \beta y^2 + \gamma z^2) + \frac{V_0}{2} \cos(\Omega t)(\alpha' x^2 + \beta' y^2 + \gamma' z^2), \quad (2.3)$$

where Ω is the RF angular frequency and the quadratic coefficients are restricted to solutions of $\alpha + \beta + \gamma = 0$ and $\alpha' + \beta' + \gamma' = 0$ to satisfy the Laplace equation $\nabla^2 U = 0$ at all times t . The equations of motion for a single ion of mass m and charge e in the above field, in the absence of any damping force from laser cooling, are given by the Mathieu equation

$$\ddot{u}_i + (a_i + 2q_i \cos(\Omega t)) \frac{\Omega^2}{4} u_i = 0, \quad (2.4)$$

where $\mathbf{u} = u_x \hat{x} + u_y \hat{y} + u_z \hat{z}$ is the position of the ion relative to the trap coordinate system,

$$a_x = a_y = \frac{-a_z}{2} = -\frac{4e\alpha U_0}{m\Omega^2} \quad (2.5)$$

and

$$q_x = -q_y = \frac{2e\alpha' V_0}{m\Omega^2}, q_z = 0. \quad (2.6)$$

These coupled differential equations gives rise to a first order solution of the ion's motion along the i^{th} axis in a harmonic potential as

$$u_i^{(1)}(t) = u_{1i} \cos(\omega_i t + \phi_i) \left(1 + \frac{q_i}{2} \cos(\Omega t)\right), \quad (2.7)$$

where $\omega_i = \sqrt{a_i + q_i^2/2}$ is called the secular trap frequency. For most ion traps, the potential depth from the RF field will be much larger than that from the DC fields and pseudopotential (i.e. $U_0 \ll V_0$), and we use the common approximation of $a_i \approx 0$ and $\omega_i \approx q_i/(2\sqrt{2}\Omega)$ (Leibfried et al., 2003; Berkeland et al., 1998). From Eqn. 2.7 we see that in addition to the oscillations at the trap frequency ω_i , the ion undergoes unavoidable micromotion that occurs as the ion oscillates back and forth

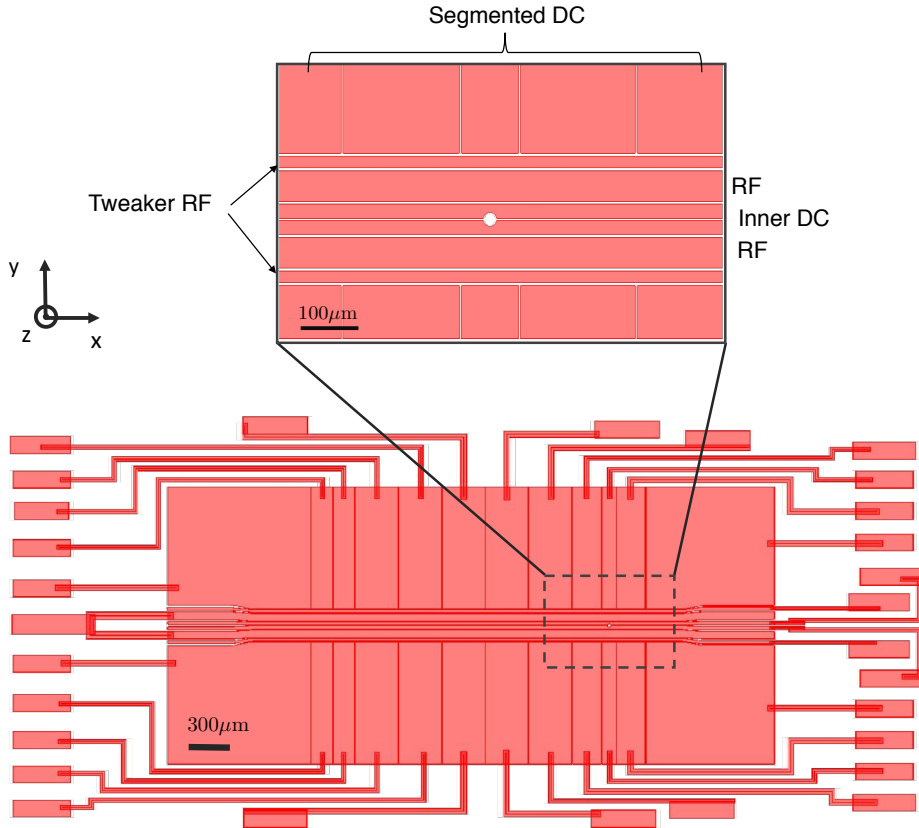


FIGURE 2.2: The photolithography mask used in the mirror trap fabrication. There are 24 segmented DC electrodes for confining the ion along the axial direction. The two inner DC electrodes which run along the length of the trap are used for rotating the trap principal axes. There are two primary trapping regions, one over the hole in the trap for the cavity experiments and one 2 mm to the left (around the 150 μm electrodes) for loading ions into the trap. This separation allows for the ability to block the Yb atomic flux used for loading ions from the exposed cavity mirror.

across the RF null. Unlike excess micromotion, this micromotion can be reduced with cooling of the ion which reduces u_{1i} .

2.4 Surface Trap Design and Fabrication

This section describes the design and fabrication of the mirror ion trap made for the purpose of integrating a surface trap with an optical cavity. Our strategy for optical cavity integration was to fabricate the surface trap directly on a mirror which can

form half of a hemispherical cavity. While the properties of this mirror are described in more detail in Sec. 5.2, for the purpose of ion trap fabrication, its most significant feature was that it was a highly reflective surface at the ultra-violet (UV) wavelengths used for photolithographic patterning of the trap features. The consequences of this are addressed in the description of the fabrication procedure in the following sections.

The mirror trap has 24 outer DC electrodes, two inner DC electrodes, two RF electrodes, and two tweaker RF electrodes as shown in Fig. 2.2. We placed a hole along the center axis of the trap to expose the underlying mirror for the optical cavity. This hole had to be large enough to reflect the optical cavity mode without introducing significant clipping losses. The tradeoff consideration, however, for larger hole sizes is that a greater surface area of dielectric is exposed to the ion which can affect the trap stability. Dielectric surfaces are insulators and can become charged, especially during exposure to UV light, and these charges can disturb the harmonic trapping potential of the ion. Charging is a significant issue faced in any ion trap experiment with dielectric surfaces such as mirrors or viewport windows close to the ions, and its effects are studied in more detail in Chapter 3. Our design goal was therefore to make the hole in the trap surface just large enough to avoid significant clipping losses of the cavity mode, but not too large so as to mitigate the effects of charging. After performing tests of the cavity losses from reflection off the mirror for various holes diameters from $100 \mu\text{m}$ down to $15 \mu\text{m}$, we determined that a diameter of around $24 \mu\text{m}$ was the smallest the cavity hole could be made before the clipping loss increased substantially. This is the diameter of the hole in the final trap design shown in Fig. 2.2. Immediately surrounding the hole are a pair of axial DC electrodes called the inner DC electrodes. Their purpose is to improve the ability to rotate the trap axis, a property which is explored in more detail in Sec. 2.4.1.

Our design calls for two primary trapping locations, with one location over the cavity hole and the other two millimeters away along the x-axis for ion loading. The

motivation behind the separate loading zone away from the cavity region is to avoid spraying Yb flux from the oven for loading ions over the exposed mirror in the cavity region of the trap. Any Yb atoms which deposit on the mirror surface inside the cavity hole will scatter the light in the cavity and may introduce significant optical losses to the system. The separate loading zone allows us to block the flux of Yb atoms emanating from the oven tube from the cavity region using an oven aperture, only allowing the flux to pass over the loading zone. The ion, once loaded, can then be shuttled over the larger middle electrodes to the cavity region in this arrangement.

The trap height and trap depth are two other important features we optimized in the design of the mirror trap. In conventional surface traps, the trap height is defined as the distance above the trap surface where the RF pseudopotential of Eqn. 2.2 has a minimum and the oscillating RF field vanishes, also called the RF null. This location is determined by the size and spacing of the RF electrodes. The height of the RF null in a surface trap can be estimated as $\sqrt{y_0 y_1}$, where y_0 and y_1 are the coordinates of the inner and outer edges of the RF electrodes along the y-axis, respectively. Our design considerations here were again driven by a tradeoff, this time involving the proximity of the ion to the cavity beam waist, which would call for a smaller trap height, and the increased effect of charging for an ion closer to the mirror surface. We settled on a trap height of around 50 μm which was determined from considerations of the cavity mode for the initial proposal of a near concentric cavity design (as outlined in Sec. 4.2) to have the optimal location for the ion to be a single Rayleigh length away from the waist. For the expected cavity mode waist of around 2.4 μm , this corresponds to about a 50 μm ion height. These constraints led us to a design with a RF trap width of 57 μm and spacing of 120 μm . The target trap depth for a RF voltage amplitude of 200 V was 180 meV. A gap of 5 μm between the RF electrodes and neighboring electrodes was used to prevent a leakage current at high RF voltages.

While conventional traps have a fixed trap height determined by the electrode geometry, the cavity experiment requires a fine control of the ion position for placement at the center of an antinode of the cavity standing wave. Satisfying this condition will maximize the coupling strength between the ion and the cavity. For a standing wave of wavelength $\lambda = 370$ nm, the periodicity of the standing wave pattern is of $\lambda/2$, while the distance between a maximum and minimum (antinode and node) is $\lambda/4 = 92.5$ nm. In order to place the trap RF null position anywhere in the standing wave, we need to be able to adjust its height by at least 92.5 nm. We accomplish this by creating a novel trap design which introduces another pair of RF electrodes, called the “tweaker” electrodes, outside of the main RF electrodes. The width of the tweaker electrodes in the mirror trap is 20 μm , and they are driven by an independent RF source. By varying the relative voltage amplitude between the tweaker RF and the main RF, we can vary the effective width of the RF rails and adjust the ion height along the z-axis in a continuous manner. As long as the main and tweaker RF voltages are oscillating at the same frequency and in phase, and the DC null position is compensated to overlap with the RF null as it is moved, there should not be any added micromotion from making the ion height an adjustable parameter. This is one of the primary advantages of our approach and is explored in more detail in Sec. 3.3.

The design space tradeoff for making the tweaker electrodes was in determining their relative width with respect to the main RF. Our target was to have the capability to move the ion over a distance of at least one standing wave fringe of the cavity, or $\lambda/2 = 185$ nm, with a voltage in the range of 0 – 15 V that can be applied with a simple operational amplifier (op amp) circuit.¹ The larger the ratio of the tweaker electrode width to that of the main RF, the higher the responsiveness will be of the ion height to the tweaker voltage. One tradeoff for increasing the tweaker electrode width is that a wider set of electrodes pushes the outer segmented DC

¹ See Sec. 3.2 for a discussion on the operation of the tweaker electrodes.

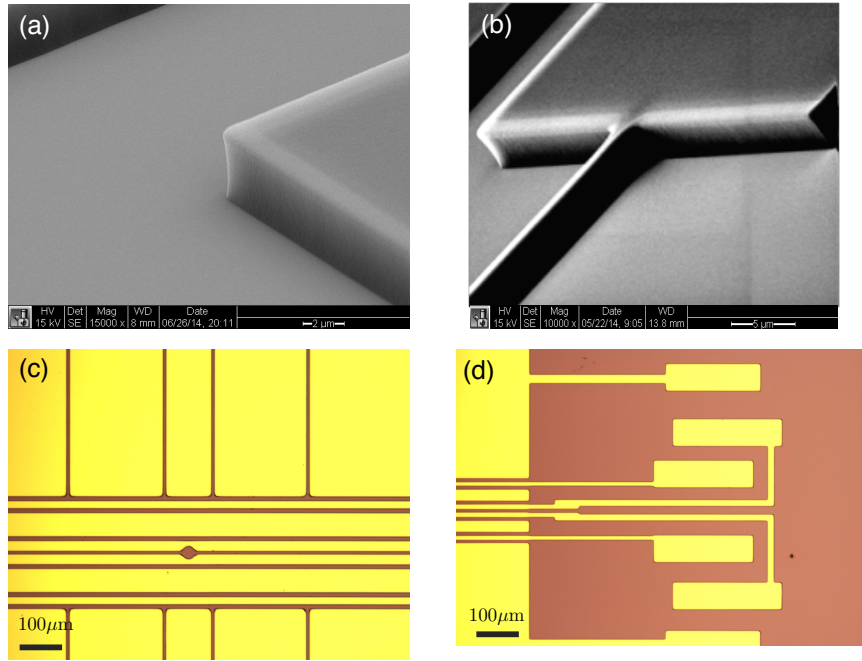


FIGURE 2.3: (a) Sidewall profile of the photoresist taken with a SEM showing the profile after a 7.2 sec exposure (scale bar is $2 \mu\text{m}$). (b) A zoomed out SEM picture showing the bond pad resist thickness near the edge of the sample (scale bar is $5 \mu\text{m}$). (c) A microscope picture of the mirror trap post metal lift off showing the trap electrodes and the hole for the optical cavity. (d) Several of the bond pads used for wire bonding the electrodes to the CPGA.

electrodes farther away from the trap location, thereby reducing their effectiveness for confining the ion in the axial direction. I tested traps with tweaker electrode widths of $10 \mu\text{m}$ and $20 \mu\text{m}$. While I was unable to test the performance of the $10 \mu\text{m}$ electrode trap due to some fabrication imperfections during processing, I found excellent performance well characterized by our design parameters using the $20 \mu\text{m}$ trap. This trap design was used for all experimental results presented in this thesis.

I made several iterations of the mirror trap at the Shared Materials and Instrumentation Facilities (SMIF) at Duke University. The SMIF facilities include a class 100 clean room with advanced microfabrication and materials characterization capabilities. A picture of the photolithography mask designed with careful considerations

for all features as outlined previously is shown in Fig. 2.2. The mask design was sent to Photo Sciences Inc. for patterning with chromium on a soda-lime glass, with a critical dimension specification of $2.0 \pm 0.25 \mu\text{m}$. The substrates used for the trap were 1/4 inch thick, 1/2 inch diameter high quality fused silica optically coated with a high reflectance (HR) coating optimized for 369.5 nm and 780 nm wavelengths and deposited by Advanced Thin Films. These mirrors were then sent off to be diced into rectangular substrates of dimensions 3.25 mm wide by 8 mm long at the Stanford University glass shop. The substrates had to be wide enough to fit the trap, but not too wide as that would lead to a clipping of the lasers used for trapping at the edge of the substrate. The trap was fabricated using a photolithographic process to make the electrode pattern, followed by an evaporation step to deposit Titanium (Ti) and Gold (Au). The presence of the HR coating on the substrate changed the standard photolithography process because the UV exposure was increased from the reflection of the UV light off the mirror surface. It also created a standing wave inside the photoresist, which further reduced the uniformity of the exposure.

For the photolithography process I used a negative photoresist, NFR-016D2, which meant that any areas of resist exposed to the UV light remained on the sample, and any parts that were not exposed were removed during the develop step. The exact procedure for fabricating the trap came from a process of trial and error to find the best way to modify the standard procedure for photolithography with NFR-016D2 to fit the unusual rectangular substrate shape and the presence of the HR coating on the surface. To help find the right exposure time, I coated several test samples in sputtered gold and imaged them using a scanning electron microscope (SEM) to see the sidewall profile of the photoresist. Having an undercut sidewall profile is critical for a clean metal lift off in a later process step. I found an exposure time of 7.2 seconds did not overly expose the photo resist but also was not too short as to prevent a good sidewall profile from forming after development. Several of the

SEM images showing the photoresist after development are shown in Fig. 2.3. For comparison, the standard NFR-016D2 process on a non-reflecting substrate calls for a 12 second exposure.

A second significant change we had to make to the standard process was the spin coating speed. The standard process calls for spinning the photoresist at 3000 rpm for 30 seconds, which leaves a resist film thickness of approximately $3.9\ \mu m$. However, with a rectangular substrate, the photoresist tends to bead up on the edges and especially the corners of the sample due to surface tension effects. Around the bond pad regions which are located closest to the corners of the trap, the photoresist will be thicker than on the rest of the sample, which can lead to residual photoresist remaining over these bond pads after the development step, for example. To counteract the effects of the photoresist edge beads, I increased the spin speed to 6000 rpm, which pushed the edge beads farther away from the center of rotation. This led to a decrease in the film thickness to $3.0\ \mu m$, which was still an acceptable thickness for the metal liftoff step. The gold thickness of the trap was limited to around 350 nm to make it less likely that it would coat the photoresist sidewalls and not liftoff cleanly. While it is possible to make traps with metal thicknesses of up to $1\ \mu m$ using this process, the lower yield rate and increased risk of metal tearing during lift off was deemed not worth the potential benefits of thicker gold. The full fabrication process for the mirror traps I made is listed here:

1. Clean the mirror sample by rinsing it in acetone and isopropyl alcohol (IPA).
If particulates remain on the surface, wipe it gently with a cotton swab while it is immersed in an IPA bath. Purge with nitrogen for 30 seconds.
2. Spin on the NFR-016D2 photoresist with the following cycle: 500 rpm for 5 seconds, 6000 rpm for 30 seconds with a ramp rate of 1000 rpm/s, then ramp down by 1000 rpm/s until the spinner has stopped. Set the photoresist by

baking the sample for 2 minutes at 90° C in an oven.

3. Align the alignment marks in the photo mask to the four corners of the trap substrate. Expose with 365 nm UV light at 14 mW/cm² for 7.2 seconds. Post exposure bake for 2 minutes and 45 seconds at 90° C, also in the oven.
4. Develop in MF-319 photoresist, gently agitating the sample for 60 seconds. Rinse thoroughly in de-ionized water and purge with nitrogen for 1 minute. Do not do a post develop bake.
5. Examine the sample under a microscope. If there are any defects in the photoresist pattern, rinse with acetone and repeat the process from step 1.
6. Plasma ash the sample at 100 W for 1 minute in O₂. This removes any residual films or moisture before metal deposition.
7. Electron beam evaporate 200 Å of Ti on the sample at 1 Å per second, followed by 3.5 kÅ of Au at 10 Å per second.
8. Soak in acetone for 3-12 hours. Sonicate as needed (no more than 1 minute) to help lift off any gold stuck to the edges. Rinse thoroughly with IPA before purging with nitrogen for 1 minute.

The next step after fabrication was to package the trap in a ceramic pin grid array (CPGA) to provide a means with which to apply voltages to the electrodes. Gold wire bonds were formed between the bond pads at the outer edge of the trap and bond pads on the CPGA. Small capacitors of approximately 0.8 mm in length and width, 0.25 mm in thickness, and 820 pF in capacitance from the vendor American Technical Ceramics were used to provide filtering of any RF pickup on the DC electrodes from the main RF voltage. These capacitors provided a low impedance path to ground for any RF pickup on the DC electrodes and were epoxied using UHV compatible

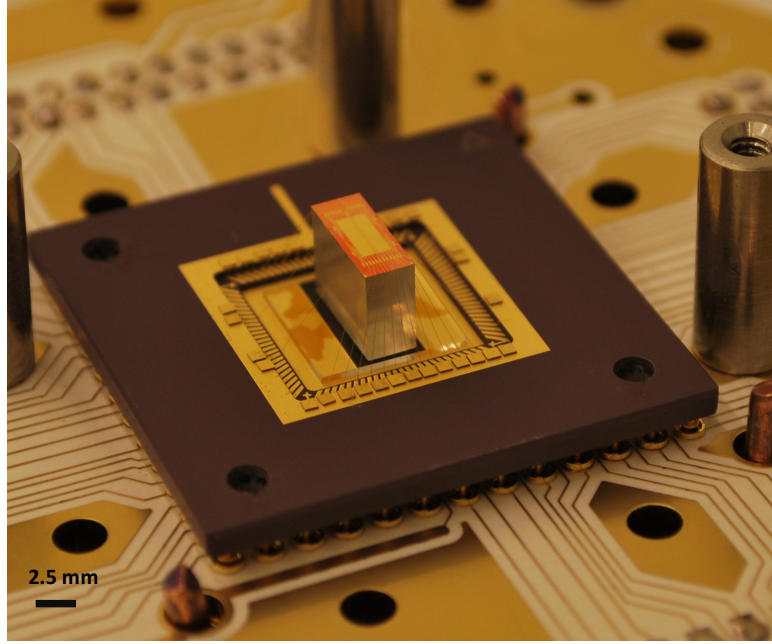


FIGURE 2.4: A picture showing the packaged mirror trap on the CPGA. The capacitors around the edge of the CPGA help filter out the unwanted RF pickup on the DC electrodes. Gold wire bonds connect the capacitors to the CPGA pads and to the electrode bond pads on the trap. Also shown here is part of the printed circuit board routing the electrical signals from the vacuum chamber feedthroughs to pins on the CPGA.

conductive epoxy (Epo-Tech H20E) to the gold outer edge of the CGPA, as shown in Fig. 2.4. The trap itself was epoxied to a 0.5 mm thick fused silica slide which was then epoxied to the CPGA using the 353 ND epoxy also from the vendor Epo-Tech.

2.4.1 Trap Simulations

We simulated the performance of the trap to find an optimal set of voltages to apply to the RF and DC electrodes to form the trapping potential. The software used for generating the electric field from the exact geometry of the electrodes is called the Charged Particle Optics (CPO) software. The simulated EM fields found from this program were read into a Mathematica notebook to solve for appropriate electrode voltages for trapping. As described in Sec. 2.3, the optimal trapping condition over-

laps the pseudopotential minimum from the RF field with the DC null. Symmetry requirements on the DC potentials for a vanishing field at the trap location dictate that the final voltages should be a linear combination of antisymmetric and symmetric voltages around the trap axis. The antisymmetric solutions serve the purpose of rotating the principal axes of the harmonic trapping potential in the y-z plane. These principal axes, also called the trap axes, define the oscillation directions of the eigenmodes of the 2D harmonic trapping potential of Eqn. 2.3. In order for Doppler cooling to be effective, the cooling beam must have a propagation component along each principal trap axis so that it can cool all eigenmodes of the ion. Fig. 2.5c shows the trap axes rotated approximately 20° from the normal with the trapping solutions used for the mirror trap. The axial trap axis (x-axis) is rotated 45° with respect to the horizontal direction of the cooling lasers to allow for cooling the axial eigenmode. Fig. 2.5d shows the EM field vectors from the RF electrodes at a moment in time as they create the quadrupole trapping field. The vanishing point of these field vectors defines the trap location, which from the simulations we find to be approximately $50\ \mu\text{m}$ above the trap surface. The ponderomotive pseudopotential of Eqn. 2.2, which defines the trapping potential in the radial directions, is shown in Fig. 2.5a. A picture of the trap installed within the vacuum chamber also showing the ground shield and the Yb oven is shown in Fig. 2.6.

2.4.2 Helical Resonator

RF trap voltages of around 150-200 V are required to achieve sufficient trap depths to trap Yb ions in surface trap geometries. The trap depth should be significantly larger than the thermal energy of the ion at room temperature, which is around $k_B T \approx 26\ \text{meV}$. We do not apply RF power directly to the trap electrodes, as this could lead to several problems. Firstly, unless the output of the amplifier is impedance matched to the trap, the signal will be reflected from the trap and the power will be dissipated

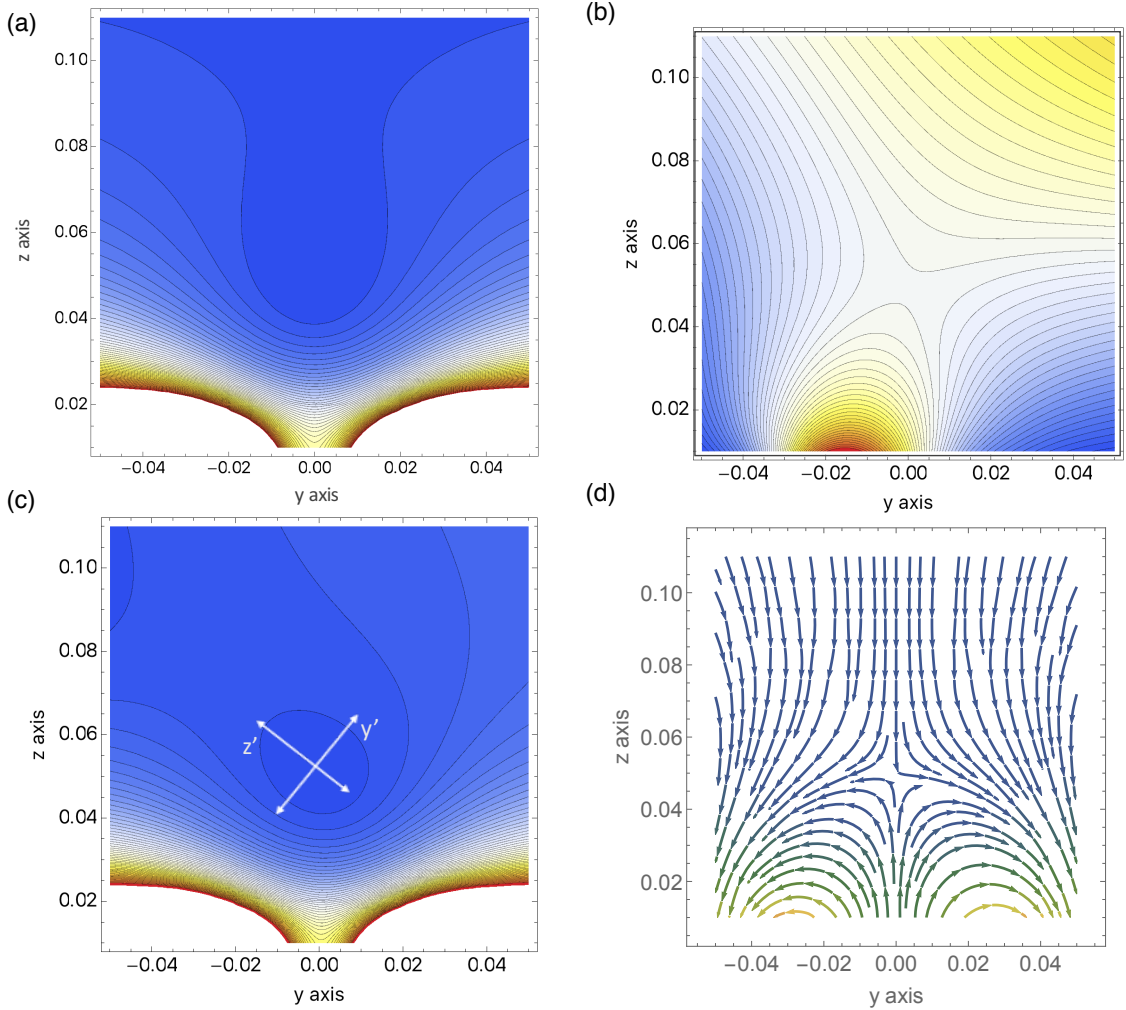


FIGURE 2.5: (a) A contour plot showing the electric potential formed by the RF electrodes (axis units in mm). (b) The electric potential from the applied DC fields. This data was generated by simulating the EM field generated from each electrode with 1V applied, and then superimposing all of those fields together with appropriate scaling factors for each electrode's voltage. (c) The combined RF and DC potentials showing a rotation of the trap axes. (d) A snapshot of the simulated electric field at a moment in time shows the formation of a quadrupole trap along the y and z axes. The RF null is the point where the field vanishes, which here is roughly 50 μm above the trap surface.

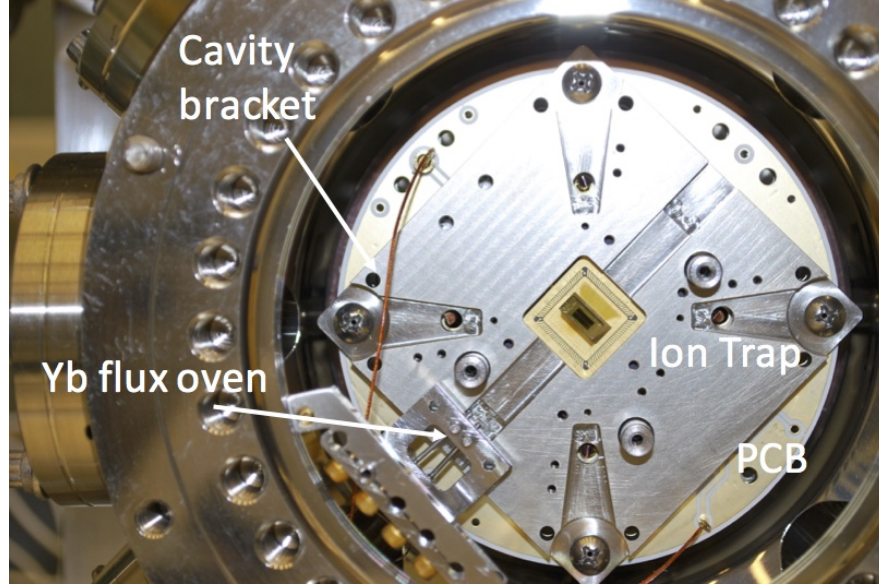


FIGURE 2.6: A picture taken in the clean room when the vacuum chamber was opened for installing a new trap. Pictured here is the vacuum compatible printed circuit board for delivering the RF and DC voltages to the trap, the titanium cavity bracket for mounting the trap, the non-evaporable getter attached to the RF ground shield for absorbing gas molecules in the chamber, and the atomic flux oven in the bottom left corner for loading Yb atoms into the trap.

on the output impedance of the amplifier. This will require a power rating on the amplifier much larger than what is required to drive the trap voltage. Secondly, it will inject noise into the RF signal which can heat the ion. To circumvent this problem, I have made a helical resonator for voltage amplification of the RF signal to be used with the mirror trap. The amplification from the resonator depends on its quality factor, which is a function of its inductance L , capacitance C , and resistance R as

$$Q = \frac{1}{R} \sqrt{\frac{L}{C}}. \quad (2.8)$$

The peak voltage of the resonant circuit with input power P is given by

$$V_{RF} \approx \kappa \sqrt{2PQ}, \quad (2.9)$$

where κ is the geometrical factor of the resonator given by

$$\kappa = \left(\frac{L}{C} \right)^{1/4}. \quad (2.10)$$

The resonant frequency of an LC circuit is given by $\omega_0 = 1/\sqrt{LC}$. Applying RF power with a high Q resonator in this way reduces the power in the unwanted frequencies being applied and amplifies, which can cause unwanted heating of the ion. In order to minimize the capacitance and maximize the inductance, I made the helical resonator coil out of copper tubing and copper wire. This allows for a relatively high inductance from the solenoid coil combined with a low capacitive coupling between the coil and the outer copper tubing (Sivers et al., 2012). Connecting an amplifier directly to the resonator would increase the resistance of the resonant circuit by the output impedance of the amplifier (usually 50Ω), and therefore dissipate power and lower the Q factor. To avoid this problem, we connect the resonator can to the RF amplifier through inductive coupling by driving a circular coil placed inside the main inductance solenoid. This decouples the amplifier's output resistance from the resonant circuit, and allows for a way to impedance match the amplifier output to the resonator by adjusting the inductive coupling between the inner coil of the transformer and the main resonator coil. This is usually accomplished by adjusting the overlap of the two coils until the power transferred to the resonator from the amplifier is maximized.

The frequency and amplitude of the RF voltage, along with the trap geometry, determine the shape of the harmonic trapping potential and hence the trap frequencies. These are all relevant quantities for calculating the trap stability parameter from Eqn. 2.6, which is proportional to the ratio of the trap frequency to the RF frequency as $q_i = 2\sqrt{2}\omega_i/\Omega$. The deeper the trap potential from the RF pseudopotential, the higher the trap frequencies will be. However, there exist trap instability

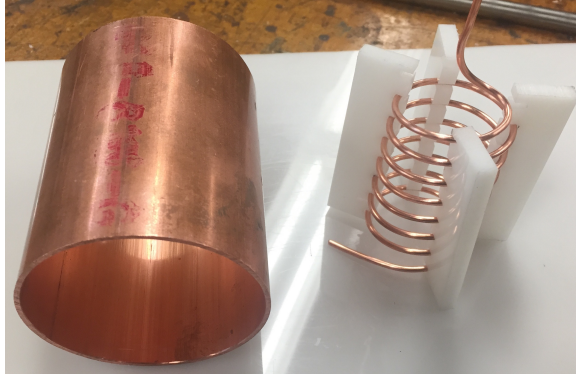


FIGURE 2.7: A picture of the outer copper shield and inner copper coil held in place with machined teflon pieces for assembling the helical resonator to drive the main trap RF voltage.

points for certain values of q , and these points become more densely packed as the trap frequency is increased and q approaches 1. For this reason, my aim was to make a resonator with as high a resonant frequency as possible to minimize q . The primary load on the resonator is from the trap capacitance, which is around 12 pF for the mirror trap, which provides one limit on how high we can make the resonant frequency. For the helical resonator I made, the quality factor is $Q \approx 80$ and the resonance frequency when attached to the capacitive load of the trap is 42.5 MHz. The resonator itself was formed from copper tubing 2.5 inches in diameter and 3.3 inches in length, and a helical coil of pitch 0.135 turns/inch made from 14 wire gauge copper. A picture of the outer copper shield and the inner copper coil of the helical resonator is shown in Fig. 2.7.

2.5 Ion Trap Infrastructure

2.5.1 Lasers

The primary means with which we interact with trapped ions, whether by exciting transitions of their internal electronic states or their motional states, involves laser light. These lasers must be well controlled in frequency, power output, and mode

shape in order to be effectively used for trapped ion experiments. A common technique for making highly stable lasers involves placing the optical gain medium of the laser diode inside an external cavity to provide optical feedback. By tuning the cavity resonance, one can control the frequency of light which is fed back into the cavity and thereby select the dominant optical mode for the stimulated emission. Lasers enclosed in an optical cavity are called external cavity diode lasers (ECDL) (Littman and Metcalf, 1978). I used three such lasers for the experiments shown in this thesis for cooling, photoionization, and repumping of trapped $^{174}\text{Yb}^+$ ions. These lasers were constructed in the Littrow configuration, whereby a diffraction grating is used to provide optical feedback by reflecting a specific frequency range of the laser output corresponding to the first order diffraction maximum of the grating back into the laser diode. The majority of the optical power is transmitted in the zeroth order reflection and used for the experiments, while a much smaller fraction is reflected back from the first order Bragg scattering. The frequency of the feedback light is set by the angle of the diffraction grating, which can be used to select a relatively broad frequency range of 100s of GHz. Within this range, the laser frequency is narrowed further by the resonance condition of the external cavity, which is determined by the cavity length and linewidth. The linewidth of the optical cavity sets the laser output frequency to a range of about 2-5 GHz. Within this window, the frequency can be selected within a range of a few MHz using a piezo to shift the cavity length.

The laser temperature is an important parameter for shifting the gain of the laser diode to be as large as possible at the desired operating wavelength. For the laser diode used in the 370 nm wavelength laser, the operation temperature was around 10° C. Cooling of the laser was accomplished using a thermoelectric cooler (TEC) attached to the laser diode mount, and a water cooling chiller to cool the base of the laser box down to 14° C. The entire box housing the laser was purged with nitrogen to lower the humidity and prevent water condensation on the diode.

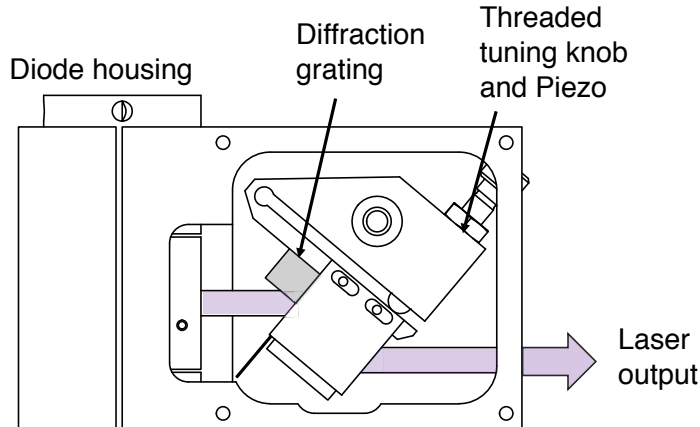


FIGURE 2.8: A drawing of the external cavity diode laser using the Littrow configuration that I assembled for the 370 nm wavelength laser. The diffraction grating and the laser diode form an optical cavity for selecting a frequency for lasing, and the feedback signal for stabilizing the output frequency is applied to the piezo on the flexure arm as shown. This laser was used primarily for Doppler cooling the trapped ions.

Once the laser is set to the desired frequency, it must be locked to a stable reference to prevent it from drifting over time. A suitable feedback signal can be applied to the piezo of the laser grating to keep the laser locked to the reference point. For the 370 nm laser used in these experiments, the reference laser was another 370 nm laser which had its frequency locked to an absolute reference from the energy levels of Yb ions. The saturation spectroscopy used to provide this stable reference utilized an ionized gas of Yb ions called a hollow cathode lamp (HCL). A diagram of the optical setup for the HCL is shown in Fig. 2.9. We use polarization spectroscopy to generate a Doppler free spectroscopic signal of ionized Yb, which allows us to generate a good frequency discriminant signal for laser stabilization. A complete description of this technique can be found in (Lee et al., 2014). The locked master laser then becomes a stable reference with which to lock all other lasers in the lab using a beat note lock. The HCL laser lock kept the master laser to within about 1-2 MHz of the set point frequency using a custom made feedback controller.

The laser used for experiments shown in this thesis was locked using this beat note technique whereby the master laser and reference laser are overlapped on a high speed photo diode (Hamamatsu PD S9055) to create a beat note signal. The beat note produced is then sent to a prescalar (RF Bay Inc. FPS-10-12) to reduce the frequency by a factor of 10 and then a 3-300 MHZ phase detector with a loop filter (RF Bay Inc., PDF-100) where it is compared to the output signal from a direct digital synthesis (DDS) board. The phase difference between the beat note and the DDS output creates a suitable error signal for locking other lasers to the master laser. This beat note technique allows us to lock any number of lasers to a single master laser as long as there is enough optical power from the master laser and their frequency difference is not more than about 2.5 GHz, which is the approximate bandwidth of the beat note detection electronics used. The stability of the 370 nm cooling laser achieved using this technique was measured to be around 1-3 MHz, which was primarily limited by fast fluctuations in the laser output frequency.

The photoionization laser used in this experiment was the same type of ECDL laser as the 370 nm laser, but was not locked to stable reference since it was only used for a brief time (1-5 minutes) when an ion was being loaded into the trap, and its frequency did not drift substantially over this time. The exact photoionization frequency for ionizing ^{174}Yb depends on any Doppler shift the moving atomic flux beam emanating from the oven may have relative to the 399 nm laser beam. As shown in Fig. 2.6, the Yb oven is in the bottom left corner of the chamber at an angle of around 20° from horizontal, while the 399 nm laser light propagates from left to right in this picture. This means that the Doppler shift from the atom's velocity will shift the laser frequency needed to excite the 1S_0 to 1P_1 transition used as part of the photoionization process towards higher frequencies. As a result, I performed spectroscopy on the excitation signal of the 399 nm light to find where the photoionization transition frequency of ^{174}Yb was when accounting for the Doppler

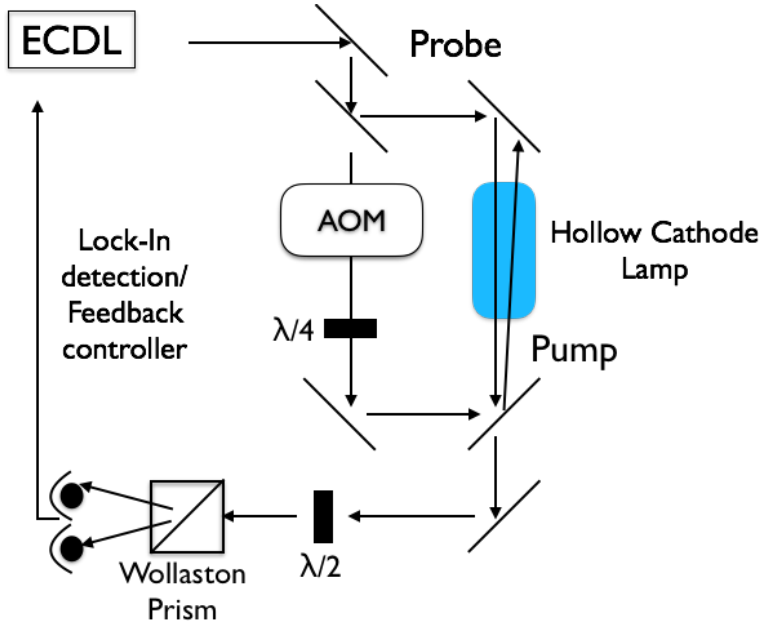


FIGURE 2.9: A diagram of the hollow cathode lamp setup. The pump beam is modulated using an AOM at 210 MHz, and the error signal is read out through a lock in amplifier.

shift of the transition frequency as compared with those values cited in the literature (Das et al., 2005). Comparison of the spectroscopy peaks shown in Fig. 2.10 with the known values allowed us to determine the Doppler shift of the Yb flux to be around 900 MHz.

2.5.2 Vacuum Assembly

A significant effort when constructing and maintaining an ion trap experiment goes towards creating an ultra-high vacuum (UHV) environment to trap the ions. Any collisions of the ion with gas molecules inside the chamber can disturb the experiment and can even kick the ion out of the trap. For this reason, pressures at least as low as 5×10^{-11} torr are needed for sensitive ion trapping experiments (1 atm = 760 torr). Reaching such low pressures requires delicate care when assembling all components inside the vacuum to make sure they are not contaminated with any oil or residue which can outgas inside the vacuum chamber and increase the pressure. Each

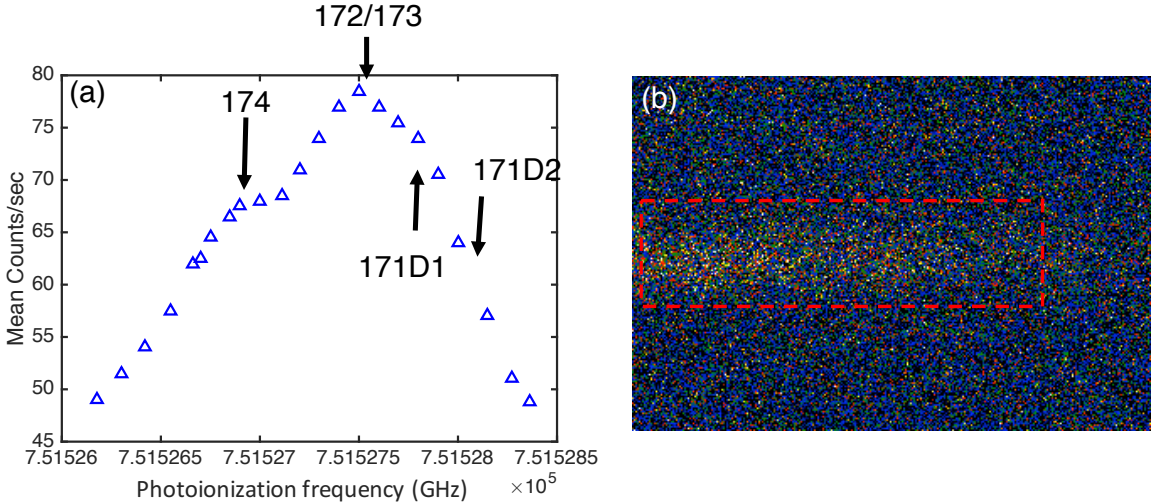


FIGURE 2.10: Imaging data of the fluorescence signal from Yb atoms emanating from the atomic oven when excited with 399 nm wavelength. We can determine the correct Doppler shifted frequency to ionize the ^{174}Yb isotope for trapping by correlating the different peaks in the spectrum to different isotopes. (a) The mean number of counts measured on the Andor camera in the reference window shown in (b) as a function of the laser frequency.

component placed inside the chamber is cleaned with a thorough solvent cleaning process to remove any residue or debris. As part of this process, the parts are first rinsed with IPA and then sonicated in Acetone for at least twenty minutes. Secondly, any stainless steel parts, including the entire chamber housing, are baked overnight at 200° C to outgas any moisture or water molecules which may be trapped inside the metal. Following this, all components are sonicated in a strong solvent, Trichloroethylene (TCE), for one minute. All components are then rinsed with IPA again and stored only in containers already cleaned with this solvent cleaning process or else in UHV clean aluminum foil.

Assembly of the vacuum chamber and the parts inside was done inside the SMIF clean room to reduce the exposure to potential contaminants. Once cleaned, all parts are handled with clean gloves straight from the packaging. Gloves were discarded once they were used to touch something not UHV clean, such as the outside of the

chamber, other tools, or even a pen. This extreme care is necessary when handling UHV parts because if some contaminants get into the vacuum chamber and outgas at a rate that prevents the pressure from reaching a suitably low enough value, it is nearly impossible to locate where the contaminant is and, as a result, the entire vacuum assembly usually must be cleaned again. Fortunately, with the proper care, this cleaning procedure has been demonstrated to be very effective for building UHV chambers capable of pressures $< 1 \times 10^{-12}$ torr.

Once all the components are cleaned and the trap is epoxied and wire bonded to the CPGA, the CPGA is then connected to a UHV compatible printed circuit board (PCB) via press fit sockets. The purpose of the PCB board is to route the voltage signals required for trapping from the vacuum feedthroughs to the CPGA and to properly ground the trap. The PCB is made out of Rogers 6002 material, which is a UHV compatible laminate material that is also good for handling large RF voltages, such as those used in the ion trap. In addition to the RF signal, the board has four 25-pin D-sub connections for routing the DC voltages from the back flange D-sub feedthroughs to the CPGA. The connections to the PCB are made with sockets which fit tightly around the D-sub and CPGA pins for effective electrical connections without solder. The sockets are made of gold plated tin and are soldered to gold plated via holes in the PCB board, and the electrical connections are routed with gold traces on the board.

Achieving UHV pressures requires an extensive baking and pumping process to pump out gas molecules which are in the chamber or adsorbed to any of the metal surfaces. A turbomolecular pump is used for the primary initial pumping of the vacuum chamber, and is backed by an Agilent leak detector which is used as a roughing pump and to check for any leaks in the vacuum chamber. Leak checking is performed by applying helium gas around the chamber flanges and looking for a spike in the detected helium level of the leak checking pump. The temperature

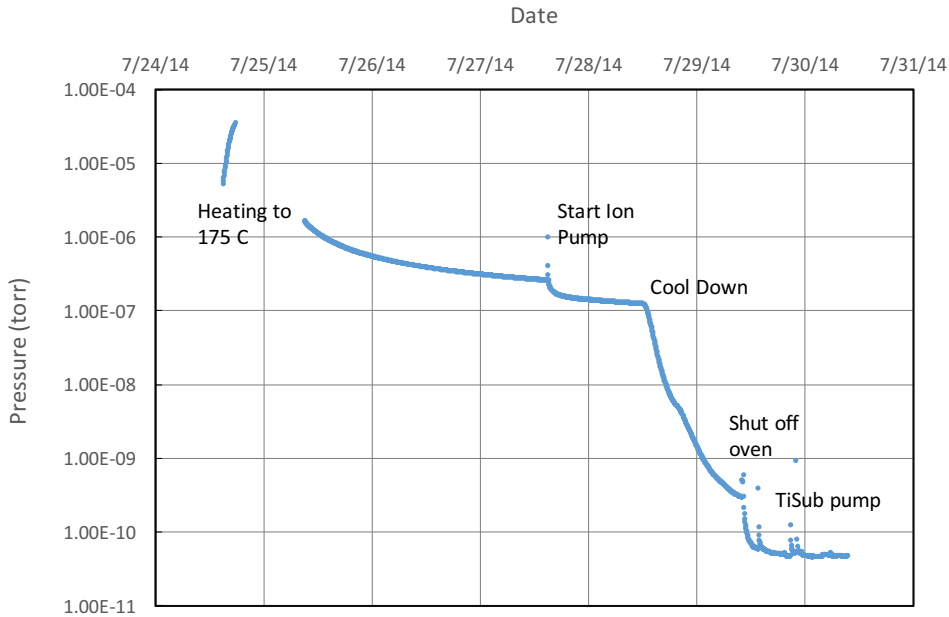


FIGURE 2.11: The process of pumping the ion trap chamber down to UHV pressures of $\sim 1 \times 10^{-11}$ torr requires many stages of heating, cooling and pumping. The pressure goes off the scale as the chamber is initially heated to 175° C. When the pressure stabilizes again after turning on the ion pump, the chamber is cooled down to room temperature. Running the TiSub pump several times helps bring the pressure down to its final level of 1.5×10^{-11} torr.

during baking was increased by no more than 1° C per minute to accommodate the different thermal expansion rates of the stainless steel and the fused silica viewports. The temperature was held at 175° C for two days while being pumped with the turbo pump and roughing pump. After the pressure stabilized, I degassed all filaments and turned on the ion pump. After the pressure went down and stabilized again, I began cooling the chamber and closed the all metal valve when the chamber reached a temperature of around 80° C. This disconnected the turbo pump from the chamber, leaving only the ion pump and the non-evaporable getter (NEG) for pumping. Once at room temperature, I fired the titanium sublimation (TiSub) pump which sputtered titanium, an effective gas adsorbent, around parts of the chamber away from the ion trap. The TiSub helped bring the pressure down to a level of $\sim 1.5 \times 10^{-11}$, which was the final pressure of the chamber used in the ion trapping experiments. A

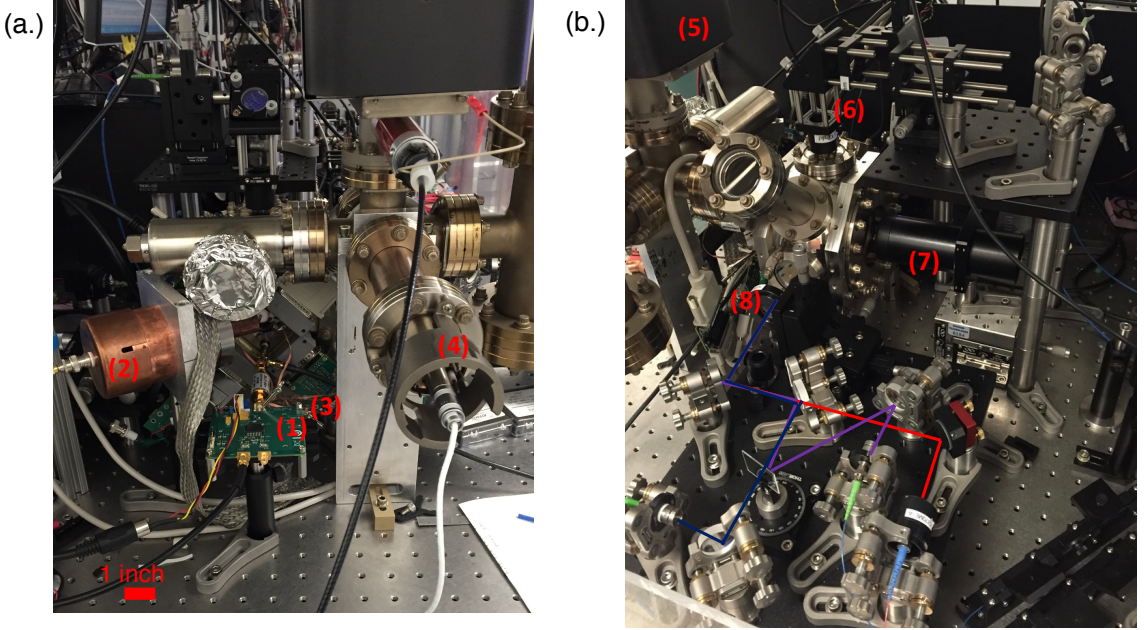


FIGURE 2.12: Pictures of the ion trapping experimental setup. Labelled components are as follows: (1) the op amp board for applying the tweaker voltage, (2) the helical resonator, (3) the D-sub feed throughs for applying the DC voltages to the trap, (4) the ion gauge filament for measuring the chamber pressure, (5) the Ion pump, (6) the side light collection for the standing wave experiment, (7) the ion imaging lens, and (8) the beam paths for the overlapping 370 nm, 399 nm, and 935 nm lasers.

pressure log of this entire process over the course of the roughly six days it took is shown in Fig. 2.11. A picture of the chamber when set up in the lab for ion trapping experiments is shown in Fig. 2.12.

2.5.3 Optical Imaging Designs

I used a compound imaging system with five lenses for imaging trapped ions onto a charge coupled device (CCD) camera and photo multiplier tube (PMT). I used 2 inch diameter off the shelf lenses with an UV anti-reflection (AR) coating. The camera used was an Andor iXon EMCCD camera, which is a high performance electron multiplying CCD camera with 16 μm pixels, which was cooled to -40° C. Some of the key performance metrics of the imaging lens found from a simulation using the

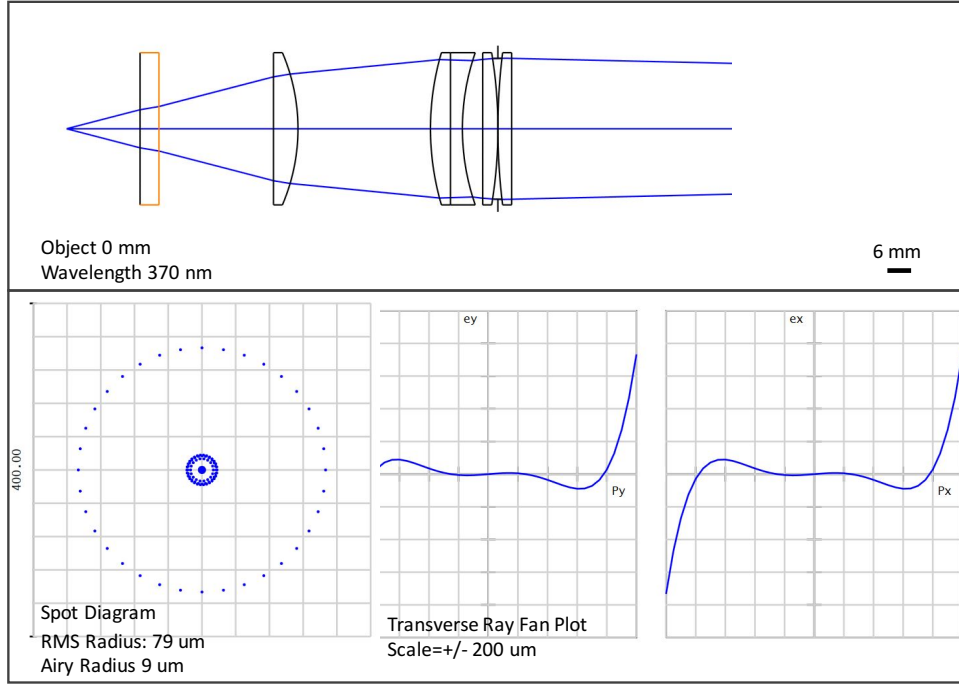


FIGURE 2.13: Simulations using Zemax software of the imaging system used for imaging the ion onto a camera or PMT. The lens design metrics shown here are the image spot diagram and the transverse ray fan plot, both at 370 nm wavelength. The spot diagram shows the point spread function for imaging a single trapped ion, and has an RMS radius about eight times larger than the diffraction limited spot size in this case. The ray fan plot shows the distance orthogonal to the optical axis between an ideal paraxial ray and the actual ray location for this imaging system. These simulations show there is some spherical aberration and coma in this lens design. Quantitative data for the ion trap experiment is taken primarily from light collected into the PMT, so as long as the final spot size directs the light from the ion into the PMT aperture, the effects of aberrations will be minimal.

Zemax software are shown in Fig. 2.13. The Zemax model includes the five lenses and the 6 mm thick front fused silica viewport on the chamber. This is a reentrant viewport with a depth of 10 mm and a distance from the trapping location of 28 mm. The effective focal length of the optical system is 90 mm, the magnification is 8.33, and the numerical aperture (NA) is 0.25.

3

Laser Cooling of Trapped Ions in a Standing Wave

3.1 Experiment Background

We conducted extensive testing of the mirror trap to quantify its capabilities and performance with regards to its eventual use in conjunction with an optical cavity. The cavity experiment for which this trap was designed imposes some rather stringent requirements on the trap itself. Some of the important requirements include having a high degree of trap stability, a long ion lifetime, sufficient trap depth, the ability to compensate for excess micromotion, and an effective means for moving the ion trap location along all three trap axes. The trap stability and trap depth were addressed in Sec. 2.4.1 as it relates to the strength of the electromagnetic potentials. Compensation of excess micromotion has been the topic of several studies which detail methods for characterizing both the trap depth and micromotion (Keller et al., 2015; Berkeland et al., 1998). These include the resolved sideband method, the photon correlation method, and the parametric excitation method. Both the photon correlation method and the parametric excitation method were used in our experiment to measure the ion micromotion in the mirror trap. A detailed analysis

of the full set of micromotion measurements is described in Sec. 3.3.

The primary goal of our experiments with the mirror trap was to measure the effectiveness of the RF tweaker electrodes for adjusting the trap location along the z-axis, perpendicular to the trap surface. For this purpose, we needed a way to precisely locate the ion’s position relative to the trap surface. Imaging the ion with a camera gives provides resolution of the ion’s position in the x-y plane to within the point spread function of the imaging system. For our imaging system, this gives us a lateral resolution of about $2 \mu\text{m}$. While this works well for locating the ion in the x-y plane, the resolution in the depth of focus is tens of microns, and therefore not fine enough to precisely locate the ion’s position along the z-axis. Even for a custom built, high NA lens ($\text{NA}=0.6$) specially designed for imaging ions, the depth of focus is still over 800 nm, and therefore an order of magnitude larger than the length scales within which we need to control the ion’s position (i.e. $\sim \lambda/10$, where $\lambda = 370 \text{ nm}$). Some work has been done on tomographic imaging of the ion position to get the three dimensional spatial resolution down to 35 nm, but this requires extensive image processing overhead and does not provide the resolution level we are targeting (Gloer et al., 2015). Our approach to locating the ion position along the z-axis involves taking advantage of the mirror surface under the trap by introducing a standing wave from the retroreflection of 370 nm wavelength light off the mirror surface. A standing wave is produced from the interference of the overlapping incident and reflected waves traveling in opposite directions. This setup provides a spatially varying light intensity with which to measure the ion position by effectively simulating the intensity distribution the ion will experience in a cavity. This approach has allowed us to explore and characterize the dynamics and position of the ion with high precision and demonstrate the effectiveness and utility of our tweaker electrode approach for adjusting the trapping location.

3.2 System Design

The application of high voltage RF signals for creating a harmonic confinement potential around the ions was discussed in Sec. 2.4.1 as an introduction to the working principles of a Paul trap. There I showed how the ion trap location, defined as the location of the vanishing RF field (RF null), is determined by the size and spacing of the linear RF electrodes. I also introduce one of the novel features of the mirror trap, which is the addition of a second set of linear RF electrodes (which we call the tweaker electrodes) for adjusting the ion trapping height in the direction perpendicular to the plane of the trap (z-axis). By adjusting the ratio of the main trap RF voltage to that on the tweaker electrodes, we can change the effective width of the RF trap electrodes, thereby adjusting the trap height over a continuous range of values.

To maximize the responsiveness of the ion height to the applied tweaker voltage and avoid introducing additional excess micromotion, the voltage on the tweaker electrodes must be applied in phase with that of the main trap RF. As detailed in Sec. 2.4.2, the main RF trap voltage is applied with a resonant LC circuit made from a helical copper wire and copper tubing. The voltage amplification of the resonator is proportional to the square root of its quality factor, $V_{RF} \propto \sqrt{Q}$. Due to their close proximity in the trap, there is some capacitive coupling on the order of 1 pF between the tweaker electrodes and main RF electrodes. This means that we cannot make a separate LC resonator circuit to drive the tweaker electrodes at the same frequency as the main RF, since this would lead to a splitting of the single resonance line into two peaks as both resonators are brought to the same resonant frequency. Another possible approach for applying a voltage on the tweaker electrodes would be to connect the two sets of electrodes with an adjustable shunt capacitor (Kim et al., 2011b; VanDevender et al., 2010). However, this approach of adding a capacitive coupling between the two sets of RF electrodes will lower the Q value of the main

RF resonator, and therefore reduce the voltage gain and potentially make the ion trap less stable. Furthermore, this method does not allow for controlling the relative phase between the two RF signals, as the phase is set by the capacitive coupling and resistance between the two electrodes. With the direct digital synthesizer (DDS) we use to generate the RF voltages, we can produce a sine wave for the trapping voltage and set an arbitrary phase for this signal with $2\pi/2^{16}$ radians of precision. This in principle can allow for precise phase matching between the main and tweaker RF signals. In practice, the degree to which these signals can be phase matched depends on the sensitivity of the measurement of their relative phase. For practical considerations such as these, we decided to use a fast operational amplifier to generate voltages on the order of 10-15 V at the 42.5 MHz frequency used for trapping. In particular, we use a high slew rate, wide output voltage range op amp from Analog Devices (ADA4870). This op amp is ideal for driving highly capacitive, low resistance loads such as the trap. Some of the important specifications of the ADA4870 include a large bandwidth of up to 52 MHz, a supply voltage range from 10-40 V, and a high slew rate of 2500 V/ μ s. For comparison, to generate a ± 10 V signal at 42 MHz requires a slew rate of at least 850 V/ μ s, which is well within the quoted specifications of this op amp. It can drive up to 1 A of current at the output and can be purchased on an evaluation board with a large exposed copper plane for applying heat sinking as needed. A picture of the evaluation board for this op amp is shown in Fig. 3.1a.

To provide a means to measure the RF phase and voltage on the tweaker electrodes, I placed a capacitive voltage divider at the output of the op amp to pickoff and sample the applied voltage, as shown in Fig. 3.1b. In this case, the pickoff voltage amplitude is proportional to the applied voltage as $V_{pickoff} = V_t(C_2/(C_1 + C_2))$, and was measured with a high impedance oscilloscope. The capacitance values used in the experiment were $C_2 = 5$ pF and $C_1 = 200$ pF, which provided a voltage pickoff reduction factor of around 40 (-32 dB). The non-inverting op amp gain was set to the

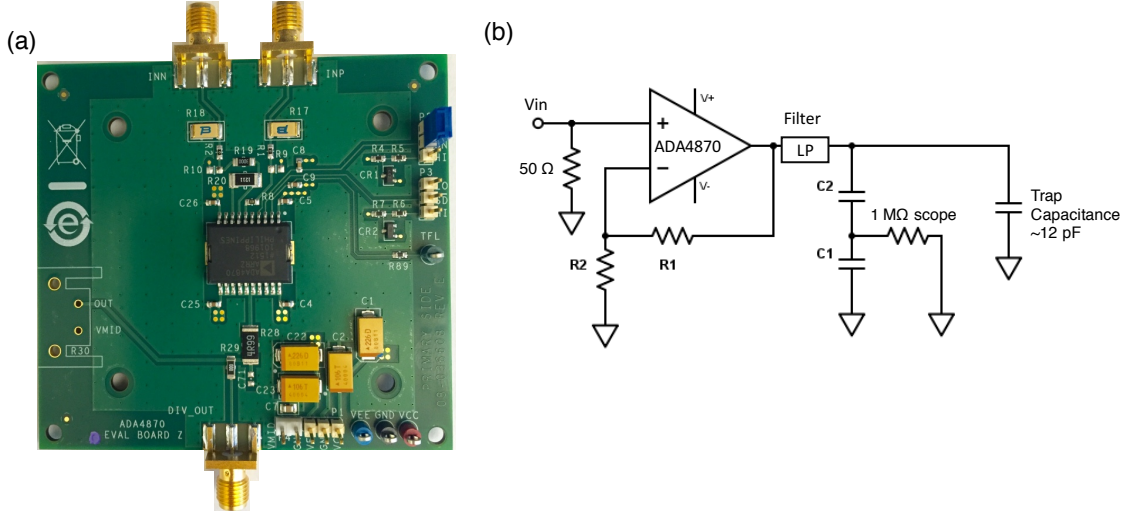


FIGURE 3.1: (a) The ADA4870 evaluation board used to drive the tweaker electrode voltage. (b) A simplified circuit of the evaluation board showing the capacitive pickoff divider and the trap capacitance.

maximum recommended value of +10 using a combination of resistors $R_1 = 1.2 \text{ k}\Omega$ and $R_2 = 133 \Omega$. I used a low pass filter at the output of the op amp to filter out the higher order harmonics of the input signal generated by distortions from the op amp, which made the output voltage signal into more of a triangle wave than a pure sine wave. This was a 50Ω low pass filter from Mini Circuits with a cutoff frequency of 48 MHz.

Measuring the voltage on the tweaker electrodes proved to be trickier than expected primarily due to the extra inductance and capacitance added by a combination of the low pass filter and the electrical connections running from the vacuum chamber feedthrough to the trap. This introduced electrical resonances into the circuit which caused the voltage to spike at certain frequencies, as shown in Fig. 3.2b. While this was not necessarily a negative effect since an enhancement in the voltage on a resonance increases the maximum accessible voltage, it made the voltage measured with the capacitive pickoff divider not a particularly good estimate of the voltage on

the trap. Based on comparisons with other measurement techniques, we concluded that the reading through the capacitive pickoff underestimates the voltage measured directly on the trap electrodes by about a factor of four to five. This is not surprising since the commercial low pass filter was designed for an output impedance of 50Ω , while the trap and pickoff load have a higher impedance of around 350Ω . This impedance causes some of the power delivered from the op amp to be reflected at the filter output. Additionally, the coaxial cable to the oscilloscope will also add some stray capacitance and change the pickoff ratio of the voltage divider. For these reasons, it is reasonable that the pickoff ratio changed from the expected value of 40:1 to something closer to 200:1. A direct voltage measurement itself without the capacitive pickoff is also not completely reliable, since the probes used to measure the voltage have their own capacitance which can alter the measurement. While the voltage measurements shown in Fig. 3.2a-b allowed us to get a good estimate of the voltage amplitude, ultimately we combined the direct voltage measurement with trap simulations to get an accurate voltage calibration for the tweaker electrodes. A measure of the voltage slopes for the various levels input power attenuations is shown in Fig. 3.2a. For the -1 dB attenuation case, the op amp output voltage saturated at a DDS amplitude of around 600 at the input, which corresponds to an input power of roughly 14 dBm after the pre-amplifier.

For calibration, we compare these voltage measurements with our expectations from the trap simulations about how the ion trap height should scale with the tweaker voltage amplitude. This scaling is dependent on the ratio of the width of the main RF electrodes to that of the tweaker RF electrodes, the main RF voltage, and the relative phase between the two signals. For the $20 \mu\text{m}$ wide tweaker electrodes on the mirror trap, the ratio to the RF electrode width was 0.35. The main RF voltage used had a 190 V amplitude. With these parameters, the simulated change in ion height was directly proportional to the tweaker voltage applied in-phase with a slope

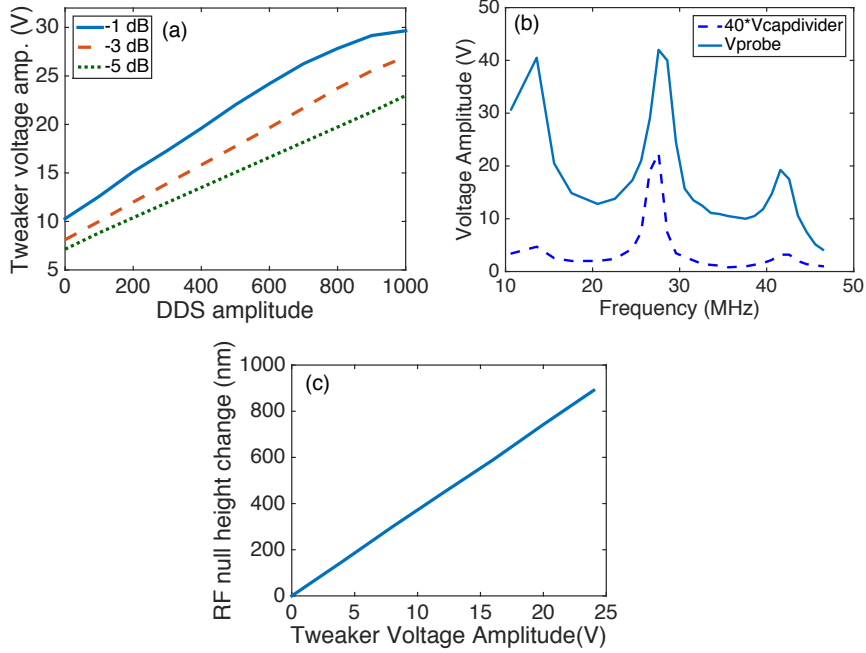


FIGURE 3.2: (a) Measuring the voltage applied to the tweaker electrodes is done with a capacitive pickoff voltage divider for various levels of input attenuation. (b) Measurements using a pickoff wire will give a more direct probe of the voltage, but will introduce stray capacitance and inductance to the system resulting in the measurement probe altering the voltage itself. The voltage measured with the capacitive divider is multiplied by a factor of 40 here to account for the voltage divider having a roughly 40:1 pickoff ratio. (c) Simulation results showing that the minimum of the ponderomotive potential (also the RF null position) along the z-axis scales linearly with the tweaker voltage amplitude when this voltage is phase matched to the main RF signal. Here the main RF is set to the measured amplitude of 185 V.

of 36 nm/V, as shown in Fig. 3.2c. From the simulations, we estimate that it will require around 4.9 V to scan the trap location over a full fringe of the standing wave.

3.3 Precise Measurements of the Ion Micromotion

Micromotion differs in a fundamental way from the secular motion associated with the ion's oscillation in a harmonic potential. Micromotion is a driven motion of the ion responding to a non zero RF electric field. Unavoidable micromotion exists due to the secular motion taking the ion back and forth through the RF null. Excess

micromotion (EMM) beyond this can exist if a non-zero electric field at the ion's equilibrium position pushes it away from the RF null, or if there exists a phase difference between the voltages on any of the RF electrodes. A static electric field at the RF null can arise, for example, due to a mismatch between the RF and DC nulls or from stray charges in the trap or mirror surfaces close to the ion. Unlike secular motion, EMM cannot be reduced with cooling methods since it is a driven motion and does not conserve energy. To consider the micromotion caused by the presence of a stray DC field at the RF null, we follow the analysis of Berkeland et al. (1998) by adding a constant force term, $e\vec{E}_{dc} \cdot \hat{u}_i/m$, for an ion of charge e , to the right hand side of the Mathieu equations in Eqn. 2.4. The subsequent solution for the ion's motion along the i^{th} trap axis is given by

$$u_i(t) = (u_{0i} + u_{1i} \cos(\omega_i t + \phi)) \left(1 + \frac{q_i}{2} \cos(\Omega t) \right). \quad (3.1)$$

Here Ω is the angular frequency of the RF voltage and $u_{0i} = e\vec{E}_{dc} \cdot \hat{u}_i/(m\omega_i^2)$ is the displacement of the ion's equilibrium position along axis $i = (x, y, z)$ from the stray electric field \vec{E}_{dc} .

I used two methods to measure the micromotion amplitude for $^{174}\text{Yb}^+$ ions in the mirror trap. The first was the photon correlation method and the second was the parametric excitation method. The photon correlation method is based on measuring the correlation between the trap RF voltage phase and the fluorescence of the ion. As the ion's velocity is modulated by the RF voltage while undergoing micromotion, the Doppler shift with respect to the cooling light will also oscillate at the RF frequency, giving rise to a correlation between the ion's scattering rate and the RF voltage phase. This correlation can be observed by recording the time delay between a zero crossing of the RF field and the detected photon arrival time from the ion. A histogram of the photon detection times can be built up by observing the ion fluorescence from a red detuned laser over many RF cycles. As a compensation voltage is added to

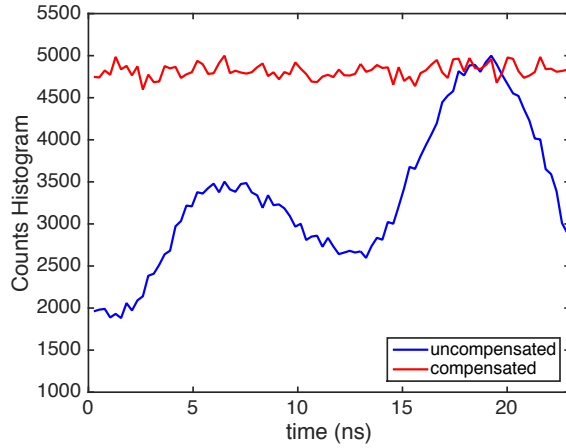


FIGURE 3.3: A photon correlation histogram with a RF period of 23 ns for uncompensated micromotion (blue histogram) and compensated micromotion (red histogram). This measurement is only sensitive to micromotion along the y-axis because the laser light has no component along the z-axis.

the DC electrodes, the ion can be moved back to the RF null location where this correlation is significantly reduced.

Detection of individual photons is done using a PMT (Hamamatsu H10682-110). The PMT operation is based on multiplying the photo-electron produced by an incident photon on the photocathode through several stages of dynodes, which can produce a charge amplification of $\sim 10^7$ that can readily be detected by an external readout circuit. I used a PMT to measure the count rate of photons emitted from the ion and collected into our detector. In Fig. 3.3, I show the result of adding a compensation field along the trap y-axis for reducing the correlations of the fluorescence histogram from the blue curve to the red curve.

One limitation of the photon correlation method in my current setup is that it is not sensitive to micromotion along the z-axis since the cooling laser is parallel to the trap surface, and therefore does not have a component perpendicular to the trap with which to detect a Doppler shift induced from the ion's micromotion in this direction. For this reason, I used another technique called the parametric excitation

(or “tickle”) method. This method is sensitive to displacements u_{0i} of the ion from the RF null which leads to EMM. It involves applying a small (~ -30 dBm) modulation to the RF voltage at the secular frequency associated with the ion’s motion in the trap, and uses the Doppler shift due to this secular motion rather than from the micromotion to detect the EMM. Since the cooling laser has a component along all three of the principal axes of the trap¹, parametric excitation in principle allows for compensation of micromotion along both radial trap directions. The size of the secular motion’s Doppler shift after excitation is proportional to the displacement of the ion, which in turn is related to the EMM amplitude from a DC offset field as given by Eqn. 3.1 (Tanaka et al., 2011). Fig 3.4 shows the excitation of the two radial trap modes from modulation of the RF signal. The higher frequency signal is from the motion along the z' axis and the lower frequency motion is along the y' axis. The prime axes are the rotated principal axis of the trap. These peaks also serve to identify the trap frequencies, which are around 5.08 MHz in the y' direction and 5.48 MHz in the z' direction. From these values, I found that the trap stability parameter in the z' direction was equal to $q_z = 2\sqrt{2}\omega_z/\Omega = 0.37$ and in the y' direction was $q_y = 2\sqrt{2}\omega_y/\Omega = 0.34$.

Comparing the measured trap frequencies with those found from the CPO trap voltage simulations allows us to determine the RF voltage amplitude used in trapping to be around 185 V. These values can then be used to find the EMM amplitude, a_i , as a function of the stray DC field with the equation (Berkeland et al., 1998)

$$a_i = \frac{q_i u_{0i}}{2} = \frac{\sqrt{2}eE_i}{m\omega_i\Omega}. \quad (3.2)$$

As compensation voltages are applied to both the inner and outer DC electrodes, I reduced E_i and the peaks were made much smaller, indicating a reduction in the

¹ Recall from Sec. 2.4.1 that the trap’s principal axes are rotated with respect to the x-y-z axes to allow for Doppler cooling of all three harmonic oscillation modes of the trap.

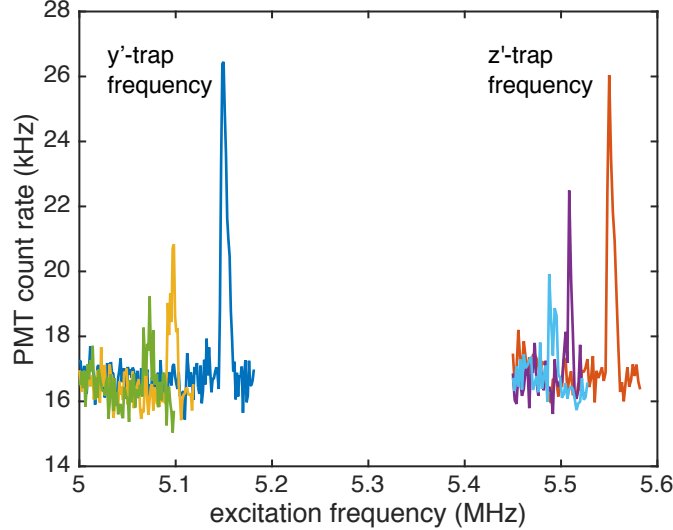


FIGURE 3.4: The parametric excitation method was used to minimize ion micro-motion. Since the side cooling beam has a component along all three principal trap axes, the Doppler shift due to an increase in secular motion when the ion is excited at one of its trap frequencies causes an increase in the scattering rate for red detuned light. As compensation voltages were applied to the DC electrodes to shift the DC null back to the RF null, the peaks were reduced in height and frequency.

EMM amplitude. In general, I was not able to make the peaks disappear completely, indicating some small amount of persistent EMM was present, likely due to charging in the mirror surface. Charging directly below the ion can create stray electric fields with smaller scale spatial variations than can be compensated for with the DC electrodes. Charging effects in the mirror trap are addressed in Sec. 3.5.

As noted previously, a mismatch in phase between the main RF signal and the tweaker RF signal can also cause EMM. Since we can control the phase for each signal from a DDS input independently, the degree to which the two signals can be matched is determined by the accuracy with which we can experimentally detect a phase mismatch. In practice, I measure the phase of the main RF signal from its pickup on the tweaker RF electrodes using the capacitive pickoff divider shown in Fig. 3.1b. This provides a reference with which to set the phase of the tweaker voltage to match

that of the main RF. Since the coupling between the main RF and the tweaker RF is primarily capacitive and the resistance is very low, only a very small phase difference is expected between the pickup signal on the tweaker electrodes as compared with the actual phase of the main RF voltage. To get an order of magnitude estimate for this phase difference, we calculate its value based on conservative estimates for the circuit resistances and capacitances. The capacitive coupling to ground from the pickoff capacitor circuit shown in Fig. 3.1b is $C_g = C_1C_2/(C_1 + C_2) = 4.8 \text{ pF}$, and we can estimate the capacitive coupling between the main RF and tweaker RF to be around $C_3 \approx 1 \text{ pF}$. The phase difference α of the pickup voltage between the two signals can be written in terms of the stray resistance R_s as $\tan \alpha = -(\Omega C_3 C_g R_s)/(C_g + C_3)$. With a conservative estimate of $R_s = 5 \Omega$, we find $\alpha = -0.0011$ radians, which is a negligible phase difference for our purposes. As a result, matching the phase of the two RF signals on the capacitive pickoff coupler measured with an oscilloscope should provide an accurate method for phase matching of the RF electrodes.

After reviewing several of the micromotion measurements I performed on the mirror trap, we can now return to consider our initial motivation behind adding a secondary set of RF electrodes to this trap (i.e. the tweaker electrodes). The purpose of these electrodes is to allow for translation of the RF null position in a continuous fashion without adding excess micromotion. This capability is important for the integration of the mirror trap with an optical cavity because the full performance improvements of the cavity can only be obtained when the ion is located at an antinode of the cavity's standing wave laser field. An alternative method to accomplish this would be to simply use the DC electrodes to push the ion away from the RF null towards an antinode if the two locations were not overlapping. However, this approach necessarily adds EMM that is proportional to the displacement u_{0z} from the RF null, as shown in Eqn. 3.1. In Fig. 3.5, I compare the effectiveness of our tweaker electrode approach with an alternative of simply using the DC electrodes

to push the ion without compensating for the EMM. This calculation uses Eqn. 3.2 to estimate the EMM added to the ion when moving it over the maximum required distance of $\lambda/4 = 92.5$ nm. For comparison, I also indicate the characteristic size of the ion’s wave function in a motional ground state with energy $\hbar\nu/2$, and the secular amplitude for an ion cooled to the Doppler energy limit of $\hbar\gamma/2$. From these results, we see that moving the ion over a distance of at least 30 nm introduces a significant amount of EMM amplitude that is larger than the secular motion amplitude, and therefore potentially problematic for applications in quantum computing.

The ability to minimize EMM is critical for remote entanglement applications using an ion in a cavity. Any micromotion along the cavity axis will translate to a frequency shift in the emitted photon from the ion. Since the heralded entanglement scheme we plan to use for generating remote entanglement requires the interference of two indistinguishable photons on a beam splitter, the presence of micromotion on one or both of the ions will lead to a difference between two otherwise identical photons and hence a loss in the entanglement fidelity. This would decrease the overall efficiency of the optical interconnects and should be avoided if possible.

3.4 Measuring the Ion Position in a Standing Wave

As a first step towards simulating the presence of an optical cavity with the mirror trap, we have designed an experiment to introduce a laser standing wave (SW) from light reflected off the mirror surface below the trap. A schematic of the experiment is shown in Fig. 3.6. The wavelength of the light used is that of the Doppler cooling transition $2S_{1/2} \leftrightarrow 2P_{1/2}$ for $^{174}\text{Yb}^+$ at $\lambda = 369.5$ nm. Laser cooling of single trapped ions in a SW has been investigated theoretically in the context of understanding how a two level atom in the Lamb-Dicke limit can experience sub-Doppler cooling dynamics in such a system (Cirac et al., 1992). The Lamb-Dicke limit refers to a regime where the spatial extent of the atom’s wave function is small compared to

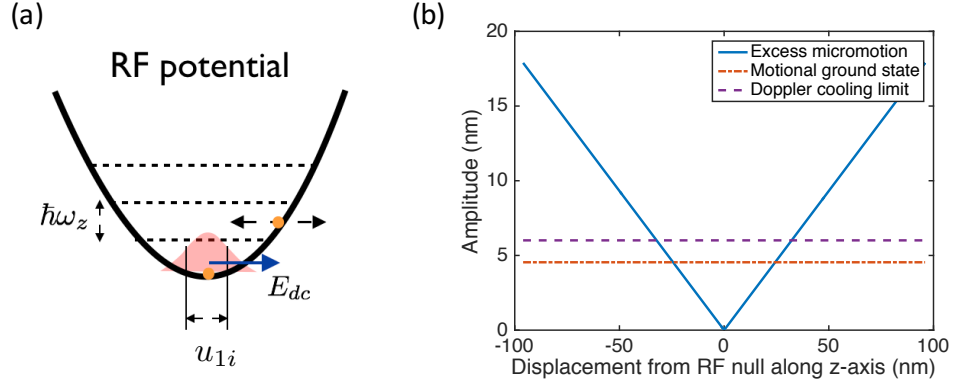


FIGURE 3.5: (a) A schematic depicting the origin of EMM from a displacement of the ion away from the RF null by a static electric field. (b) Simulations of the EMM amplitude from displacing the ion using the DC electrodes without adjusting the RF null position. For comparison, the amplitude of the ground state wave function and the amplitude of the secular motion corresponding to the Doppler cooling limit are plotted with the dashed dot and dashed lines, respectively.

the wavelength of the excitation light. This approximation applies to almost all ion trapping experiments, including the ones described in this thesis. Their findings concluded that the cooling rate of trapped ions in a SW depends strongly on which part of the SW the ion is in, including (somewhat counterintuitively) that there is (1) no cooling at the antinodes, (2) red detuned cooling in the vicinity of the nodes, and (3) blue detuned cooling in the position of steepest gradient of the SW, midway between a node and antinode. The range of the SW over which the ion experiences red detuned cooling depends on the ratio of the detuning Δ to the spontaneous emission rate, Δ/γ , and the ratio of the Rabi frequency Ω_0 to the spontaneous emission rate, Ω_0/γ . For large values of the light intensity, such as $\Omega_0 = 6\gamma$ for example, the ion actually experiences heating from a red detuned laser away from a node of the SW. Furthermore, ions in a spatially inhomogeneous field, such as a SW, experience a force due to the spatial gradient of the light field, called the dipole force. This force is generated from absorption and subsequent stimulated emission of photons into oppositely traveling components of the SW, and can be much larger

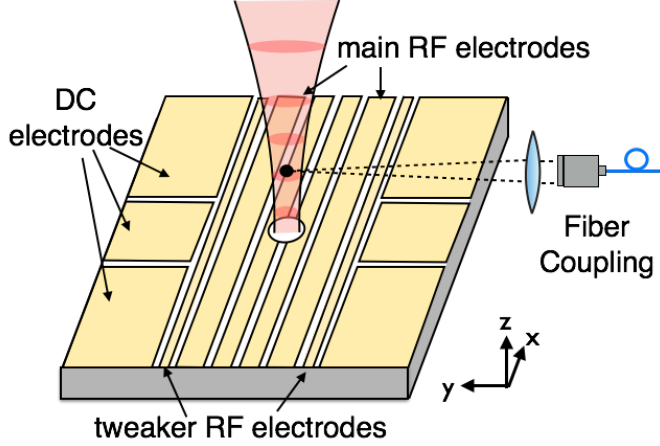


FIGURE 3.6: A schematic of the standing wave experimental configuration showing the standing wave incident on the mirror surface under the trap and the fiber collection optics for measuring the ion's fluorescence.

than the maximum dissipative force from a traveling wave, which is $F_{max} = \hbar k \gamma / 2$ for a wave vector with magnitude k . These findings all serve to highlight the rich interplay of light-atom interactions in this rather simple system. Based on the results reported in Cirac et al. (1992), I determined the appropriate intensity and detuning parameters for the laser that forms the SW to set it in a regime where it is cooling the ion for nearly the entire range of the SW. This includes using an intensity where the Rabi frequency is less than the spontaneous emission rate and the detuning is set to approximately one linewidth away from resonance.

Since the SW beam is incident on the trap through the front viewport and focused down to a spot size of several microns by the imaging lens², this same lens cannot be used for also collecting light into the PMT because the reflection of the SW light will completely saturate the PMT counts. Instead, I collected the photon emission from the ion through one of the side 2-3/4 inch viewports of the vacuum chamber. I used a single mode optical fiber to couple light into a PMT and filter out any 370 nm light which may have come from laser scatter off the trap and not the ion fluorescence.

² See Fig. 2.12 for a picture of the experimental setup.

The count rate of photons collected from the ion in this setup depends on both the numerical aperture of the focusing lens and on the coupling efficiency into the fiber. To maximize the collection rate, I used a large aperture fiber collimator from Micro Laser Inc., the FC10-VIS1-T/A model, with a 10 mm clear aperture and a ~ 5.5 mm $1/e^2$ beam size. The distance from the center of the trap to the outer edge of the viewport is about 110 mm, so I used a single plano-convex fused silica lens AR coated for UV wavelengths with a focal length of 125 mm to collect light into the fiber. Initial alignment was carried out by directing resonant laser light through the detection fiber and scattering it off the ion. Once the scattering was maximized, I cooled the ion with a separate side cooling beam and the scattered photons were collected into the fiber. The collected photons in the fiber were directed into a PMT, and the detected count rate was further maximized by adjusting the lens and fiber positions. We can estimate the collection efficiency from a calculation of the $NA \approx D/2f$ to be $\epsilon \approx 1 \times 10^{-4}$. This setup allows for photon detection rates in the 500 - 1000 cps (counts per second) range with a very low rate of background counts limited only by the dark count rate of the PMT, which is roughly 10 cps.

As described previously, the intensity of the SW beam is a critical parameter for determining the ion's heating and cooling dynamics. The intensity must be low enough such that $\Omega_0 \leq \gamma$ in order to efficiently cool the ion over the entire SW period. However, if the intensity is too low, the scattering rate signal to noise ratio will decrease and the sensitivity will be diminished. To measure the optical intensity of the SW beam, I used a calibrated power meter and measured the beam waist from the image of the beam scattering off the trap surface on the Andor EMCCD camera. A picture of the SW beam on the trap is shown in Fig. 3.7. The pixel spacing of the camera is $16 \mu\text{m}$, and the magnification of the imaging system is 8.3. I have fit the SW intensity distribution with a Gaussian beam profile, and find a waist of radius of $4.2 \mu\text{m}$ in the horizontal direction and $4.8 \mu\text{m}$ in the vertical direction. I used

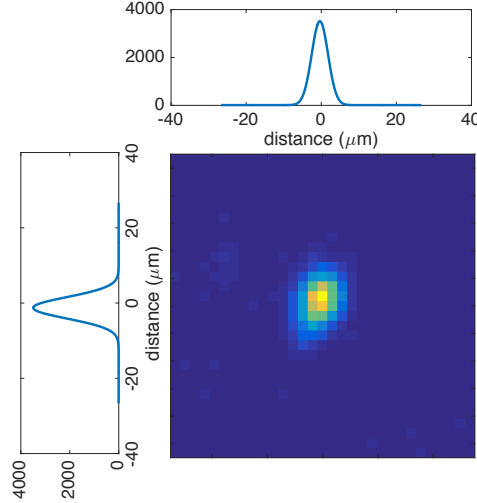


FIGURE 3.7: The standing wave beam profile with Gaussian fits indicating a waist of $4.2 \mu\text{m}$ in the horizontal direction and $4.8 \mu\text{m}$ in the vertical direction.

optical powers in the range of $40 - 80 \text{ nW}$, which corresponded to intensities in the range of $60 - 130 \text{ mW/cm}^2$.

A complete description of the ion's fluorescence in the SW must take into account the effects of micromotion on the scattering rate. If we transform to the ion's frame of reference, the cooling laser will appear as if it is phase modulated at the RF frequency due to the presence of any z -axis micromotion. This will give rise to sidebands in the SW laser's frequency at integer multiples of Ω . We can subsequently write the laser's electric field at the ion location for a micromotion amplitude of a_z as

$$E(z, t) = 2E_0 \sin(kz) \exp(-i\omega_0 t) \exp(ika_z \sin(\Omega t)). \quad (3.3)$$

The second exponential term can be expanded in terms of Bessel functions as

$$\exp(ika_z \sin(\Omega t)) = \sum_{n=-\infty}^{\infty} J_n(\beta) \exp(in\Omega t), \quad (3.4)$$

where we have defined the modulation parameter $\beta = ka_z$.

The effect of micromotion will be to both oscillate the ion around its equilibrium

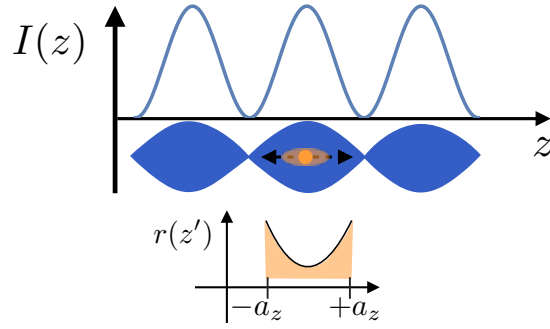


FIGURE 3.8: A schematic of the convolution of the ion’s motion, modeled with the function $r(z')$, with the spatially varying intensity field of the standing wave.

position and add modulation sidebands to the laser frequency. For a SW, these oscillations give rise to both a frequency modulation and an amplitude modulation of the field intensity at the ion. Using the side fiber coupling of the ion’s fluorescence, I measured directly the spatial field intensity $I(z)$ of the SW along the z-axis by monitoring the spontaneous emission rate of the ion as a function of its height above the trap, which in turn was a function of the tweaker voltage. Our model takes into account the effects of the ion’s micromotion oscillations using the normalized spatial distribution of the ion over one period of its motion as $r(z') = 1/\pi\sqrt{1/(a_z^2 - z'^2)}$ for $-a_z < z' < a_z$. The ion’s scattering rate in the SW can be written as a convolution of the ion’s motion with the modulated scattering rate for an ion at rest as

$$S_{sw}(z, \Delta) = \int_{-a_z}^{a_z} r(z') S(z - z', \Delta) dz', \quad (3.5)$$

where $S(z, \Delta)$ is the scattering rate from the field intensity $I(z)$ with detuning Δ . The rate $S_{sw}(z, \Delta)$ is what we measured with the side fiber coupling to determine the ion’s height above the trap with nanometer scale precision.

I measured the scattering rate of Eqn. 3.5 by collecting photons into a PMT through the side optical fiber, and observed clear oscillations in the photon counts as the ion was moved through the SW. To calibrate the voltage scale, I measured the

periodicity of these oscillations as a function of the input voltage slope. The tweaker amplitude voltage as a function of the DDS input power measured with the pickoff voltage capacitors for various levels of input attenuation is shown in Fig. 3.2a. The periodicity of the scattering rate oscillations with the DDS input power converted to tweaker voltage can be found from a sine fit of the detected counts and is shown in Fig. 3.9 for varying levels of input power attenuation. Each data point in this figure is the average count rate of fifty experiments, where the ion is exposed to the standing wave for 120 ms with 20 ms of Doppler cooling in between. As the DDS power is attenuated by 2 dB between scans, the period of the oscillations changes by around 80%, consistent with the expected change of the tweaker voltage between scans. A full period of the oscillations corresponds to a movement of the ion over a distance $\lambda/2 = 185$ nm. From the simulation results shown in Fig. 3.2c, we find that a translation of the RF null position over 185 nm corresponds to a tweaker amplitude increase by 4.9 V. For the -5 dB attenuated scan, this corresponds to a DDS amplitude change of $a = 323.4$, giving a slope of 0.0152 V/a. For the other two attenuation values of -1 dB and -3 dB, the slopes are 0.0184 V/a and 0.023 V/a, respectively. Together, these results provide a good calibration for measuring the voltage amplitude being applied to the tweaker electrodes and indicate a roughly 10% discrepancy with the direct voltage measurement, which is well within the range of uncertainty as discussed in Sec. 3.2.

For the parameter regime of $^{174}\text{Yb}^+$ where the trap frequency is less than the spontaneous emission rate, spontaneous emission must be taken into account as a damping force on the ion's motion. Spontaneous emission as a decay process of the excited state of a two level emitter (TLE) is discussed in the context of the Doppler cooling of a trapped ion in Sec. 2.2. The complete dynamical picture for the interaction of a TLE with a light field is governed by the optical Bloch equations (OBE), which include the effects of stimulated emission and absorption with the

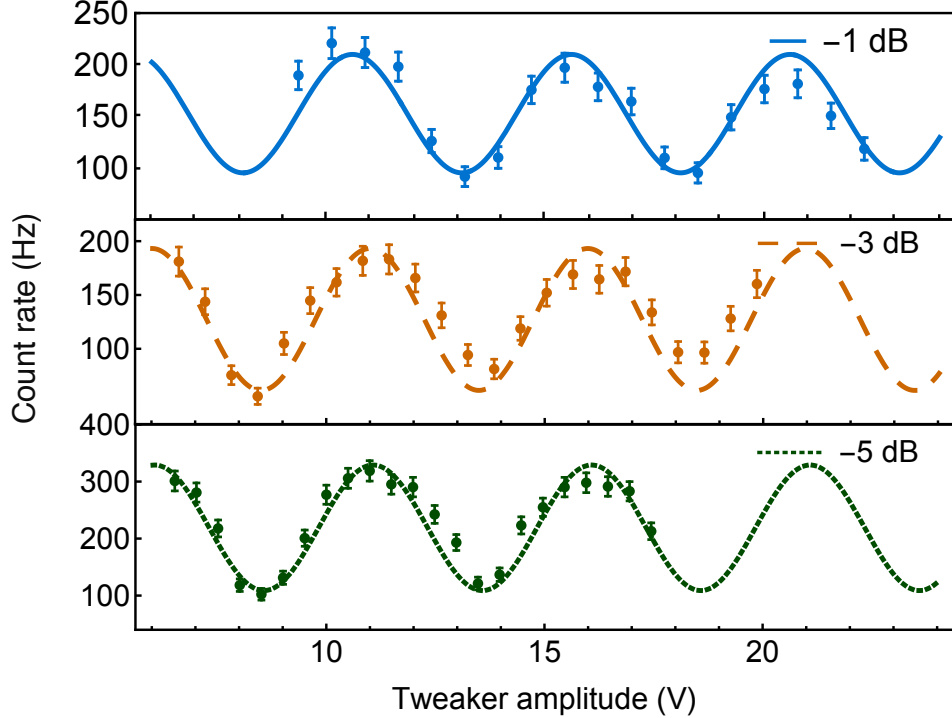


FIGURE 3.9: Oscillations in the ion scattering rate as a function of the tweaker voltage for various levels of input attenuation and a SW laser detuning of $\Delta/2\pi = -10$ MHz. The data is fit to a sine function to extract the periodicity of the oscillations, which correspond to an ion translation of $\lambda/2 \simeq 185$ nm. We calibrate a full period of oscillation to an ion height change of $\lambda/2$, which from our trap simulations corresponds to a tweaker voltage of 4.9 V.

spontaneous emission decay process and can be used to solve for the density matrix ρ of the TLE in a light field (Metcalf and van der Straten, 1999). For a steady state solution of the OBE, the total scattering rate of the laser will be $S = \gamma\rho_{ee}$, where ρ_{ee} is the excited state population and γ is the transition linewidth. To understand the scattering of the ion at different parts of the SW, we use a model of $S(z, \Delta)$ which incorporates the modulation caused by the micromotion into the scattering rate in the low intensity limit (Metcalf and van der Straten, 1999; Cirac et al., 1993). The stipulation for the low intensity limit of this equation will hold near the node of the SW. At the antinode, the field intensities can be on the order of $I_{sat} = 2\pi^2\hbar\gamma c/3\lambda^3$ or

greater and saturation effects cannot be ignored. Saturation effects can be included into the scattering rate model by numerically integrating the master equation of a laser interacting with a TLE in the presence of a sinusoidally varying SW. In general, however, these effects will cause a shift in the height, width, and frequency of the micromotion sidebands as the intensity is increased (Keller et al., 2015). At the node of the SW, the light intensity goes to zero and consequently there is no saturation due to the possibly strong carrier laser at ω_0 , but the sidebands at $\omega_0 \pm \Omega$ will still scatter light without saturation at a rate proportional to the intensity (Cirac et al., 1994). In this low intensity limit, we can use a model for the scattering rate at the node in terms of the micromotion sidebands as

$$S(z, \Delta) \approx \frac{\gamma}{2} \frac{I(z)}{I_{sat}} \sum_n \frac{J_n(\beta)^2}{1 + (2(\Delta + n\Omega)/\gamma)^2}. \quad (3.6)$$

Substituting Eqn. 3.6 into Eqn. 3.5 gives a model that can be used to calculate $S_{sw}(z, \Delta)$ as a function of the ion's position around the SW node and the laser detuning. Fig. 3.10 shows the fit of the scattering rate as a function of detuning Δ taken at the node of the SW. Here we fit three different scattering curves using Eqn. 3.6, and find the micromotion amplitude from the modulation parameter β . For the case of a large micromotion amplitude of ~ 40 nm, the lineshape begins to show effects of saturation as the micromotion and main transition sidebands become wider and the sideband peak shifts in frequency relative to our model's prediction. Numerical solutions of the micromotion sideband for an ion cooled with a traveling wave predicts this type of behavior as the intensity of the cooling beam is increased (Keller et al., 2015).

At the antinode of the SW where the intensity is higher, second order effects including two photon processes must be taken into account when solving for the scattering rate. While this requires a numerical solving of the OBE master equation

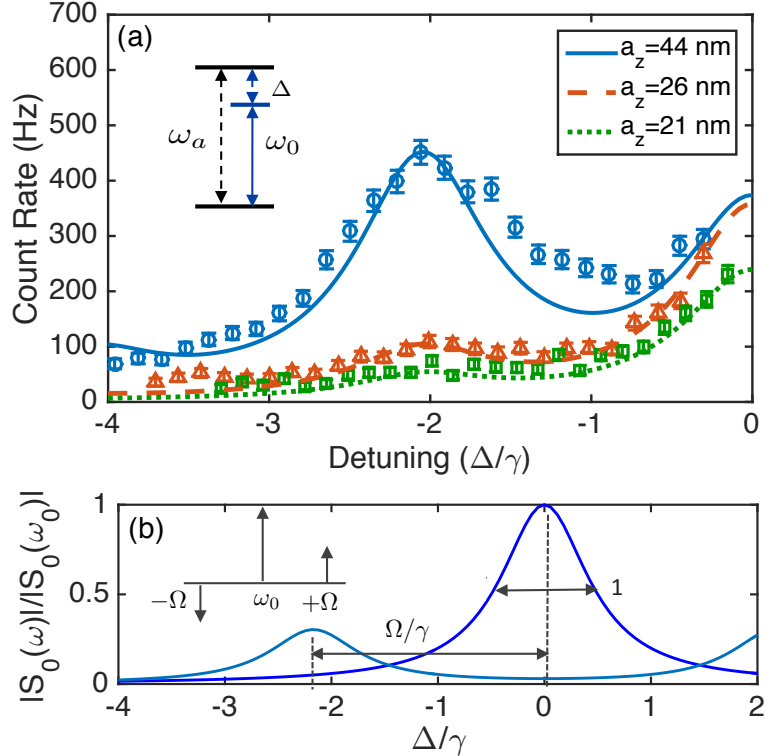


FIGURE 3.10: (a) The measured photon counts from an ion near the standing wave node as a function of laser detuning, with the fit curves found from the empirical model of Eqn. 3.5 for several micromotion amplitudes. (b) Schematic representation of the laser frequency as seen in the frame moving with the ion. The micromotion causes the ion to see a phase modulated light field with sidebands above and below the carrier frequency.

(which is not explored further in this work), we can still gain some intuition about the scattering rate at the antinode by fitting the measured data to the steady state solution of the OBE for an ion at rest and close to resonance as

$$S_0(\Delta) \approx \frac{\gamma s_0}{2} \frac{1}{1 + s_0 + (2\Delta/\gamma)^2}, \quad (3.7)$$

where $s_0 = I_0/I_{sat}$ is the saturation parameter. From the fit to the data, we can find the power-broadened linewidth of the transition $\gamma' = \gamma\sqrt{1+s_0}$ to get an approximation for the intensity I_0 . Data for two lineshapes at a node and antinode along with their respective fit curves is shown in Fig. 3.11. This data shows how the

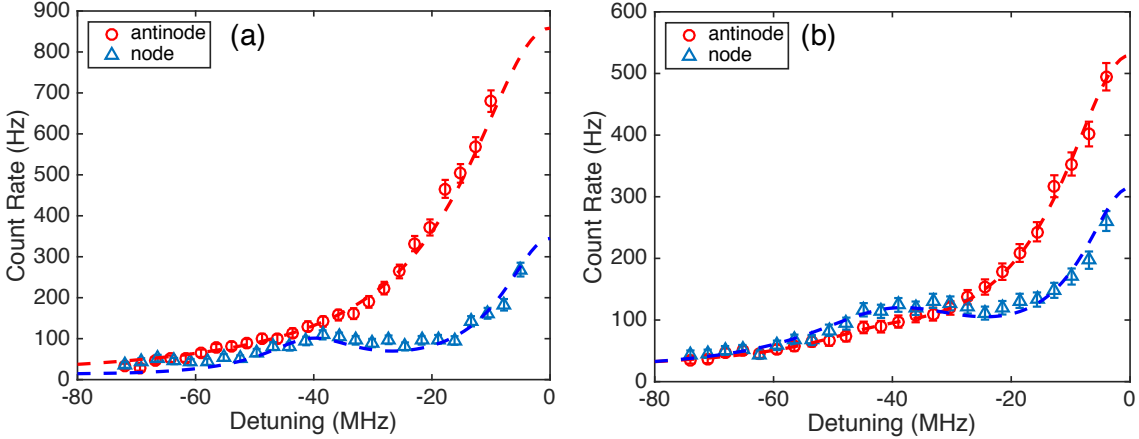


FIGURE 3.11: The measured ion scattering rate as a function of laser detuning at the node and antinode. (a) At the antinode, a saturation parameter fit of $s_0 = 2$ is found for Eqn. 3.7. At the node, Eqn. 3.6 is used as a fit to the data. (b) As the micromotion amplitude is increased, the scattering rate near $\Delta/2\pi \approx -42$ MHz grows larger for the node than the antinode, indicating a higher overall scattering rate at the micromotion sideband for the node compared with the antinode.

micromotion sideband height at the node can increase above that of the antinode for sufficiently large micromotion amplitudes.

The potential for ion heating from a red detuned laser of high intensity (Cirac et al., 1992) or at a frequency just above a micromotion sideband (DeVoe et al., 1989) has led us to investigate whether an increase in the motional energy of the ion by the SW has led to an increase in micromotion at the node as compared with the antinode. To account for this possibility, I measured the relative height of the micromotion sideband peak to the carrier peak for various detection times over which the ion was exposed to the SW field at both a node and an antinode. I found that the size of both the sideband and the carrier peak did not change significantly over detection times from 20 ms all the way out to 1 second (Fig. 3.12). This signifies that the motional heating induced micromotion, which would cause the peak height to increase over exposure time to the SW as the ion gained motional quanta of energy, turns out to be negligible in this case. The size of the sideband did change

significantly, however, depending on in which part of the SW the ion was located. We can explain this from saturation effects which suppress and shift the sideband peak at the antinode position relative to the node. This effect is apparent in Fig. 3.12a as the sideband height of the node has become larger than that of the antinode for a sufficiently high modulation parameters of $\beta \approx 1.5$.

The scattering rate of the ion as it moves through a full two periods of the SW is shown in Fig. 3.13, along with the fit curve found from the convolution model of Eqn. 3.5 and the scattering rate in Eqn. 3.6. This fit is only an approximation since we expect the scattering rate at an antinode to include saturation effects not accounted for in our model. For this reason, we added a saturation parameter $s_0 = I_0/I_{sat}$, such as in Eqn. 3.7, to the scattering model to provide an empirical fit parameter for the entire curve which reproduces the wider peaks at the antinode compared with the narrow valleys of the nodes. The other input parameters to this model are the input traveling wave intensity of $I_0 = 126 \text{ mW/cm}^2$, corresponding to a

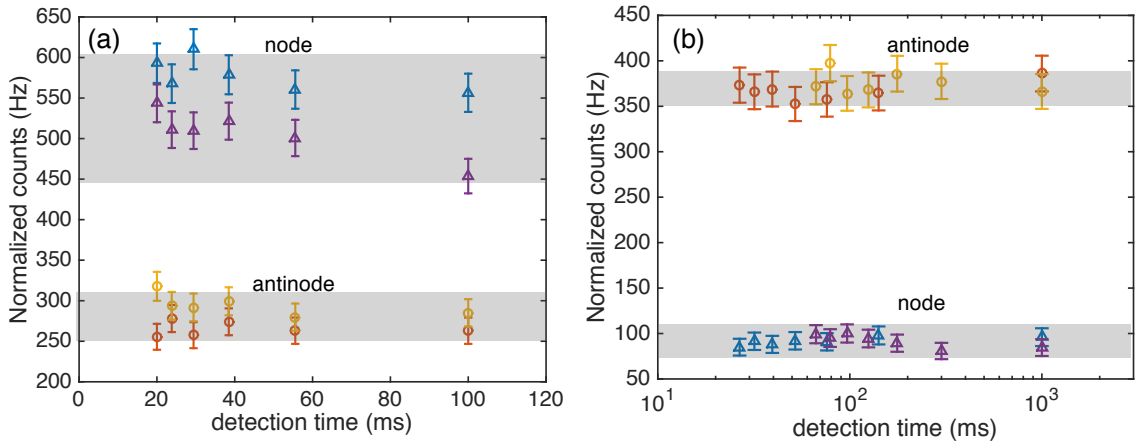


FIGURE 3.12: The average photon scattering rate for various exposure times to the standing wave for the case of (a) the micromotion sideband peak at $\Delta/2\pi = -40 \text{ MHz}$ and (b) closer to resonance at $\Delta/2\pi = -10 \text{ MHz}$. This data was taken for an ion with a sufficiently large micromotion amplitude to cause an inversion in the scattering rates between the node and antinode at the micromotion sideband, as shown for example in Fig. 3.11b.

Rabi frequency of $\Omega_0/\gamma = \sqrt{I_0/2I_{sat}} = 1.1$, and a near unity reflectance of the mirror coating at the 370 nm wavelength. The micromotion amplitude also enters into the spatial probability distribution $r(z')$ to determine the visibility of the fit, defined as $V = (S_{max} - S_{min})/(S_{max} + S_{min} - 2b)$, where S_{max} is the maximum of the scattering rate along the standing wave, S_{min} is the minimum scattering rate, and b is the background counts on the detector PMT. Since the PMT has a 370 nm optical bandpass filter and is connected directly to an optical fiber, the background counts are mainly due to the detector's dark counts and measured to be $b \approx 14$ Hz. For a detuning of $\Delta/2\pi = -20$ MHz, we used our model in Eqn. 3.6 with the voltage calibration from Fig. 3.9 to fit a scan of the scattering rate as a function of the tweaker voltage amplitude. The amplitude of the micromotion found for this fit was $a_z \approx 20$ nm, and the fiber collection efficiency was $\epsilon_f = 4.4 \times 10^{-6}$. As before, each data point represents the average of fifty measurements of the ion scattering rate in the SW for 120 ms with 20 ms of cooling from a side laser between each measurement.

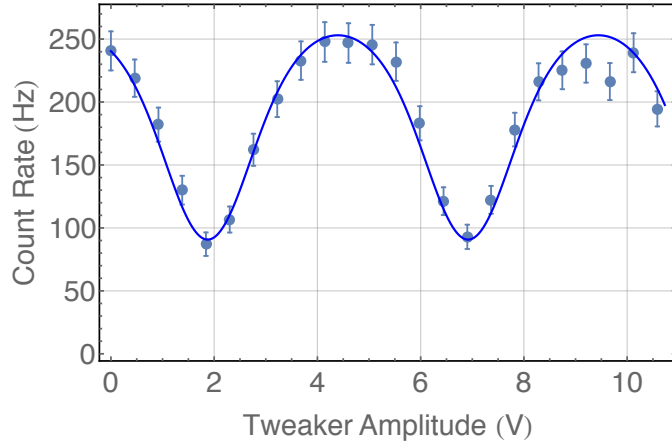


FIGURE 3.13: The ion scattering rate in a $\Delta/2\pi = -20$ MHz detuned standing wave as a function of the tweaker voltage with a convolution fit of the micromotion. The fit curve has a micromotion amplitude of $a_z \approx 20$ nm and a side light collection efficiency of $\epsilon_f = 4.4 \times 10^{-6}$.

3.5 Charging Effects of the Mirror Surface

Exposure of dielectric mirror coatings to UV light is known to introduce positive charge into the material from the ejection of electrons from the HR coating (Harlander et al., 2010). This charge introduces a significant repulsive force directly beneath the ion, pushing it away from the area where the SW beam is incident on the mirror. We can model these charging effects with a charge distribution that is proportional to the incident laser intensity. The intensity profile of the SW on the mirror was imaged using the Andor EMCCD camera and is shown in Fig. 3.7. The electric field on the center axis due to a Gaussian charge distribution of $Q(r, t) = Q_0(t) \exp(-r^2/\sigma^2)$ on the mirror surface a distance z_0 above the surface is given by the following integral

$$E_z(t) = \frac{Q_0(t)z_0}{2\epsilon_0} \int_0^\infty e^{-r^2/\sigma^2} \frac{r}{(z_0^2 + r^2)^{3/2}} dr. \quad (3.8)$$

For $\sigma = 5 \mu\text{m}$ and $z_0 = 50 \mu\text{m}$, this integral evaluates to

$$E_z(t) = 2.8 \times 10^{-8} Q_0(t). \quad (3.9)$$

By finding the rate of increase in the electric field $E_z(t)$ at the ion's position, we can find the charging rate of the mirror as $dQ_0(t)/dt$. I measured this charging field as a function of laser exposure time by measuring the displacement of the ion's position relative to the SW in response to the SW. These results are shown in Fig. 3.14a. I then calibrated this result to find the charge density on the mirror as a function of time, $Q_0(t)$. The ion's equilibrium position as a function of the DC field is given in Eqn. 3.1 as u_{0z} . From the measured velocities of the three curves shown in Fig. 3.14, the electric field as function of time can be found as

$$\frac{dE_z(t)}{dt} = \frac{m\omega_z^2}{e} \frac{dz}{dt}. \quad (3.10)$$

For the highest intensity beam tested of 184 mW/cm^2 , the velocity was 0.282 nm/s , for the 142 mW/cm^2 intensity the velocity was 0.17 nm/s , and for 64 mW/cm^2 the

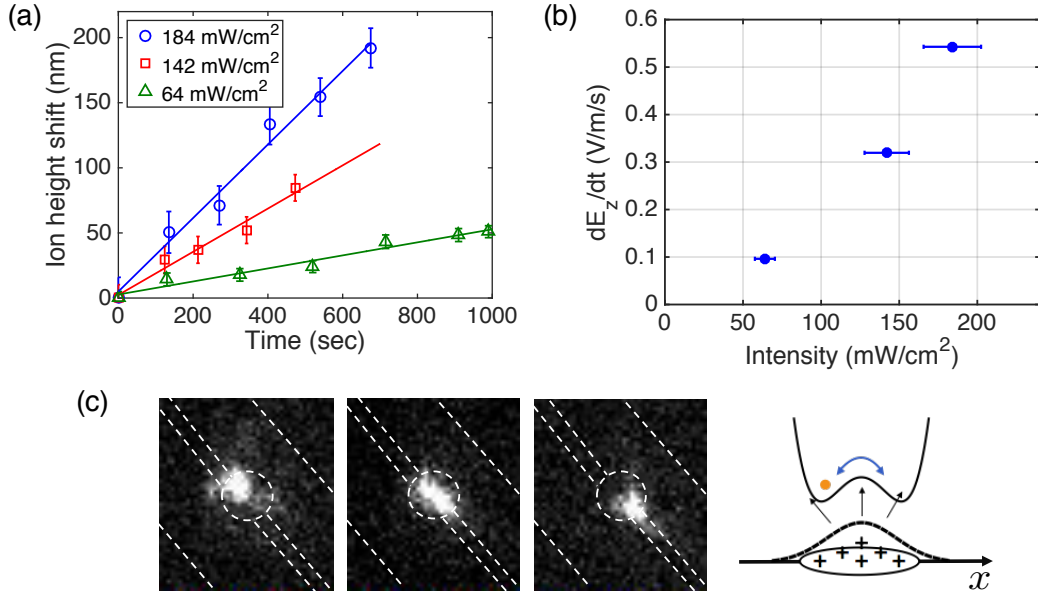


FIGURE 3.14: (a) The charging rate of the mirror surface below the trap can be found from the change in the ion's height above the trap relative to the standing wave. (b) The ion's velocity for different intensity standing wave beams can be converted into an electric field rate of change using Eqn. 3.10. (c) An extreme case of charging occurs if the standing wave has too much power or is left on for too long, where the harmonic potential bifurcates along the axial direction into a double well structure due to the strong field from positive charges accumulating on the mirror surface. The ion can make discrete jumps between each minima (first and last picture) or, when placed exactly between the two minima (middle picture), it hops back and forth between the two minima and its image is spread along the axial direction.

velocity was 0.05 nm/s. From this data, we can measure the rate of change of the electric field at the ion location as a function of laser intensity, as shown in Fig. 3.14b. Due to the increase in the charging rate as a function of the incident light intensity, for higher intensities the ion becomes more unstable to the point where the harmonic potential along the axial direction can even bifurcate into two potentials as shown in Fig. 3.14c.

The potential for charging of the mirror surface below the trap is certainly a potential drawback of the mirror trap design. However, our analysis has shown that

for short times and low powers, the field generated from the charging $E_z(t)$ increases linearly with time and can be compensated for by adjustments of the inner DC electrode voltages. For the eventual use of light collection from an ion in a cavity, no UV light is stored in the cavity. Only a 780 nm stabilization laser is needed for this application, and these substrates do not charge significantly at these IR wavelengths. For the qubit state detection applications, the probe laser is turned on for short time scales on the order of 1 μ s, which will cause only negligible charging with intensities < 50 mW/cm², and we expect the influence of any charging to be controllable. Although the beam may have to be on for a significantly longer time for alignment purposes, in my experience the relatively small amounts of charge considered here will dissipate over the course of 24 hours without exposure to UV laser light.

3.6 Ion Trap Outlook and Summary

In this chapter, I have presented extensive testing results of the mirror trap I have fabricated, which is one of the first implementations of a surface trap on a dielectric mirror surface. The trap performance was characterized in terms of the trap lifetime, trap depth, excess micromotion, effectiveness of the tweaker electrodes for changing the ion height, and charging rate of the mirror surface under the trap. The use of separate RF electrodes for adjusting the ion height is also a novel feature of our trap, providing the first demonstration of a continuous trap height adjustment over a surface trap with nanometer scale precision. While our motivation for this feature is towards integration with an optical cavity, such a capability also has other applications in the field of ion trapping, including for use in suppression of the sideband coupling strengths in a SW gate beam (deLaubenfels et al., 2015) and increasing fiber coupling from a fiber integrated surface trap (VanDevender et al., 2010; Kim et al., 2011b). Our approach can provide significant benefits for these applications (and possibly others) since the ion can be moved perpendicular to the

trap without adding EMM from displacement away from a fixed RF null position.

The study of laser cooling in a SW is a complex topic owing to the competition between the potentially strong dipole forces of the laser field gradient and the dissipative spontaneous emission process (Dalibard and Cohen-Tannoudji, 1985). While some theoretical models do exist for the low intensity regime around the nodes, the enhancement of stimulated emission into either of the standing wave components makes this rate comparable to γ for higher intensities around the antinodes, and closed form theoretical solutions break down as two photon scattering processes become significant. Nevertheless, we have developed a model to fit the ion's scattering function at the SW node, $S_{sw}(z, \Delta)$. This effectively models the periodic fringes of the scattering rate as the ion's height within the SW is adjusted by the tweaker electrodes. Intricacies of the SW cooling aside, we have shown the unique ability with our method to effectively adjust the height of the RF null above the trap in a continuous fashion and with nanometer scale precision, which is a necessary capability towards future integration of surface traps with optical cavities.

4

Cavity Theory and Simulations

4.1 Integrated Ion Trap and Optical Cavity Design

The field of cavity quantum electrodynamics (QED) is concerned with the interaction of optical cavities with atoms. Cavity QED systems are characterized by an oscillatory exchange of energy between an atomic system and the cavity mode. The rich interplay between photons in the cavity and electronic transitions of the atoms gives rise to exotic quantum mechanical behavior which is highly relevant to trapped ion quantum computation. We will investigate two applications of such a system in this chapter, namely efficient photon collection and fast qubit state detection.

All of the various trapped ion systems utilize transitions between the internal electronic states of the ions to interact with them. This includes exciting atomic transitions by applying resonant laser light to the atom and measuring the rate of emitted photons. The emission of photons from an atom can occur either through stimulated emission, where an incoming photon induces an atomic electron in an excited state to decay to the ground state and emit another photon into the same optical mode, or by spontaneous emission, where the excited state spontaneously

decays to the ground state (Saleh and Teich, 2007). In both cases, the rate of the process is proportional to the transition cross section of the atom at the resonance frequency and inversely proportional to the mode volume of the surrounding space. By enclosing the light surrounding the atom in a small mode volume, the rate of these interactions can be significantly increased. Furthermore, in the case of spontaneous emission into free space, the photon is emitted in a random direction over the full 4π solid angle due to the symmetry of the mode. Introducing an optical cavity surrounding the ion breaks this symmetry and can significantly increase the spontaneous emission rate into the cavity mode relative to all other modes by increasing the density of states in that mode. The optical cavity therefore provides the capability for dramatic changes to the photon emission profile, which has several potential applications for quantum computation with trapped ions.

Our cavity system uses an optical Fabry-Perot cavity made up of two highly reflective mirrors which can support standing waves at evenly spaced resonant frequencies. The resonance condition of the cavity is that the electric field acquires an integer multiple of 2π phase shift for each round trip transit through the cavity. This condition can be summarized as requiring an integer number of half wavelengths to fit inside the cavity, or $n\lambda/2 = l$, for a cavity of length l and light of wavelength λ . Resonant solutions to the cavity condition with the same spatial profile, called longitudinal modes, are separated in frequency by an integer multiple of the free spectral range, $\nu_f = c/2l$. Spherical mirrors of radii R_1 and R_2 can provide a stable configuration with which to confine the light rays reflecting off each mirror provided the length of the cavity satisfies the confinement condition

$$0 \leq \left(1 - \frac{l}{R_1}\right) \left(1 - \frac{l}{R_2}\right) \leq 1. \quad (4.1)$$

It is common to write this condition in terms of the g -parameters, $g_1 = 1 - l/R_1$ and $g_2 = 1 - l/R_2$, as $0 \leq g_1 g_2 \leq 1$. We consider here a hemispherical cavity

arrangement with $R_1 = \infty$, where the stability condition reduces to the requirement that the cavity length cannot exceed the radius of curvature of the second mirror, or $0 \leq l \leq R_2$.

In addition to the stability condition provided by a ray tracing analysis, the spatial intensity distribution of the cavity mode must also match the mirror profile for the mode to be stable. The wave solutions for the cavity modes are well approximated as solutions to the paraxial Helmholtz equation, with a generic solution being the Gaussian beam (Saleh and Teich, 2007). The Gaussian beam is characterized by a beam size $w(z)$, wavefront radius of curvature $R(z)$, and Rayleigh length z_R by the following equations

$$w(z) = w_0 \sqrt{1 + \left(\frac{z}{z_R}\right)^2} \quad (4.2)$$

$$R(z) = z \left[1 + \left(\frac{z_R}{z}\right)^2 \right] \quad (4.3)$$

$$z_R = \frac{\pi w_0^2}{\lambda}. \quad (4.4)$$

Here w_0 is called the mode waist, which is the radius of the beam at its smallest size which encloses 86.5% of the total power. The resonance condition requires that the cavity mode radius of curvature match that of the mirror, which for our hemispherical cavity design means $R_1 = \infty$ at the beam waist and $R_2 = l(1 + (z_R/l)^2)$ at the curved mirror a distance l away from the waist. We use these Gaussian beam parameters to characterize the mode profile for the optical cavities we have made. In addition to the cavity length and the radii of curvature of the mirrors, other important quantities for describing the cavity include the mirror reflectance, losses, and aperture size. All these quantities factor into the overall performance and suitability of an optical cavity for cavity QED experiments.

A suitable description of how a cavity interacts with an atomic system begins with a quantization of the EM field as a duality of discrete photons and a traveling wave. In terms of the photon creation and annihilation operators, \hat{a}^\dagger and \hat{a} , we can write the EM field as

$$\hat{E} = E \sin(kz)(\hat{a} + \hat{a}^\dagger), \quad (4.5)$$

with the quantized field strength $E = \sqrt{\hbar\omega/2\epsilon_0V}$. Here V is the volume of the optical cavity mode and ω is the angular frequency of the light. The mode volume is the spatial volume of the resonant mode inside the cavity. A full description of the cavity QED system is given by the Jaynes-Cummings Hamiltonian,

$$\mathcal{H} = \hbar\omega_c \hat{a}^\dagger \hat{a} + \hbar\omega_a \frac{\hat{\sigma}_z}{2} + \mathcal{H}_{int}. \quad (4.6)$$

The first two terms in this Hamiltonian describe the energy of the cavity and ion system, respectively, while the final term is called the interaction Hamiltonian and describes the coupling between the atom and the quantized EM field. The field couples to the dipole moment of the intra-cavity atom between its excited and ground state energy levels, written as $d_{eg} = |\langle e | \vec{e} | g \rangle|$. The dipole moment quantifies the difference in the electron charge distribution between the ground and excited states of the atom, and the electric field must have a component along this direction in order to drive a transition between the two quantum states. The interaction Hamiltonian is often written in the rotating wave approximation (RWA) where terms which oscillate at the higher frequency $\omega_a + \omega_c$ are neglected, and the interaction is written in terms of the atomic transition operators from state $i \rightarrow j$ ($\hat{\sigma}_{ij}$) as

$$\mathcal{H}_{int} = g\hbar(\hat{a}\hat{\sigma}_{ge} + \hat{a}^\dagger\hat{\sigma}_{eg}). \quad (4.7)$$

The quantity g is the coherent rate of energy exchange between the ion and the field for both the absorption of a photon and transition to the excited state of the emitter

$(\hat{a}\hat{\sigma}_{ge}$ term) and the decay of the excited state and emission of a photon ($\hat{a}^\dagger\hat{\sigma}_{eg}$ term). This rate depends on the atom's dipole moment and the electric field magnitude in the direction of the dipole moment, and is given by

$$g = d_{eg} \sqrt{\frac{\omega}{2\epsilon_0 V \hbar}}. \quad (4.8)$$

The dipole moment is a fundamental property of the atom, and is related to the spontaneous emission rate γ and the angular frequency ω of the electronic transition as $d_{eg}^2 = 3\pi\epsilon_0\hbar\gamma c^3/\omega^3$. The atomic system we are interested in is the $^{171}\text{Yb}^+$ ion with an electronic structure as described in Sec. 2.2. The main atomic transition used for cooling, qubit state initialization, and qubit measurement is the $^2S_{1/2}$ to $^2P_{1/2}$ transition at 370 nm wavelength.

The ion-photon energy exchange rate, g , is only one of the important rate parameters for describing the dynamics of a cavity QED system. Two of the other important parameters are the rate of photons decaying from the cavity mode, which is given by 2κ with $\kappa = \pi\nu_f/\mathcal{F}$, and the spontaneous emission rate of the atom, γ . The cavity decay rate κ is a function of the mirror loss rate per reflection, here written in terms of the mirror transmission T and losses L as the finesse $\mathcal{F} = 2\pi\sqrt{1 - (T + L)/(T + L)}$, and the rate at which photons hit the mirrors, given by the free spectral range $\nu_f = c/2l$.

When an optical cavity is resonant with the photons emitted by a transition in the energy state of an intra-cavity ion, these photons can either be re-absorbed by the ion or else leave the cavity through an absorption by the mirror coating or transmission through the mirror. The strength of the ion-cavity coupling is described by a parameter called the *cooperativity*,

$$C = \frac{g^2}{\kappa\gamma}. \quad (4.9)$$

Systems for which $C > 1$ are said to be in the strong coupling regime, while $C < 1$ is considered weak coupling (Law and Kimble, 1997). In the strong coupling regime, photons emitted by the ion into the cavity mode are more likely to be reflected by the mirrors until they are reabsorbed again by the ion. In the weak coupling regime, photons are more likely to leave the cavity through one of the loss or transmission channels rather than be reabsorbed. In order to enter the strong coupling regime, we need to increase the cavity coupling rate g relative to the decay rate κ and the spontaneous emission rate γ . Since $g \propto l^{-1/2}$ and $\kappa \propto l^{-1}$, the cooperativity is independent of the cavity length. The spontaneous emission rate for the $^{171}\text{Yb}^+$ ion is equal to $\gamma = 2\pi \times 19.6$ MHz. The parameters available for increasing C are therefore improving the reflectance of the mirrors to increase the finesse, \mathcal{F} , and decreasing the cavity mode size at the ion, which decreases the mode volume as $V \sim w_{ion}^2$. The optimal value of C depends on the particular application of the cavity QED system. We have investigated two important applications here: the efficient collection of entangled photons in Sec. 4.2 and ultra-fast qubit state detection in Sec. 4.3.

4.2 Improved Collection of Photons

One of the important goals for scaling quantum computers to larger sizes is to be able to distribute quantum information (QI) over a network of smaller quantum computing nodes, called elementary logic units (ELUs). QI is mediated over different ELUs using photons, which can travel over long distances through optical fibers while maintaining their quantum coherence with the ion. This allows, for example, teleportation of quantum states and quantum cryptography (Kimble, 2008). Photonic entanglement with ions has important implications for the scalability of a QI system since single ion chains in an ELU are limited to $N \approx 10 - 20$ qubits for QI purposes, and photonic links can connect several quantum nodes via a photonic quantum bus

(Monroe and Kim, 2013).

One way of achieving remote qubit entanglement which is well suited for trapped ion qubits is through the process of heralded entanglement (Moehring et al., 2007). In this scheme, remote entanglement of two ions can be achieved by subjecting two photons, one from each ion, to a Bell-state measurement where ion entanglement is heralded by the coincident detection of the photons on opposite detectors (Simon and Irvine, 2003). The two photon interference used in such a measurement is a purely quantum phenomenon in which two coincident photons impinging on a beam splitter simultaneously will either both be reflected, both transmitted, or have one transmitted and the other reflected. For two photons with the same polarization, frequency, and spatial mode, they will always emerge in the same direction due to their indistinguishable nature. While the generation of the entangled pair of ions is probabilistic in this scheme, once the coincident detection of the photons is made the entanglement is heralded with a high fidelity (i.e. $\geq 90\%$).

An important metric for the scalability of quantum networks is the entanglement generation time, which is the time it takes to generate an entangled pair of ions using a photonic interconnect link. The heralded entanglement process requires that each of the two photons be entangled with an ion, either through their frequency or polarization. Since this protocol requires the coincident detection of one photon from each ion, the entanglement rate of the ions scales as the square of the photon collection probability from each ion. In the case of Maunz et al. (2007), the entanglement rate was about 0.1 Hz from a photon collection probability of 1.4×10^{-8} . Entanglement rates as high as 4.5 Hz for $^{171}\text{Yb}^+$ ions have been achieved using a high numerical aperture (NA) lens of $NA = 0.6$, which allowed for the collection of $\sim 1.4\%$ of the emitted photons (Hucul et al., 2015). While progress is being made on increasing the entanglement generation rate by developing UV fiber beam splitters and near unity efficient photon detectors (Marsili et al., 2013), utilizing an integrated optical cavity

can allow for a factor of 5-6 times improvement in the collection rate over the best lens designs available today. When the probability is squared to find the coincident detection rate, this improvement can lead to an order of magnitude increase in the overall ion entanglement rate. This has important implications for trapped ion QI since the remote entanglement rate is one of bottleneck steps currently limiting the implementation of multi-ELU quantum computing. Our goal is to create a photonic interconnect between two ELUs with a speed near the time scale of the local Coulomb-based gates of the ion chain, which is around $100 \mu\text{s}$.

The generation of an entangled ion-photon pair begins with the initialization of the ion to an excited state and subsequent spontaneous emission, which produces a photon with a polarization that is entangled with the qubit state of the ion. By coupling the ion to a resonant cavity, we can get strong enhancement of the spontaneous emission into the cavity's resonant mode, which can have a clean Gaussian profile and be readily coupled into a single mode fiber. This enhancement is called the *Purcell effect*, named after the physicist E.M. Purcell who discovered this effect in the 1940s (Purcell, 1946). The principle concept is that the rate of spontaneous emission of an excited emitter is proportional to the density of photon states available in the surrounding space. If the emitter is surrounded by a cavity, the density of states is increased from the free space density to

$$\rho_{cav}(\omega) = \frac{\kappa}{\pi V} \frac{1}{\kappa^2 + (\omega_{cav} - \omega)^2}, \quad (4.10)$$

where V is the mode volume, ω_{cav} is the cavity resonance angular frequency and ω is the angular frequency of the atomic transition. Taking the ratio of this quantity to the free space density of states, $\rho_{free}(\omega) = \omega^2 V / \pi^2 c^3$, gives the Purcell factor

$$F_p = \frac{3Q\lambda^3}{4\pi^2 V}, \quad (4.11)$$

where Q is the cavity quality factor defined as $Q = \nu_0 / \delta\nu$ for a resonance frequency ν_0

and cavity linewidth $\delta\nu$. The Purcell factor is related to the cooperativity parameter of Eqn. 4.9 as $F_p = 2C$, and quantifies the enhancement of the spontaneous emission probability for an atom in a cavity relative to one in free space.

Our design for the cavity trap calls for a hemispherical cavity configuration, as shown in Fig. 4.1. The cavity geometry defines the mode volume, V , and having a sufficiently small mode volume is a critical condition to achieving a large Purcell enhancement in Eqn. 4.11. For an ion trapped at height z above the mirror surface, a Gaussian cavity mode with waist w_0 at a wavelength λ has a beam radius of $w_{ion} = w_0\sqrt{1 + (z\lambda/\pi w_0^2)^2}$ at the ion, where the electric field amplitude is scaled by a factor of $E \sim E_0 w_0 / w_{ion}$ relative to its amplitude E_0 at the waist. We define the scaled cavity mode volume of the Gaussian mode at the ion as $V_{ion} = \pi w_{ion}^2 l / 4$, where l is the length of the cavity. In this case, V_{ion} replaces the traditional mode volume V in Eqn. 4.8 for the coherent coupling rate.

We are interested in calculating the probability that a single photon leaks out of the cavity during a time interval $[0,t]$ without making a spontaneous atomic decay, written as $P_{extr}(t)$. For a sufficiently long detection time compared with the pulse width of a single photon, we have for the probability of having a photon emitted into the resonant cavity mode (Cui and Raymer, 2005; Law and Kimble, 1997)

$$P_{cavity} = \frac{2C}{2C + 1}. \quad (4.12)$$

The total emission probability of photons extracted from the cavity mode is then given by

$$P_{extr} = \left(\frac{\kappa}{\kappa + \gamma/2} \right) \left(\frac{2C}{2C + 1} \right). \quad (4.13)$$

The quality of the mirror coatings enters into two parts of this equation for P_{extr} . While a higher reflectivity of the mirrors will improve C by decreasing κ , it will also slow the extraction probability since the photons emitted into the cavity mode will

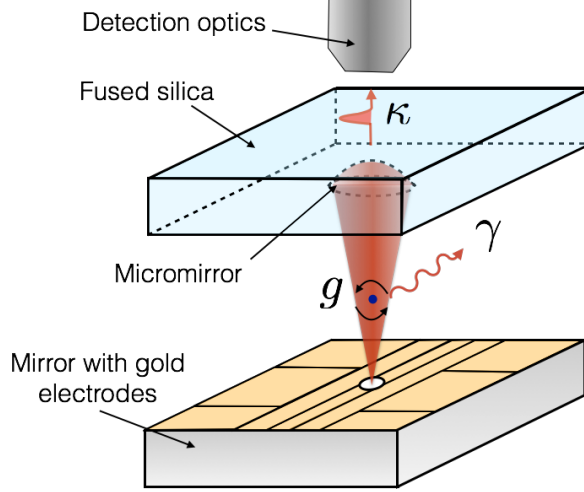


FIGURE 4.1: A schematic of the hemispherical cavity showing the ion trap and optical cavity arrangement. The ion trap is fabricated directly on the flat mirror while the curved mirror is positioned above a hole in the trap electrodes to form the cavity.

be less likely to transmit through the mirrors and out of the cavity. The balance between the two competing terms in Eqn. 4.13 means an optimal mirror reflectance can be found which maximizes P_{extr} for each cavity geometry.

The initial design for our cavity called for using small, super polished mirrors with a radius of curvature (RoC) of 5 mm, and bringing the cavity length to nearly the concentric limit of $R = l$, which according to Eqn. 4.1 is the limit beyond which the cavity cannot sustain a resonant Gaussian mode. In this limit, the mode size on the curved mirror will asymptotically increase as the waist on the flat mirror shrinks to zero. The expression for the beam radius on the curved mirror, w_1 , in terms of the cavity length and radius is

$$w_1 = \sqrt{\frac{\lambda l R}{\pi}} (l(R - l))^{-1/4}. \quad (4.14)$$

The waist on the flat mirror side of the cavity is

$$w_0 = \sqrt{\frac{\lambda l}{\pi}} \left(\frac{R}{l} - 1 \right)^{1/4}. \quad (4.15)$$

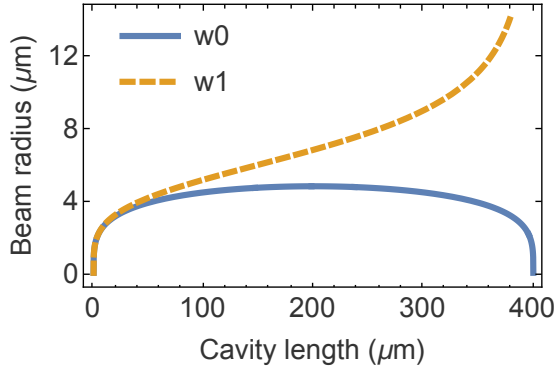


FIGURE 4.2: The beam size on the flat mirror w_0 and on the curved mirror w_1 as a function of cavity length for a $R = 365 \mu\text{m}$ cavity.

Since the mode volume is proportional to the length of the cavity, a smaller RoC mirror will allow for a smaller volumes when $l \leq R$. The smallest RoC mirror attainable with traditional super polishing techniques we found was around 5 mm. Fig. 4.3a shows the relevant cavity QED dynamical rates as a function of cavity length for a cavity system with a $R=5$ mm mirror and a $^{171}\text{Yb}^+$ ion, while Fig. 4.3b shows the photon emission probability P_{extr} of Eqn. 4.13 as a function of cavity length for this system. The actual probability to collect the emitted photon into a single mode fiber also depends on the fiber coupling rate, ϵ , and the fraction of the light which is transmitted through the curved mirror, $\epsilon_t = T_2/(T + L)$.

For reasonable fiber coupling efficiencies of $\sim 90\%$ and typical cavity loss and transmission factors in the ultra-violet (UV) coatings, the benefit of the cavity over high NA refractive optics, which can achieve a best case collection probability of 10%, only occurs for cavity lengths within around $5\text{-}15 \mu\text{m}$ of the instability point. This turned out to be a major drawback of this design because aligning a cavity close to concentricity is extremely difficult, as detailed further in Sec. 5.2. For this reason, we have also designed an optical cavity setup which avoids the super polished limit on the RoC by investigating the use of micromirror cavities made through the laser

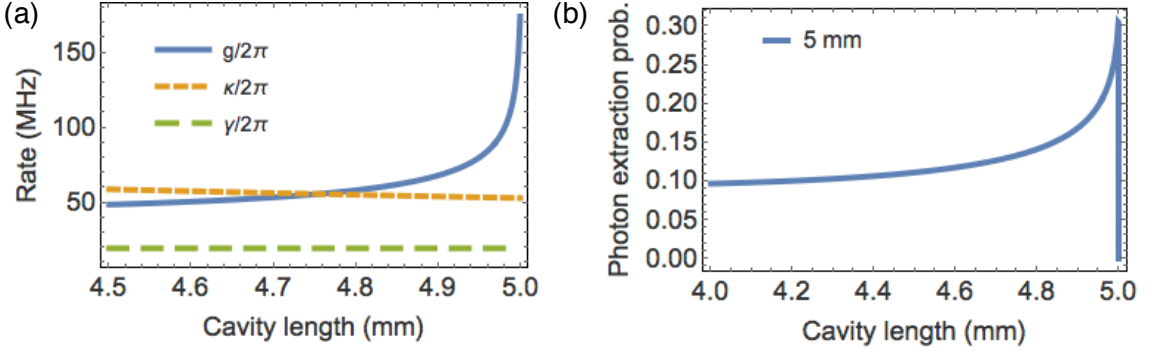


FIGURE 4.3: (a) Simulation of the cavity QED rates $(g, \kappa, \gamma)/2\pi$ as a function of the cavity length in the near concentric limit of a cavity with a $R= 5$ mm mirror. (b) Calculation of the cavity emission rate P_{extr} as a function of cavity length.

ablation of fused silica surfaces. Such a process has been shown to produce high finesse mirrors at infrared (IR) wavelengths when made on the cladding of optical fibers (Hunger et al., 2010). However, there are currently no demonstrations of using these fiber mirrors at UV wavelengths. The small RoC cavities made with these micromirrors have a number of significant advantages over the larger, millimeter sized ones. First of all, they are relatively inexpensive to make and can be made in large batches on high quality fused silica substrates. Secondly, their size can be easily varied by varying the shape, power, and exposure time of the ablation pulse. Lastly, and most importantly, the performance range for efficiently extracting single photons into a fiber scales very well over a broad range of cavity lengths, rather than just very close to the concentric limit as with the larger mirror cavities. The main reason behind this improvement with shorter cavities is the increase in the free spectral range, which scales as inversely proportional to the cavity length. Indeed, the cavity cooperativity of Eqn. 4.9 is independent of length and the first factor in Eqn. 4.13 is also approximately independent of length since the spontaneous emission rate is an order of magnitude less than the cavity loss rate κ for these micromirror cavities. This means the total P_{extr} probability should also be approximately independent

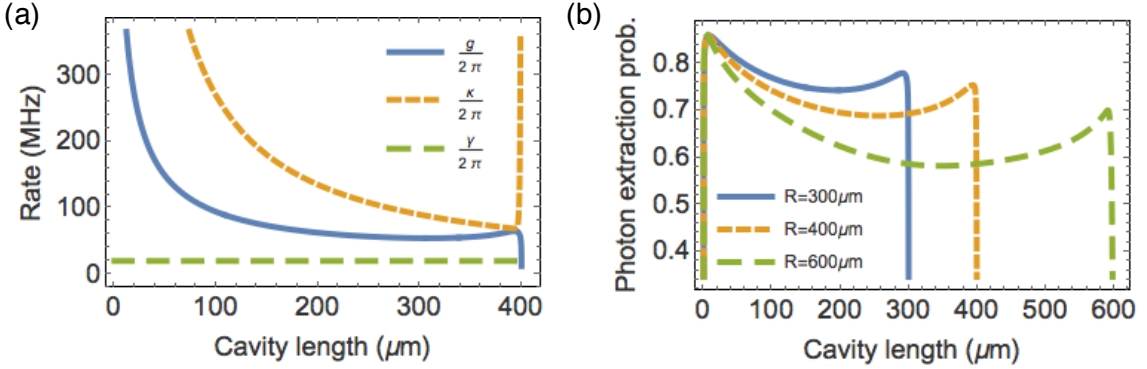


FIGURE 4.4: (a) Simulation of the cavity QED dynamical rates of $(g, \kappa, \gamma)/2\pi$ for a $400 \mu\text{m}$ cavity. (b) Calculation of the quantity P_{extr} for cavities with a RoC of $R = 300, 400$, and $600 \mu\text{m}$ as a function of cavity length. These results show a much wider range of lengths over which a high P_{extr} can be achieved compared with Fig. 4.3.

of length. The relevant rates of $(g, \kappa, \gamma)/2\pi$ for a cavity with radius of curvature $R = 400 \mu\text{m}$ are shown in Fig. 4.4a. The resulting quantity of interest, P_{cavity} , is shown in Fig. 4.4b for $R = 400 \mu\text{m}$ as well as for $R = 300 \mu\text{m}$ and $R = 600 \mu\text{m}$. Important assumptions made for these simulations include (1) an $^{171}\text{Yb}^+$ ion positioned at the antinode of cavity with a height of $50 \mu\text{m}$ centered above the beam waist at the trap surface, (2) a cavity finesse of $\mathcal{F} \approx 1200$ with a combined bad losses (i.e. losses from absorption or scattering) of $L=500$ ppm at 369.5 nm wavelength, and (3) a spherically symmetric curved mirror with a diameter of $90 \mu\text{m}$. Comparison with the simulation results of the $R=5 \text{ mm}$ cavity shown in Fig. 4.3 indicates not only a clear improvement in the overall photon extraction probability P_{extr} , but also a much wider range of cavity lengths over which these relatively high extraction probabilities can be reached. The cooperativity of such a cavity with $R = 400 \mu\text{m}$ and $l = 300 \mu\text{m}$ is $C \approx 3.3$, which put this cavity QED system into what is normally considered the strong coupling regime of $C > 1$.

One of the design space tradeoffs with the micromirrors is that with the smaller

RoC also comes a smaller mirror aperture. As the cavity length approaches the concentric limit, the size of the mode on the curved mirror increases asymptotically, as calculated in Eqn. 4.14 and plotted in Fig. 4.2. For a finite diameter mirror, some of the beam intensity will then lie outside the mirror aperture and thus not reflect back into the cavity. We can include this effect in our model by introducing an appropriate aperture to the mirror and considering the added round trip clipping loss to be all the energy which lies outside this aperture. From this rather simplified model, we can estimate the losses from an aperture of radius a to be

$$\mathcal{L}_{clip} = e^{-2a^2/w_1^2}, \quad (4.16)$$

where w_1 is the Gaussian mode radius on the curved mirror as shown in Fig. 4.2 (Hunger et al., 2010). Our simulation results indicate that for the relevant parameter regime with $R \approx 400 \mu\text{m}$ and $l \approx 300 \mu\text{m}$, the usable diameter of the laser ablated mirror should be at least $50 \mu\text{m}$ to avoid significant clipping losses. This simplified model tends to overestimate the clipping loss effects of the aperture because it does not take into account how the aperture modifies the beam size on the mirrors from the ideal solution with no aperture. In Sec. 5.6, I show a method for accurately simulating the shape of the cavity mode, and derive a better estimate for the clipping losses in micromirror cavities.

The quantity of interest calculated thus far has been P_{extr} , which is the probability that a single photon emitted from an ion is coupled to the resonant TEM₀₀ cavity mode and is then transmitted out of the cavity rather than lost in the mirror coatings or through spontaneous emission into the emitter reservoir. Ultimately, we are interested in the probability of coupling photons emitted from the ion into a single mode fiber for use in a heralded entanglement scheme. The protocol for ¹⁷¹Yb⁺ excitation and entanglement with an emitted photon polarization involves state initialization into the $|0\rangle$ qubit state, a microwave rotation to the $|1\rangle$ state, and subsequent exci-

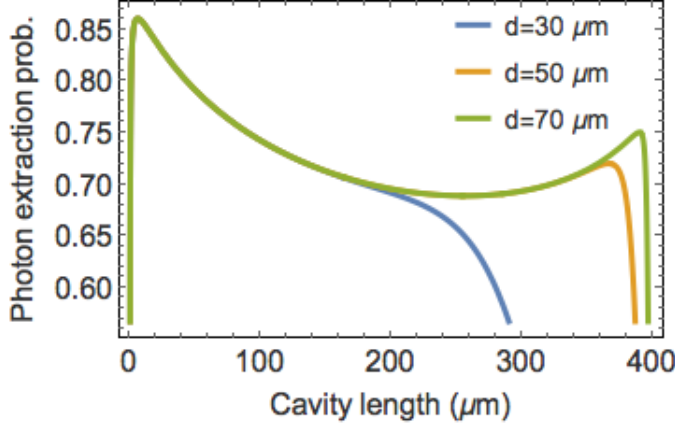


FIGURE 4.5: An increase in clipping losses limits the overall P_{extr} factor as the size of the cavity is increased. Shown here is P_{extr} as a function of the cavity length with $R = 400 \mu\text{m}$ for various diameters of the curved micromirrors and clipping losses calculated as in Eqn. 4.16.

tation to the $^2P_{1/2}$ level followed by spontaneous decay back to the $^2S_{1/2}$ level. This entire process can occur at a repetition rate of roughly $r_{rep} = 500 \text{ kHz}$ (Hucul et al., 2015). The fraction of these photons which can be collected into a single mode fiber depends on the transmission fraction through the output mirror, $\epsilon_t = T_{out}/\mathcal{L}$, and the fiber coupling rate, ϵ_f , which we expect to have a reasonable value of approximately 80%. Combining all three quantities with P_{extr} and the 2/3 efficiency that the ion decays to one of the $^2S_{1/2}|1, \pm 1\rangle$ states gives the final expression for the fiber coupling rate as

$$r_{fiber} = \frac{2}{3}\epsilon_t\epsilon_f r_{rep} P_{extr}. \quad (4.17)$$

The cavity design we are proposing can therefore allow for an optimal fiber coupling rate of entangled photons of up to 200 kHz, which is an order of magnitude greater than what would be theoretically possible with current technologies. A summary of the key parameters from our simulations is shown in Table 4.1.

Table 4.1: A summary of the relevant cavity parameters for our microcavity design.

| Parameter | Symbol | Value |
|-------------------------|----------------------------|------------------------------|
| Cavity length | l | $300 \mu\text{m}$ |
| Rad. of curvature | R | $400 \mu\text{m}$ |
| Mode radius | w_{ion} | $4.7 \mu\text{m}$ |
| Cavity rates | $(g, \kappa, \gamma)/2\pi$ | $(54, 90, 19.6) \text{ MHz}$ |
| Cooperativity | C | 3.3 |
| Finesse | \mathcal{F} | 1200 |
| Photon extraction prob. | P_{extr} | 0.7 |
| Collection rate | r_{fiber} | 200 kHz |

4.3 High Fidelity, Ultra-Fast State Readout

A second important application we have investigated of a cavity QED system for trapped ion quantum computing is in the area of quantum state detection. For trapped ion qubits such as $^{171}\text{Yb}^+$, qubit state detection in current practice is done by applying light resonant with the $|2S_{1/2}, F = 1\rangle \leftrightarrow |2P_{1/2}, F = 0\rangle$ electronic transition which excites electrons in the $|1\rangle$ qubit state to the $2P_{1/2}$ manifold (See Fig. 2.1). The subsequent spontaneous emission as the electron decays from this state will emit a photon in a random direction, which can be collected into a detector. For ions in the $|0\rangle$ qubit state of $|2S_{1/2}, F = 0\rangle$, this transition is detuned by 14.7 GHz and will therefore be excited only off resonantly and at a much lower rate. Applying resonant 370 nm light for a detection time of 30-100 μs and looking for the presence of any spontaneously emitted photons allows one to determine whether the quantum state was $|0\rangle$ or $|1\rangle$ with a fidelity which depends primarily on the light collection efficiency, the quality of the detector, and the detection time interval. State detection fidelities as high as 99.915% for a 100 μs detection time have been measured in $^{171}\text{Yb}^+$ systems using a high numerical aperture lens to collect the ion fluorescence into a PMT (Noek et al., 2013a).

The possibility exists for significant improvement in both the time and fidelity

of qubit state detection compared with the highest achieved values using standard refractive optics approaches when using an optical cavity to measure the ion state. In the cavity scheme, the qubit state of $|1\rangle$ is distinguished by its strong coupling to the resonant cavity mode. For example, if the ion is in the $|0\rangle$ state, then its atomic resonance frequency will be approximately 12.6 GHz detuned from the cavity's resonance frequency, and therefore will not couple to the cavity mode, which has a linewidth of around 400 MHz. When the ion is in the $|1\rangle$ state, however, it will nominally be resonant with the cavity and the combined ion-cavity system will have a resonant frequency which is split into two peaks from the bare cavity resonance. This frequency shift can be detected from a change in the cavity transmission of a probe beam and used as a sensitive and fast state detection mechanism. Basing our analysis primarily on the model described in Horak et al. (2003), the stationary solution for the intracavity photon number of a cavity coupled to a resonant two level emitter (TLE) is given by $N = |\alpha|^2$, where

$$\alpha = \frac{\eta}{(\kappa + \beta) - i(\Delta_c - U)}, \quad (4.18)$$

and the population of the excited state of the TLE is given by

$$\rho_{11} = \frac{g^2 N}{\Delta_a^2 + \gamma^2 + 2g^2 N}. \quad (4.19)$$

Here Δ_a and Δ_c are the detunings of the laser from the atomic resonance and the cavity resonance, respectively, and

$$\beta = \frac{g^2 \gamma}{\Delta_a^2 + \gamma^2 + 2g^2 N} \quad (4.20)$$

and

$$U = \frac{g^2 \Delta_a}{\Delta_a^2 + \gamma^2 + 2g^2 N}. \quad (4.21)$$

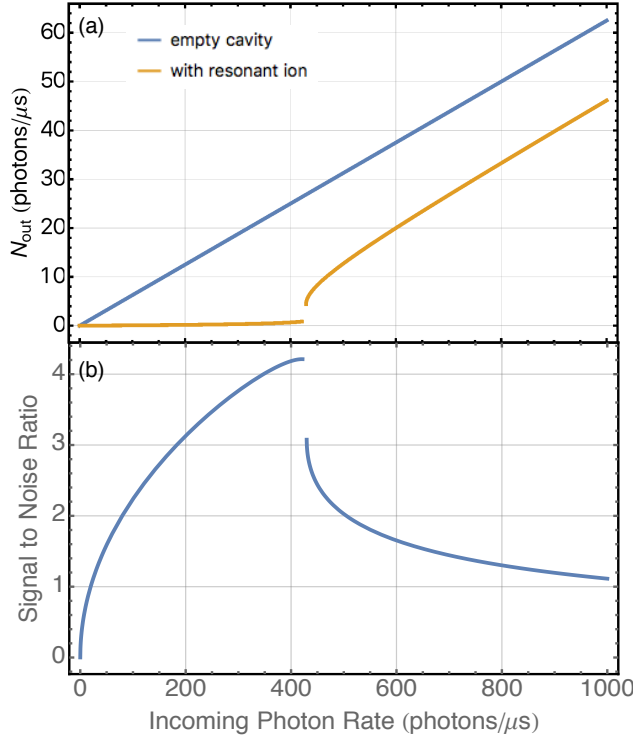


FIGURE 4.6: (a) The calculated shift in the output photon rate from the cavity between an ion in the bright state $|1\rangle$ (on resonance) and the dark state $|0\rangle$ (off resonance) for a hemispherical cavity with $R = 360 \mu\text{m}$ and length $l = 300 \mu\text{m}$ (neglecting clipping losses). (b) The SNR for the state detection signal in (a) as a function of the incoming photon rate for a detection time of $1 \mu\text{s}$.

The state of the ion as $|0\rangle$ or $|1\rangle$ is detected through its effect on the field amplitude α . In Fig. 4.6, I have plotted the difference in the output photon rate of the cavity vs. the input photon rate for a $R = 360 \mu\text{m}$ cavity of length $300 \mu\text{m}$. In this case, the optimal SNR of the system occurs at an input photon rate of roughly 400 photons/ μs , which corresponds to a power of around 0.25 nW.

An important parameter for optimizing the sensitivity of this state detection measurement scheme is calculating the signal to noise ratio (SNR). A good measure of the SNR for this system can be written in terms of the output photon rate $n_{out} = N\kappa T_2$ and detection time τ as a function of the qubit state of the ion in the cavity

with the following equation

$$SNR = \frac{n_{out}(|0\rangle)\tau - n_{out}(|1\rangle)\tau}{\sqrt{n_{out}(|0\rangle)\tau} + \sqrt{n_{out}(|1\rangle)\tau}}. \quad (4.22)$$

The result using our cavity parameters is shown in Fig. 4.6b, and indicates that a SNR of roughly 4 is possible with only a $1 \mu s$ detection time, which is two orders of magnitude less than the time currently needed for state detection using conventional refractive optics. This analysis therefore shows a pathway towards significant improvement in qubit state detection, which is an important operation in quantum computation with trapped ions.

4.4 Summary of the Cavity Design

In this chapter, I have outlined two applications of a cavity QED system for trapped ion quantum computation which can provide order of magnitude improvements in several critical areas, including enhanced remote qubit connectivity and faster state readout. Our cavity design utilizes small mode volume micromirror cavities with RoC's of several hundred microns to create a strong coupling between an ion and the cavity in a way which can be readily integrated with the mirror trap described in Chapter 2. The merit of our design for these applications is demonstrated here using a theoretical analysis supported by simulations to calculate important performance metrics. In Chapter 5, I detail progress towards realizing these small mode volume cavities for eventual use as part of a trapped ion cavity QED system.

5

Cavity Testing and Characterization

5.1 Introduction

Integrating a surface ion trap with an optical cavity has been a long standing goal in the field of ion trapping (Herskind et al., 2011; Noek et al., 2013b). One of the unique difficulties of using a surface trap for cavity QED experiments lies in finding a good way to integrate the cavity mirrors with a surface trap. Until now, most ion trap experiments involving cavities have been performed using macroscopic three dimensional ion traps where the cavity can fit inside the trap electrodes, and most use infrared laser frequencies (Kreuter et al., 2004; Steiner et al., 2013). Initial proposals for designing such a system with a surface trap sought to integrate a single mode fiber for light collection directly with the ion trap by fabricating the surface trap on the fiber cladding (Kim et al., 2011a). A related idea to integrate a fiber with a surface trap involved drilling a small hole in the trap surface and gluing a fiber underneath the trap, rather than fabricating the trap on the fiber directly (VanDevender et al., 2010). While the gluing experiment showed some promise, the plan to fabricate directly on the fiber tip suffered from many technical difficulties arising from trying

to use a photolithography process on a fiber tip, as well as difficulties with polishing the fiber. One potential work around could be to build a cavity enclosing the entire surface trap, but this requires the cavity mirrors to be separated by enough distance to fit the surface trap (i.e. ~ 10 mm), which prevents the use of the small mode volume cavities useful for efficient photon collection (Cetina et al., 2013). We have pursued a different path towards realizing a surface trap cavity which takes the unique approach of separating the cavity and fiber coupling aspects of the experiment while retaining the advantages of an integrated cavity trap by fabricating the trap directly on a flat, highly reflective mirror. This chapter details the fabrication and testing of micromirror cavities for their eventual use with the mirror trap towards building a fully integrated ion trap and cavity system. Many of the performance requirements of the cavity were detailed in Chapter 4 as I considered two primary applications for which the cavity could be used, including efficient collection of single photons emitted by an intra-cavity ion and high fidelity, fast qubit state detection. The initial testing of the macroscopic, millimeter sized cavities and their limitations is explained in Sec. 5.2. The fabrication and characterization of the micromirror cavities we developed as a response to those limitations is described in Secs. 5.3- 5.6. Finally, the performance and outlook of these cavities is described in Secs. 5.7- 5.10.

5.2 Super-Polished Mirror Measurements and Initial System Design

The first set of experiments I performed with the cavity involved characterizing the dielectric coatings of the mirrors to measure their transmission, reflectance, losses, and finesse at the design wavelength of 370 nm. The initial cavity design, as outlined in Sec. 4.2, called for using super polished mirrors with the minimum radius of curvature we could obtain, which was around 5 mm. These mirrors were coated with a dielectric coating that was highly reflective for both 370 nm and 780 nm light. The purpose of the 780 nm coating was to allow for a reference laser to be used

for stabilizing the cavity length without interacting with the ion. The substrates tested were 7 mm in diameter and 4 mm thick. They were coated by the vendor Advanced Thin Films with a process that involved ion beam assisted sputtering with active monitoring followed by annealing in air to further reduce absorption. This process had to be highly optimized to prevent scattering and absorption of light by the mirror coating. The most important aspects of these mirrors are the surface roughness, the coating density, and the coating chemistry. We used super-polished substrates with a RMS roughness of $<0.5 \text{ \AA}$ to minimize light scattering. According to the specification data sheets received from ATFilms, these mirrors were measured to have a transmission of $<0.1\%$ and a reflectance of $>99.97\%$ at a wavelength of 370 nm, and a transmission of $<0.05\%$ and reflectance of $>99.99\%$ at 780 nm wavelength.

To measure the reflectance, transmission and losses of these mirrors to confirm the coating specifications, I built a test cavity out of a flat mirror and a 5 mm RoC mirror. The flat mirror was held by a fixed post, while the curved mirror was placed in an optical mirror mount with three tuning knobs for changing the tilt of the curved mirror with respect to the flat mirror. A piezo electric transducer was placed in between one of the spring-loaded tuning knobs and the mirror holder part of the mount. Varying the voltage applied to the piezo over a range of 0-60 V allowed for scanning the cavity length over several half wavelengths of 370 nm light, and hence several cavity free spectral ranges. One way of measuring the mirror coating losses (i.e. light incident on the mirror which is not reflected or transmitted) is to measure both the reflected power, P_r , and the transmitted power, P_t , for a resonant cavity as a function of the incident power, P_{in} . From these measurements, along with an independent measurement of the finesse from the cavity free spectral range and linewidth as $\mathcal{F} = \nu_f/\delta\nu$, I was able to use the equations from Hood et al. (2001) to extract the cavity mode matching factor ϵ and the losses on each mirror, L_1 and

L_2 . The relevant equations from this reference are repeated here for clarity:

$$\mathcal{F} = \frac{2\pi}{T + L}, \quad (5.1)$$

$$\frac{P_t}{\epsilon P_{in}} = 4T_1 T_2 \left(\frac{\mathcal{F}}{2\pi} \right)^2, \quad (5.2)$$

and

$$\frac{P_r - (1 - \epsilon)P_{in}}{\epsilon P_{in}} = (L_1 + L_2 + T_1 - T_2)^2 \left(\frac{\mathcal{F}}{2\pi} \right)^2. \quad (5.3)$$

All coating characterization was done with 370 nm light as this was the wavelength critical to our design space. I used a free space electro-optic modulator (EOM) to modulate the laser light at 20 MHz to provide a reference with which to measure the linewidth of the cavity. The linewidth was measured to be $\delta\nu = 5.13 \text{ MHz} \pm 0.8 \text{ MHz}$. For measuring the length of the cavity, I used 780 nm laser light for which we had a fiber EOM from the vendor EO Space that could modulate the laser light phase up to 20 GHz. By modulating the input 780 nm light at around 16 GHz, I was able to overlap the sidebands from neighboring transmission peaks separated by a free spectral range. From this measurement, the cavity free spectral range could be found as twice the modulation frequency of the EOM, which was around 32 GHz. This corresponded to a cavity length of 4.7 mm, which was around 300 μm away from the instability point of the cavity, where the length equals the RoC (for a hemispherical cavity). The results of these measurements applied to Eqns. 5.1-5.3 were the following: a flat mirror transmission of $T_1 = 340 \text{ ppm}$ and loss $L_1 = 220 \text{ ppm}$, a curved mirror transmission of $T_2 = 420 \text{ ppm}$ and loss $L_2 = 240 \text{ ppm}$, with an overall cavity finesse of $\mathcal{F} = 4800 \pm 1200$. These measurements helped confirm the suitability of the UV mirror coatings we received for use with the cavity experiment.

One of the main difficulties with the millimeter sized cavities is that in order to get to a parameter regime where the ion's fluorescence enhancement from the

cavity allows for a significant increase in the photon collection rate, the cavity must be within several microns of the instability point in the near concentric limit (see Fig. 4.3). This places a very stringent requirement on cavity alignment because near instability where $g_1 = 1 - l/R \approx 0$, the size of the beam on the curved mirror becomes very large and any small defects or misalignment of the mirror will prevent a stable mode from forming in the cavity. One of the mirror alignment challenges presented by this design was that the cavity had to be initially aligned at a length of at least 1 mm shorter than the RoC just to obtain an initial transmission signal. As the mirror separation was slowly increased, the transmission signal was gradually lost before the necessary length was reached, even as the mirror tilt and alignment were adjusted to maximize transmission. A fundamental difficulty of such an alignment procedure was that it simultaneously required the capability of a long scan range for the cavity length of over several millimeters, while at the same time allowing for a small step size ($\sim 1-2 \mu\text{m}$) for alignment in a range of 10-50 μm away from the instability. As a result of these findings, we changed our design towards a new approach based on laser ablated microcavities, which turn out to not only be easier to align, but also have better cavity QED performance for the applications we explored in Chapter 4.

5.3 Micromirror Laser Ablation

In recent years, several research groups have created small mode volume cavities via laser ablation of optical fibers to form the mirrors of a cavity (Colombe et al., 2007; Hunger et al., 2010; Petrak et al., 2011). This technique allows for achieving an order of magnitude smaller radii of curvature for the cavity mirrors when compared with traditional super polishing techniques. Since the RoC of a Gaussian beam scales with the Rayleigh length as $R(z) = z(1 + (z_R/z)^2)$, a smaller radius allows for a smaller beam waist, and hence a smaller mode volume.

With the goal of creating our own micromirrors, we use a high power CO₂ laser

with a wavelength of $10.6 \mu\text{m}$ for the laser ablation of dielectric surfaces. This technique provides significant advantages over conventional etching or polishing methods due to its ability to create smooth, curved surfaces from a reflow of melted dielectric materials. Although these microcavities can be used with relatively small mirror spacings, for our applications, they must still allow sufficient space between the two mirrors to stably trap an ion. The minimum spacing needed for trapping depends on several factors, including that the lasers do not clip on any of the mirror surfaces and that the ion is not too close to potential static charges in the mirror dielectric coatings. Stray charges in the coatings will affect the ion with a strength that scales as the inverse square of their separation, so a close proximity to the ion can potentially degrade the trap stability. Based on the numerical aperture of the lasers interacting with the ion and our estimates of the mirror charging effects, we have determined that a minimum cavity length of around $250\text{-}300 \mu\text{m}$ is required for ion trapping purposes.

One of the significant differences in our setup compared to other work done in this field is that we have formed our microcavities using flat fused silica substrates rather than optical fibers. While the primary motivation for using optical fibers to form the cavity is that they simplify the coupling of light to the cavity, we believe that our approach offers performance benefits which outweigh the cost of the external fiber coupling optics. Specifically, the fiber cavity approach has two significant drawbacks for our system requirements, especially for use with UV wavelengths and with a surface trap. Firstly, as mentioned previously in Sec. 5.2, integrating an optical fiber directly with a surface trap is extremely challenging from a fabrication process point of view. Placing an optical fiber below a hole in the surface trap, as in VanDevender et al. (2010), requires extreme precision when drilling a hole in the surface trap and epoxying the fiber under the hole, making fabrication difficult and the system very fragile. Secondly, at the UV wavelength of 370 nm for which we are designing our

cavity, the core diameter of a single mode (SM) fiber is around $3\ \mu\text{m}$. From the calculation results shown in Fig. 4.2, we expect the beam size on the curved mirror to be in the range of $8\text{-}14\ \mu\text{m}$ for the cavity dimensions we are interested in. The size difference between the cavity mode and the fiber core will cause a significant drop in fiber coupling efficiency. We expect to have a factor of 3-4 times improvement in our fiber coupling efficiency from the cavity mode by separating the fiber from the cavity mirror. Results from our fiber coupling testing are shown in Sec. 5.10.

Our approach to constructing the microcavities uses a polished rectangular wafer of 0.5 mm thick fused silica as the substrate for the laser ablation process. This approach allowed for multiple ablation spots to be put on each sample. Since the ablation procedure has a yield rate of usable mirrors with our current process of only around 30-40%, having multiple spots on each substrate increases the likelihood of having at least one high quality mirror on each sample. Careful control of the power, beam shape, and exposure time is required to hit the correct parameter regime where the ablation spots are suitable for use as cavity mirrors. In this regime, thermal evaporation occurs and melting of the fused silica is restricted to a thin surface region above the ablation spot. This prevents surface tension from contracting the surface into a convex shape. The Synrad CO₂ laser we used has a maximum power output of 10 W. It operates by using the vibrational excitation of CO₂ molecules inside the laser to create a high power laser pulse. We continually feed it a tickle pulse to maintain the population inversion, then send several 50 ms electrical pulses to fire the laser and send high power (several watts) light pulses to the substrate. Since the ablation spot forms as a direct result of the optical power delivered to the substrate from these pulses, the shape of the spot will closely match the shape of the intensity distribution of the laser light. In order to get spherically symmetric spots, we had to spatially filter the CO₂ laser pulse to make it as close to a symmetric Gaussian beam as possible. The filter setup utilized a telescoping set of plano-convex ZnSe lenses

with a circular pinhole midway between the lenses in the Fourier plane. From the Fourier transform properties of the focusing lens, higher frequency components of the light are spatially separated away from the central axis of the lens in the Fourier plane. We used a 100 μm pinhole at the Fourier plane with a 15 mm focal length lens to filter out the higher order spatial frequencies in the beam shape, which may cause asymmetries and aberrations in the ablation spots. After the pinhole and telescope, we used a final lens of focal length 200 mm to focus the spots down on the polished fused silica substrate. A microscope image of several of the ablations spots is shown in Fig. 5.1.

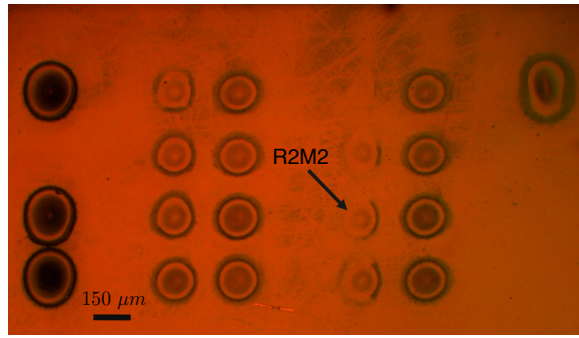


FIGURE 5.1: A microscope image of one of the substrates containing ablation spots. This sample contains 20 ablation spots for creating micromirrors and three larger spots to serve as alignment markers. The spot labelled R2M2 was the mirror primarily used for the cavity characterization results presented in this thesis. The larger, darker spots were also tested, but had a high level of surface roughness, which caused increased losses and finesse degradation when used as part of an optical cavity. The surface roughness around the edge of each mirror is characteristic of these ablation spots as some of the fused silica that was sputtered away during ablation redeposited on the surface.

After the laser ablation step, we used a Zygo NewView 5000 optical profilometer to characterize the shape of the ablation spots. This tool utilizes white light interferometry to produce a 3D topographical map of the sample surface. With this Zygo profilometer, we quantified the surface roughness, curvature, critical dimensions, and other topographical features of our ablation spots. The effective diameter of these

spots was estimated both by fitting them to a spherical function and determining the point at which the height profile deviated substantially from the fit, and from the standard deviation of a Gaussian fit function. The radius of curvature was found from the height measurements in the x-y plane along each principal axis, $z(x_i)$, using the equation

$$R(x_i) = \frac{(1 + z'(x_i)^2)^{3/2}}{z''(x_i)}. \quad (5.4)$$

The depth of the ablation spot, z_t , is related to the aperture radius a and the RoC as

$$z_t \approx \frac{a^2}{2R}. \quad (5.5)$$

Measurements for one particular mirror which we tested in the cavity setup, labelled as R2M2, are shown in Fig. 5.2.

While the Zygo optical profilometer is capable of measuring profile heights ranging from sub-nm up to 15 mm, one of its limitations for our use was the coarse lateral resolution of the scans, which had a step size of around $0.5 \mu\text{m}$. This prevented the measurements from capturing some of the high frequency roughness of the ablation spots, especially in the center of the mirror. For more accurate measurements of the surface roughness, we used an Atomic Force Microscope (AFM) to measure the surface profile with much better resolution. Many of the spots that appeared to be smooth on the Zygo turned out to have a high degree of surface roughness on the length scale of 10 -100 nm, which is comparable to the wavelength of light used in the cavity, and therefore potentially problematic. Among the mirrors made in the second ablation run and shown in Fig. 5.1, most of the mirrors with a large depth and radius contained this high frequency surface roughness, which significantly increased their bad losses. Future work on this project is being carried out to fine tune the ablation parameters of time and power and to prevent the redeposition of particulates during

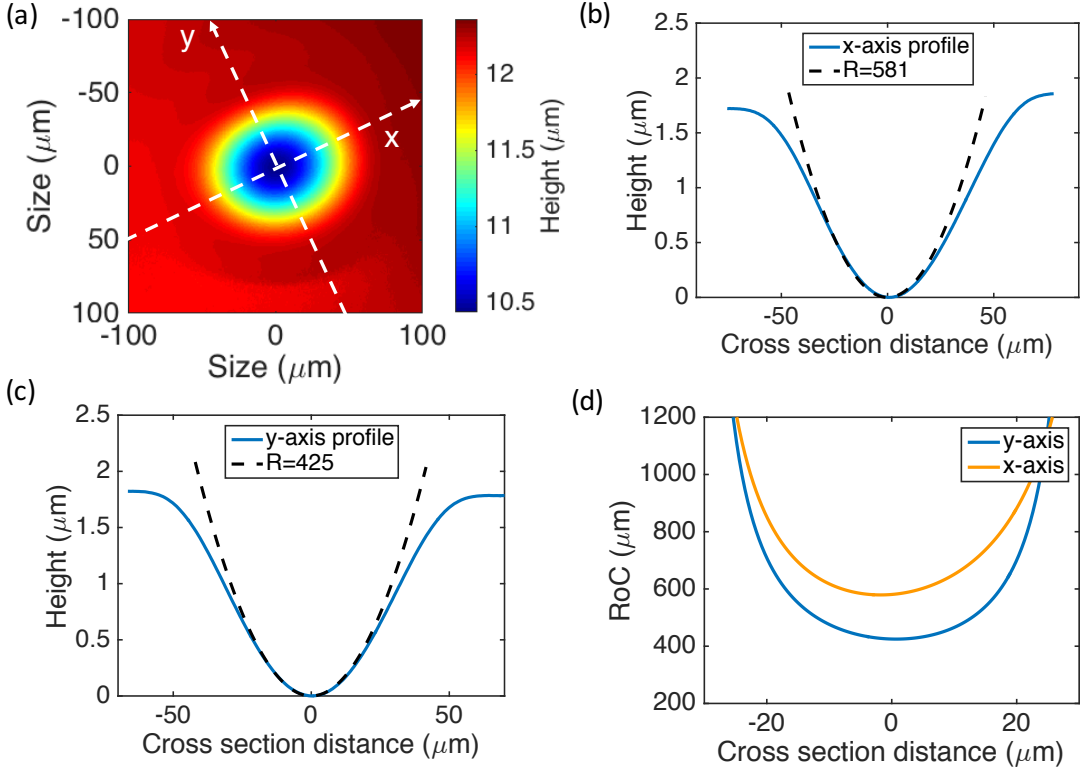


FIGURE 5.2: (a) The 2D mirror profile of the ablation spot R2M2 obtained with the Zygo profilometer. (b) The x-axis profile and (c) the y-axis profile, each with a circular fit to the data. The approximate diameter for these profiles found as the standard deviation of a Gaussian fit function is $\sigma_y = 44.2 \mu\text{m}$ and $\sigma_x = 50.3 \mu\text{m}$. (d) The radius of curvature in the x and y directions as a function of the cross sectional distance.

ablation to reduce the formation of this high frequency surface roughness.

We made two separate batches of ablation spots for testing in an actual cavity. Both were coated by the vendor Paradigm Research Optics with a high reflection coating for 780 nm wavelength. This coating was specified to have a reflectance percentage of $> 99.8\%$, and a transmission of close to 0.1% at this wavelength. The back side of the samples was coated with an anti-reflection (AR) coating, also for 780 nm light. The results of our testing these mirrors is described in the following sections.

5.4 Cavity Optomechanical Design

Our optomechanical design for the cavity had to take into account all the different requirements of making a stable cavity resonator suitable for integration with a surface ion trap. Some of the key constraints in making this design were allowing for a sufficient scan range along all three axes of motion for aligning a specific micromirror above the hole in the mirror trap electrodes, providing enough stability to dampen vibrations of the mirrors, ensuring all components are UHV compatible, and making the entire system small enough to fit inside the vacuum chamber octagon. The 0.5 mm thick substrates containing the coated ablation mirrors were diced into 5 mm x 5 mm squares. Each patch contained roughly 20 mirrors. The mirror substrate was epoxied to a ceramic piezo electric transducer, PD080.31 from the vendor PI (Piezo Technology). This was a PICMA miniature piezo actuator with a 2 μm travel range, an outer diameter of 8 mm, an inner diameter of 4.5 mm, and a 2.45 mm thickness. The epoxy used was the UHV compatible 353ND from the vendor Epo-tech. Once the mirror substrate was epoxied to the piezo, the piezo was then epoxied to the mirror mount. The entire mount, mirror, and piezo was an interchangeable part in the design. Each mirror patch tested was epoxied to its own piezo and mirror mount, which could then be placed into the rest of the optomechanical assembly system for testing each patch individually. The mirror mount was secured to the holder with a mounting screw and a set screw. A computer aided design (CAD) rendering of the entire optomechanical setup is shown in Fig. 5.3.

For mirror translation in the transverse directions, I used a combination of two compact positioners from the vendor SmarAct with part number SL-06. These positioners have a minimum step width of 50 nm and a full range of travel of ± 2.25 mm. They work on the principal of slip-stick motion, where a saw tooth voltage is applied to initially accelerate the actuator quickly when the inertial force becomes higher

than the frictional force. As the actuator slides, the applied force decreases until it is less than the frictional force again and the actuator comes to a stop. For translation along the cavity axis, which is the more critical direction, I use a SLC-1720 model positioner. This has a larger travel range of ± 6 mm and a smaller minimum step width of around 10 nm. In addition to the stepwise motion, this actuator can also be deflected by the piezo for achieving sub nm resolution over about a 1 μm scan range. This stage is mounted vertically to the baseplate as shown in Fig. 5.3. The base plate for mounting the cavity structure is made of titanium and contains threaded holes for screwing in the CPGA containing the trap.

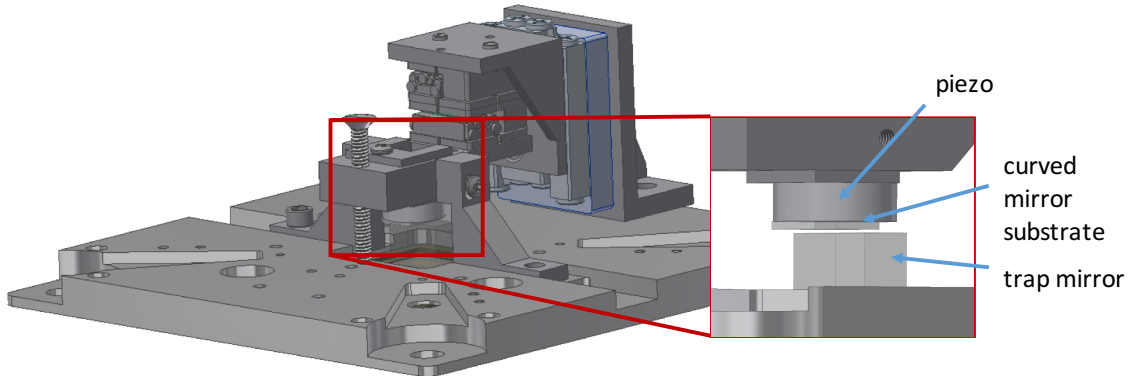


FIGURE 5.3: A computer rendering of the optomechanical setup for the cavity assembly.

In addition to having sufficient scan range and resolution, the cavity must also be stable from both a slow drift in the mirror separation and a mechanical vibrations point of view. The slower timescale drift can be due to temperature fluctuations or mechanical tension release, for example. The vibrations are primarily due to acoustic vibrations in the air exciting mechanical resonances of the cavity mounting structure. To understand the frequency spectrum of the vibrations, I measured the transmission of the unlocked cavity as it vibrated around the resonance point and calculated the power spectral density of the transmission signal (Fig. 5.5). Due the

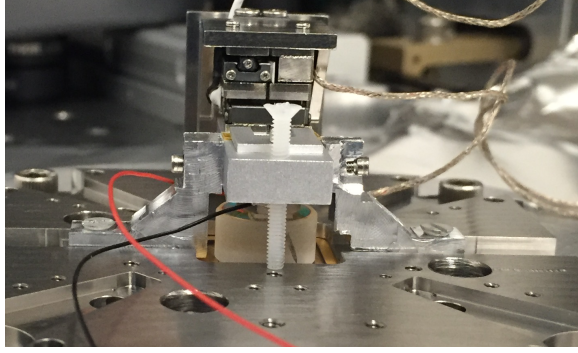


FIGURE 5.4: A picture of the experimental setup used for testing the cavity. The 3-axis stage was assembled to position the curved mirror above the ion trap. The clamps on both sides of the cavity are for securing the mirror mount once it is in the correct position, and the plastic screw on the end is for damping any remaining vibrations.

presence of several mechanical resonance peaks, I added two side clamps and a nylon screw to the setup to help dampen these vibrations. The side clamps significantly stiffened the cavity mount and pushed the resonance frequencies higher, while the nylon screw damped the vibrations and pushed the resonance frequencies lower. The combination of the clamps and the nylon screw led to an overall reduction in the vibration spectrum of the cavity, as shown by Fig. 5.5.

5.5 Cavity Optical Modes

The Gaussian beam is part of a larger class of solutions to the paraxial Helmholtz equation called the Hermite-Gaussian beams. This family of solutions forms a complex and orthogonal basis set for representing stable cavity modes (Siegman, 1986). While the Hermite-Gaussian solutions of order (l, m) differ in their amplitude distribution, their wavefront curvatures are identical. As a result, a resonator which has a stable Gaussian beam solution will also have higher order solutions from the family of Hermite-Gaussian solutions. Solutions of the same fundamental order n but a different (l, m) order will differ in their resonance frequency from that of the

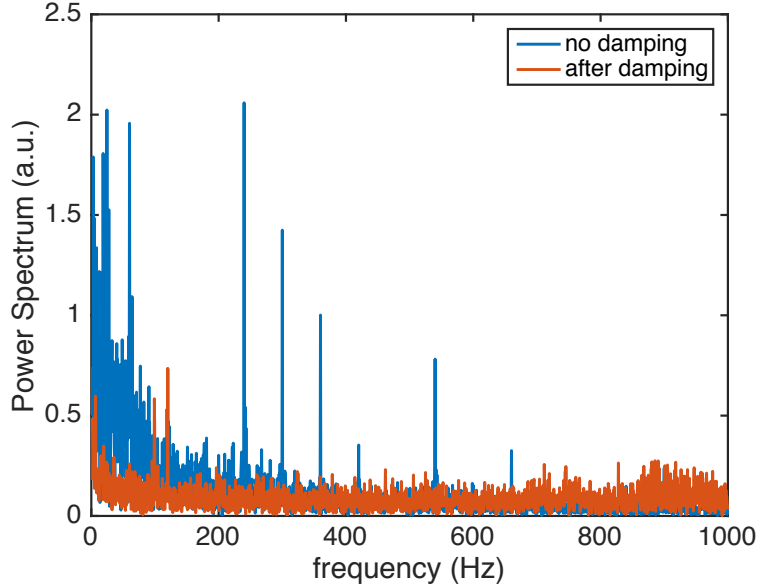


FIGURE 5.5: The background subtracted power spectral density of the cavity transmission calculated from the transmission measurements as a function of time by taking a Fourier Transform of the data. The peaks here correspond to mechanical resonances of the cavity mounting structure.

fundamental mode by

$$\nu_{l,m,n} = n\nu_f + \nu_f(l + m + 1) \frac{\cos^{-1}(\pm\sqrt{g_1g_2})}{\pi}, \quad (5.6)$$

where g_1 and g_2 are the cavity stability parameters of Eqn. 4.1. As the cavity approaches the confocal limit of $g_1 = 1$ and $g_2 \rightarrow 0$, $\cos^{-1}(\pm\sqrt{g_1g_2})/\pi \rightarrow 1/2$. For the micromirror cavity we tested with a length of $l = 285 \mu\text{m}$, the spacing between the $(0, 1)$ and $(1, 0)$ modes and the main $(0, 0)$ mode was 282 GHz, which is about half the full free spectral range of 526 GHz. We can see the evidence of the higher order modes when the cavity is slightly misaligned as in Fig. 5.6.

Measurement of the Gaussian beam parameters from Eqns. 4.2 - 4.4 will allow us to fully characterize the intracavity mode volume, V . The mode volume is an important factor for the ion cavity coupling rate, g , of Eqn. 4.8. Using a Spiricon

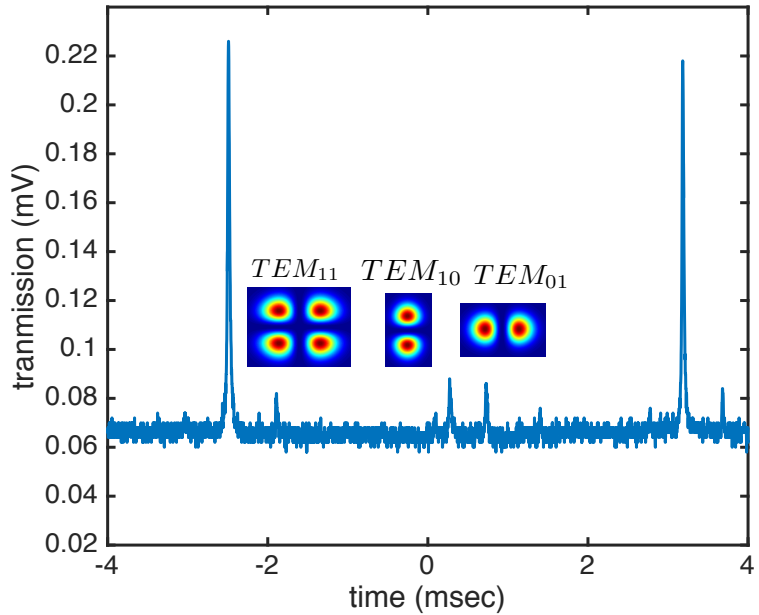


FIGURE 5.6: The cavity transmission as a function of time as the cavity length is scanned by the piezo electric actuator. The cavity supports stable transverse modes with varying spatial profiles which differ in frequency according to their mode number. The frequency splitting of the normally degenerate TEM_{01} and TEM_{10} modes is due to birefringence in the micromirrors which splits the frequency of different polarization modes.

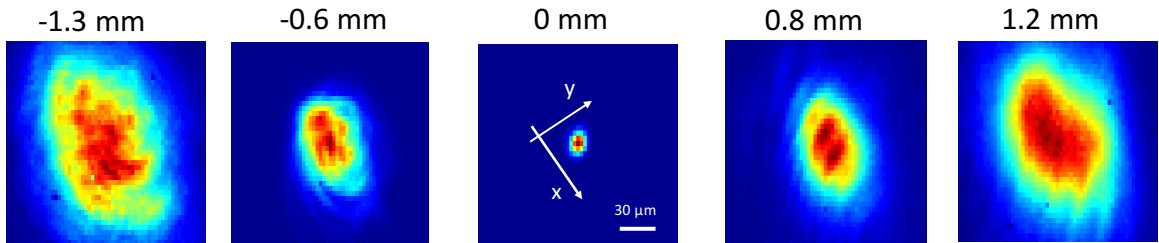


FIGURE 5.7: Images from a beam profiler showing the beam shape of the cavity mode. The distance numbers here correspond to the distance from the focusing lens to the center of the cavity. In this arrangement, the distance from the lens to the beam profiler sensor was fixed, and the combined lens and profiler assembly was moved together to measure the beam shape at various points with a fixed $2\times$ magnification.

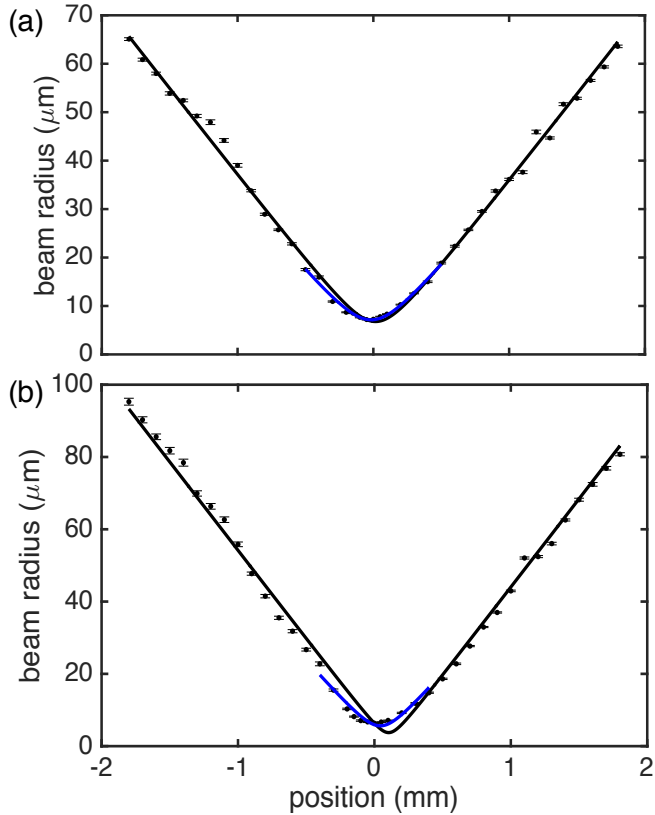


FIGURE 5.8: Measurements of the cavity beam size as a function of distance with corresponding fits to an ideal Gaussian beam along (a) the y-axis and (b) the x-axis.

beam profiler with an asphere imaging lens with a $2\times$ magnification, I measured the beam size of the cavity mode along its propagation direction. Sample images of the beam profile at several distances are shown in Fig. 5.7. Fig. 5.8 shows the $1/e$ radius of the beam along the two principal axes as a function of distance from the waist. For an ideal Gaussian beam, the beam size along the propagation direction is determined by the beam waist, w_0 and the wavelength λ . The divergence half angle of the beam away from the waist is given by $\theta = w_0/z_R = \lambda/\pi w_0$. The M^2 factor is called the beam quality factor and is a common measure of the quality of a laser beam. The M^2 factor can be calculated as

$$M^2 = \frac{\theta \pi w_0}{\lambda}. \quad (5.7)$$

A perfect Gaussian beam has a $M^2 = 1$. I found the divergence half angle, θ by fitting the beam profile away from the waist and found the measured waist value by fitting the beam profile close to the waist. For the y-direction I measure a value of $M_y^2 = 1.07$ with a waist radius of $7.2 \mu\text{m}$, and for the x-direction I measured $M_x^2 = 1.5$ with a waist of $5.6\mu\text{m}$.

5.6 Multiscale Optical Simulations

Extending the length of micromirror cavities without incurring additional losses from the mode spillover beyond their relatively small mirror apertures is one of the challenges which must be overcome to use these cavities for trapped ion quantum computing. The size of the cavity mode solution is characterized by the Fresnel parameter, $N_F = a^2/\pi w^2$, where a is the mirror aperture radius and w is the beam width at the mirrors. For mirrors with a Fresnel parameter $N_F \gg 1$, the finesse is independent of the cavity length and depends only on the losses and transmission of the mirror coatings. With micromirror cavities, the Fresnel parameter is $N_F \sim 1$ and the finite aperture of the mirrors can have a significant impact on the beam shape and the round trip mirror losses. A simplified model for the clipping losses was used for the calculations in Sec. 4.2 where the only effect of the mirror aperture was to cause a “spillover” loss of the optical power outside the aperture. In reality, the aperture will modify the beam shape itself by reducing its size on the mirror, and the clipping loss model will tend to overestimate the losses caused by the aperture. In this section, I present results of a more accurate numerical simulation method to find the cavity mode for the actual mirror shapes used in the experiments.

Methods for simulating cavity modes were investigated in the 1960s for building stable resonators for external cavity diode lasers. The method used for simulating a cavity mode first developed in Fox and Li (1968) was to start with a generic optical mode and apply successive iterations of the cavity propagator until the mode

converged to the fundamental cavity mode solution. The resonator transformation can be modeled as a linear system characterized by the impulse response function $h(x, y; x', y')$ with stable solutions being the eigenfunctions of the equation

$$\mu U(x, y) = \int \int_{-\infty}^{\infty} h(x, y; x', y') U(x', y') dx' dy'. \quad (5.8)$$

If the impulse response function is known, the cavity modes can be found by solving Eqn. 5.8 for the eigenfunctions $U(x, y)$.

The technique developed by Fox and Li for solving the cavity eigenvalue equation is to start with a trial solution U_1 and use the impulse response function to calculate the field after one round trip pass through the cavity, labelled U_4 , as shown in Fig. 5.9. The set of resonant cavity modes for an ideal cavity form an orthogonal set of basis functions with which to write any general field solution. Introducing a finite aperture to the cavity mirrors will cause more round trip loss for modes which have a larger size at the mirrors. After many round trip iterations, the field distribution will converge to the solution with the lowest loss, which is the cavity mode with the smallest beam size on the mirrors. This method can therefore be used to find the fundamental mode solution to the eigenvalue integral in Eqn. 5.8. We have adapted the Fox and Li method to find the lowest order optical mode solutions for our micromirror cavities.

We can write the impulse response function for the cavity within the paraxial approximation as a combination of the Fresnel propagator,

$$h_F(x, y, z) = \frac{e^{ikz}}{i\lambda z} e^{i\frac{k}{2z}(x^2+y^2)}, \quad (5.9)$$

and the curved mirror propagator,

$$h_m(x, y) = e^{-2ikh_t(x, y)}. \quad (5.10)$$

The height profile of the mirror is given by the function $h_t(x, y)$. The field distribution on the curved mirror, U_3 is multiplied by the pupil function $P(x, y) = 1$ for $\sqrt{x^2 + y^2} \leq a$ and 0 otherwise, where a is the radius of the curved mirror aperture. This field is then propagated back to the flat mirror to find U_4 . As we iterate the cavity mode back and forth between the two mirrors with a sufficiently small aperture radius a , the mode profile eventually converges to the lowest energy eigenmode solution, which is the solution with the smallest beam radius on the curved mirror, namely the TEM_{00} mode. The round trip energy loss converges to the square of the eigenvalue of Eqn. 5.8. The rate of convergence is dependent on the aperture radius since a smaller radius increases the relative loss per mirror reflection of the higher order modes when compared with the lowest energy eigenmode. Once the fundamental mode solution is found, I then relax the aperture constraint and propagate the solution one more time through the cavity to find the overlap integral with itself after one round trip. The modulus squared of this overlap provides an estimate of the round trip losses in the cavity. These losses are used to calculate the expected finesse as a function of cavity length as shown in Fig. 5.14.

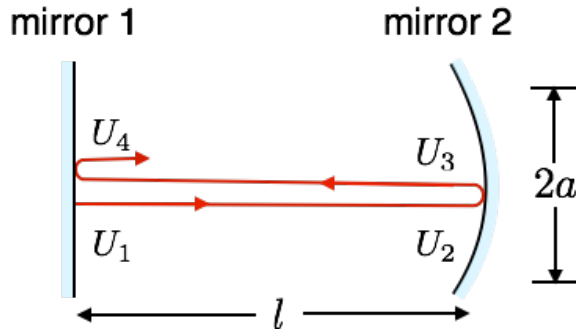


FIGURE 5.9: The lowest order cavity eigenmode can be found by repeated iteration of a plane wave through the cavity using the Fresnel propagator and the curved mirror propagator found from the profilometer measurements.

The lowest order eigenmode solutions of the cavity for several cavity lengths are

shown in Fig. 5.10. There I plot the beam radius of the simulation eigenmode in the vertical and horizontal directions, as well as the Gaussian solutions calculated with Eqn. 4.15 (solid lines) using the measured radius of curvature of the mirror at its center. For shorter cavity lengths below about $300 \mu\text{m}$, the beam shape is well approximated by a Gaussian function which matches the solution of a uniform RoC mirror. Above $300 \mu\text{m}$, however, the cavity mode distorts due to the aberrations introduced from the mirror shape and finite aperture, and its size is smaller than that of the Gaussian solutions. This implies that at these lengths the clipping losses calculated from the Gaussian solutions using Eqn. 4.16 will tend to overestimate the losses for a given aperture size when compared with the losses of the actual cavity mode. Using this cavity simulation tool, we can get a good approximation of the cavity mode shape for each mirror we make and this can significantly speed up the optimization of our mirror fabrication procedure as each mirror will not have to be tested in an actual cavity to know if it is suitable for eventual use in a cavity QED experiment. This is particularly important for the micromirror cavities as it is relatively easy to make many of these mirrors on a single substrate, so having a way to test them independently with a simulation tool is an efficient way of finding the particularly good mirrors in each batch.

5.7 Finesse Measurements and Simulations

In this section I show the results of measuring the finesse of a micromirror cavity. As explained in Sec. 5.6, the finesse will depend on the cavity length when the beam size on the curved mirror approaches the aperture size. To measure the finesse as a function of length, I increment the mirror separation using the SmarAct SL1720 positioner in steps of about $10\text{-}20 \mu\text{m}$, and scan the length of the cavity at each point using the piezo electric transducer attached to the micromirror substrate. The main 780 nm light is locked to a Rb spectroscopy signal using Doppler-free saturated ab-

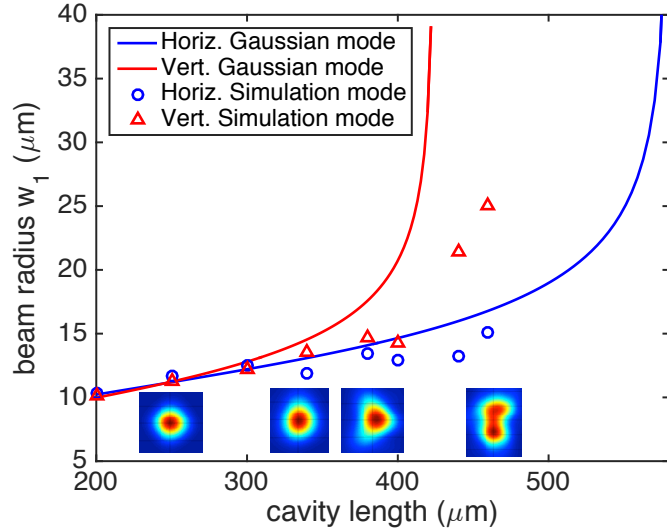


FIGURE 5.10: The mode size found from the simulations is compared with an ideal Gaussian beam solution for a uniform RoC mirror of $R = 580 \mu\text{m}$ in the horizontal direction and $R = 424 \mu\text{m}$ in the vertical direction. The inset plots show the 2D beam profile from the simulation below its corresponding cavity length data point. The accuracy of the Gaussian approximation for the beam shape decreases as the length is increased above about $300 \mu\text{m}$, where aberrations caused by the mirror shape start to significantly distort the beam.

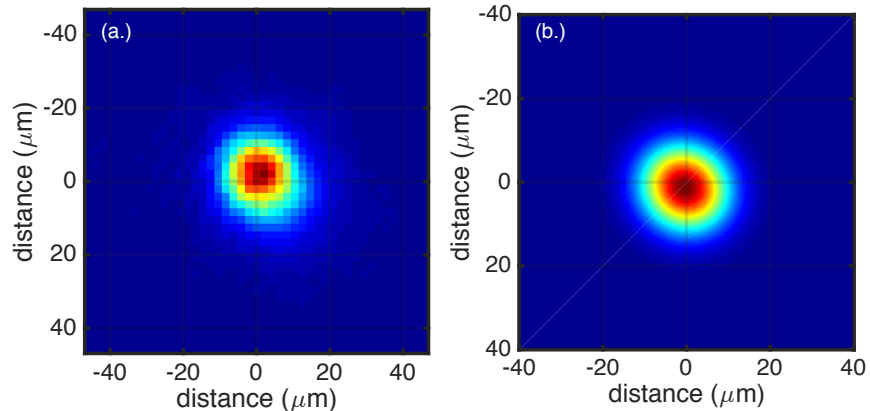


FIGURE 5.11: (a) The measured intensity distribution of the cavity mode of wavelength 780 nm on the beam profiler and (b) the intensity distribution found from the simulation of the cavity mode, showing a close match between simulation and experiment.

sorption spectroscopy. A second 780 nm laser, called the interference filter (IF) laser after its method of achieving laser feedback, with a frequency difference of around 300 GHz from the Rb stabilized laser, is simultaneously applied to the cavity to provide a calibration for measuring the free spectral range ν_f . From this measurement, I determined the cavity length as $l = c/2\nu_f$. To measure the linewidth, I modulated the input Rb stabilized laser using a fiber EOM (from the vendor EO Space) at a frequency of around $f_{mod} = 2.5$ GHz. This created modulation sidebands on either side of the transmission peak with a frequency separation of f_{mod} , and allowed us to determine the cavity linewidth from the frequency calibration provided by the two sidebands. A typical scan for measuring the finesse is shown in Fig. 5.12, with the inset plot showing the measurement of the linewidth.

I performed finesse measurements on two sets of micromirrors. The results from the first set are shown in Fig. 5.13. These mirrors were part of the first exploratory batch made and had a radius of curvature of around 350 μm , while their diameter from estimates with a spherical fitting function was only around 40 μm . Their relatively small diameter limited the length of cavities that could be made from those mirrors to under around 150 μm in length before the clipping losses became prohibitively large. We then made a second batch of mirrors with larger diameters in the 70 – 90 μm range which were able to successfully reach cavity lengths of around 250-300 μm that needed for eventually trapping ions inside the cavity. The finesse measurements from this second batch of mirrors are shown in Fig. 5.14 along with the results from a numerical simulation of the cavity finesse using the technique described in Sec. 5.6.

There are several observations to make about the data shown in Fig. 5.14. Firstly, the length of the cavity plotted on the horizontal axis is measured using the IF reference laser, as shown in Fig. 5.12a, and the horizontal error bars on the data show the uncertainty in this length due to the cavity drifting during the measurements.

In addition to these errors, there is also potentially a systematic error due to any nonlinearity in the piezo scan over the 390 nm scan range needed to cover one free spectral range. The uncertainty in the overall length from this effect can be estimated by comparing the separation between neighboring Rb laser and IF laser transmission peaks for two pairs of peaks along the same scan. In Fig. 5.12a, it is apparent that the separation of the left pair of peaks is slightly larger than that of the right pair. From comparisons of how the peak spacing changes along a piezo scan, we can estimate the systematic error from a nonlinear piezo scan to be around 5-10 μ m. One way to reduce this error would be to take several measurements with the IF laser at frequencies differing by 100s of GHz, which would sample several intervals

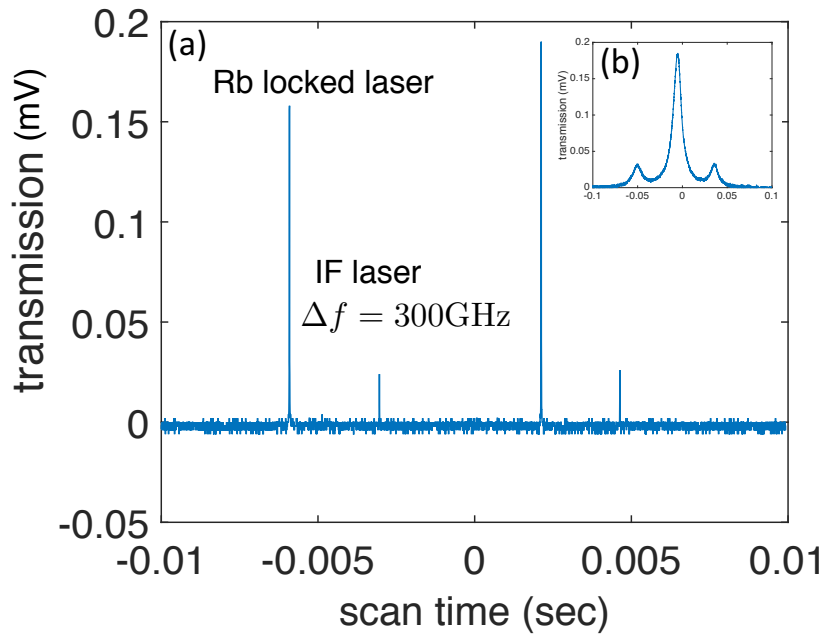


FIGURE 5.12: (a) By applying a triangle wave voltage to the piezo electric actuator in the cavity to scan its length, we find transmission peaks corresponding to the lengths where each of two lasers incident on the cavity satisfy the resonance condition of $l = N\lambda/2$. (b) Modulation sidebands on the cavity transmission of 2.5 GHz allow us to measure the linewidth by fitting each peak to a Lorentzian lineshape and using the sideband spacing to convert scan time into frequency.

along the piezo scan curve. For our purposes, however, the amount of uncertainty in the length measurements of up to 3-5% is small enough that it does not change the conclusions drawn from our measurements that stable cavities over $300 \mu\text{m}$ in length are feasible with our current micromirror fabrication process. Since the finesse plotted on the vertical axis is calculated from the length measurement, it too may contain a small systematic error from a nonlinear piezo scan. The vertical error bars shown are derived from the length and linewidth uncertainty due to mechanical vibrations and drift of the cavity. Since we do not have an independent measurement of the mirror coating losses which affect the finesse, we cannot determine the finesse on an absolute scale independent of any systematic errors. However, for comparison I did measure the finesse of a macroscopic cavity containing $R=10 \text{ cm}$ mirrors from the same coating run with a cavity length of about 12 mm. This cavity had a somewhat higher finesse of 2400. I attribute the lower baseline finesse of the micromirror cavity to its enhanced surface roughness and non-uniformity of the reflective coating over the small mirror aperture. For the final UV coatings to be used in the cavity QED experiment, we can specify the mirror transmission, reflectance, and losses to set an absolute scale for the cavity finesse based on the requirements of the experiment. A final observation for this data is that the simulation model does not take into account variations of the surface roughness over the mirror which may cause increased losses as the cavity mode size on the mirror increases. Efforts to reduce this surface roughness by improving the fabrication process and characterizing the samples with an AFM are currently underway as part of a future phase of this project.

5.8 Cavity Stability and Active Feedback Lock

Active stabilization of the cavity length is required to maintain the resonance matching condition between the ion and cavity frequencies. The cavity resonance frequency is inversely proportional to the cavity length as $f = Nc/2l$, where N is the integer

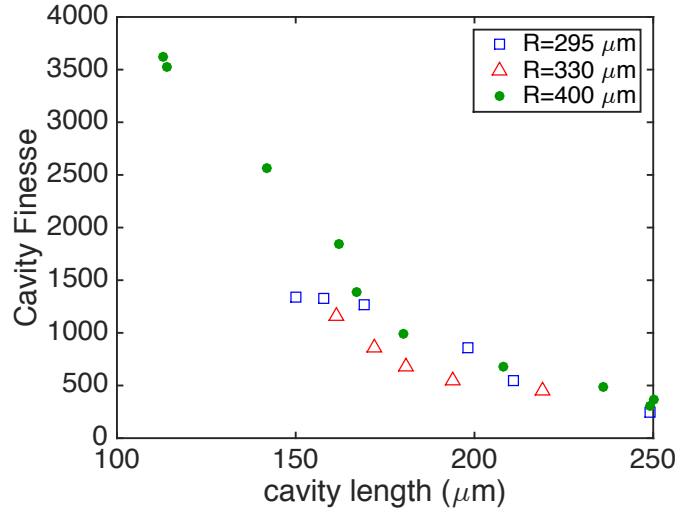


FIGURE 5.13: Measured data of the cavity finesse as a function of length for three mirrors from the first batch of samples coated. The finesse was obtained by measuring the free spectral range and the linewidth, and taking $\mathcal{F} = \delta\nu/\nu_f$. These cavities were limited from sustaining the sufficiently long cavity lengths required for ion trapping by the mode clipping losses from their relatively small diameters.

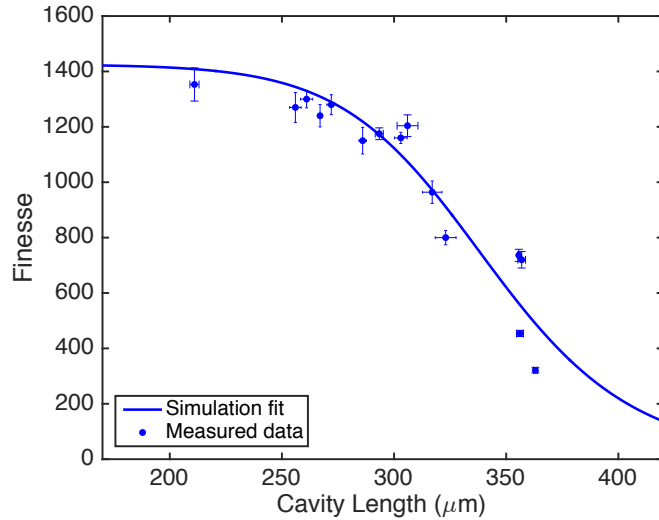


FIGURE 5.14: Measured data of the finesse as a function of cavity length for a micromirror from the second coating run, labelled as M2R2. The simulation curve was generated with the software described in Sec. 5.6 using an aperture diameter of $2a = 58 \mu\text{m}$.

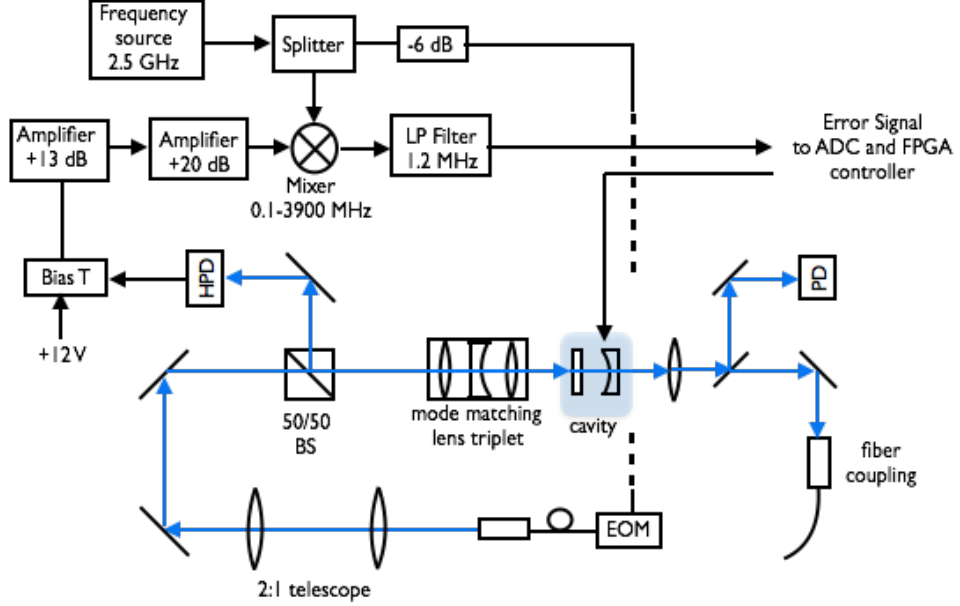


FIGURE 5.15: Schematic of the optical and electronic system used for locking the micromirror cavities. The cavity length is controlled by a high voltage feedback signal generated from a digital controller reading in the PDH error signal.

number of half wavelengths inside the cavity. A small change δl in the cavity length will give rise to a frequency change of $\delta f = -Nc\delta l/2l^2$, or $\delta f/f = -\delta l/l$. The linewidth of the cavity quantifies the spectral bandwidth at which the cavity transmission drops to half its peak value on both sides of the resonance frequency. The linewidth is dependent on the loss per mirror bounce of the light inside the cavity and on the frequency with which the light hits the mirrors, given by $\delta\nu = \nu_f/\mathcal{F}$. I measured the linewidth using a phase modulator to add frequency sidebands to the carrier light, as shown in Fig. 5.12. For the cavity regime we are working in with relatively small diameter mirrors (i.e. $a \approx 30 \mu\text{m}$), the linewidth depends on the cavity length as l approaches R since in this limit, the finite mirror aperture increases the clipping losses and therefore also increases the linewidth. For the test cavities I made, the linewidth was measured to be around 400 MHz for cavity lengths of around $300 \mu\text{m}$ which are in the length range relevant for cavity QED experiments.

5.8.1 Pound-Drever-Hall Technique

The Pound Drever Hall (PDH) method has become an industry standard method for frequency locking a laser to an optical cavity, as it has achieved such spectacular performance that lasers stabilized to under 1 Hz are now common (Millo et al., 2009). We are interested in using this technique in the opposite way, namely we want to use a stable laser to provide a reference signal with which to lock the cavity's resonance frequency. The PDH technique uses frequency modulation to generate a discriminant signal from light reflected off the cavity which can distinguish between the two conditions of the cavity being slightly below or slightly above resonance. The key to this technique is measuring a quantity proportional to the derivative of the intensity, which is antisymmetric about the resonance point. Above the resonance, the derivative of the reflected intensity is positive, while below resonance, the derivative is negative because the lower sideband is 180° out of phase with the upper sideband. By measuring the derivative of the reflected intensity, a discriminant can be obtained using a mixer to coherently extract the component of the reflected signal at the modulation frequency. The sign of this signal will depend on whether the upper or lower sideband is reflected (due to their phase difference of 180°), and hence provides a linear error signal to act as feedback for stabilizing the cavity length. To implement this method, I use a fiber EOM from EOSpace to modulate the light at a frequency of $\Omega_{mod} \approx 2.5$ GHz, which is about an order of magnitude greater than the linewidth of the cavity. The phase modulation of the electric field after the EOM becomes

$$E_{inc} = E_0 e^{i(\omega t + \beta \sin \Omega_{mod} t)} \approx E_0 (J_0(\beta) e^{i\omega t} + J_1(\beta) e^{i(\omega - \Omega_{mod})t} - J_1(\beta) e^{i(\omega - \Omega_{mod})t}), \quad (5.11)$$

with $\omega = 2\pi c/\lambda$ and modulation amplitude given by β . The phase modulation therefore gives rise to modulation sidebands at frequencies $\omega \pm \Omega_{mod}$.

On resonance, the main beam is almost fully transmitted into the cavity, and the reflected beam is a sum of the off resonant modulation sidebands which are exactly

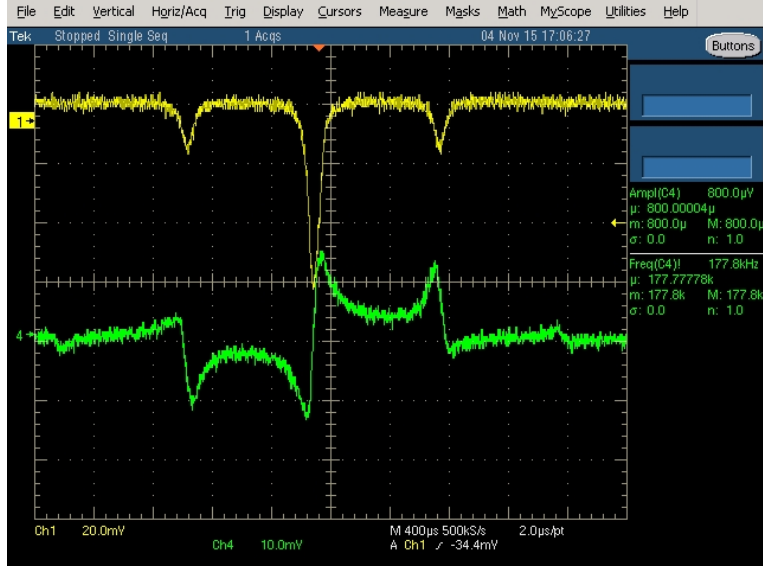


FIGURE 5.16: The PDH error signal (lower, green trace) and the inverted transmission signal (upper, yellow trace) from a 2.6 GHz modulation of the input 780 nm wavelength light to the cavity. The PDH error signal shows the characteristic three peak structure for modulation frequencies which are large compared to the cavity linewidth, which was 400 MHz.

out of phase and of the same amplitude, and will therefore cancel. If the cavity is not perfectly on resonance with the laser, then the phase difference between the two reflected sidebands will not be 180° anymore and they will not cancel. The net sum of the reflected field will be positive for a cavity which is slightly too long and negative for a cavity which is slightly too short. The strongest error signal is obtained when the modulation frequency is much higher than the linewidth (i.e. at least an order of magnitude higher). Under this condition, most of the light is reflected when the carrier is near resonance, and $F(\omega \pm \Omega_{mod}) \approx -1$. To first order in $F(\omega)$, the reflected power is then

$$P_{ref} \approx 2P_s - 4\sqrt{P_c P_s} \text{Im}[F(\omega)] \sin \Omega_{mod} t. \quad (5.12)$$

The demodulated signal scales linearly with the laser deviation from resonance, $\delta\omega$,

and close to resonance is given by the expression

$$\epsilon \approx -\frac{4}{\pi} \frac{\sqrt{P_c P_s}}{\delta\nu} \delta\omega \quad (5.13)$$

for a modulation frequency Ω_{mod} , cavity linewidth $\delta\nu$, sideband power P_s , carrier power P_c , and reflected power $P_{ref} = P_0|F(\omega)|^2$. This error signal is therefore proportional to the frequency difference between the cavity and the laser δf as $\epsilon = D\delta f$, with a proportionality constant of $D = -8\sqrt{P_c P_s}/\delta\nu$ (Black, 2001).

5.8.2 Digital Controller

I designed and built a digital PI (Proportional-Integral) controller to provide feedback for maintaining the cavity on resonance at a specific frequency using the PDH error signal described in Sec. 5.8.1. There are many good reasons for using a digital controller rather than an analog one. Some of the advantages include that it allows for monitoring and recording of the error signal history, averaging of the error signal over varying time intervals to set the correct feedback response rate, using a graphical interface for setting the control parameters, and setting up conditional interlocks to prevent runaway feedback loops.

The layout of the controller board was made with CadSoft Eagle PCB design software and is shown in Fig. 5.18. The philosophy behind making this board was to make it versatile enough to be used in many different applications throughout the lab. The integration of a HV264 surface mount high voltage amplifier from Supertex Inc. onto this board makes it useful for any applications involving piezo electric transducers, which generally require voltages in the range of 0-150 V. There are four analog input channels and four analog output channels on the board, a USB connection for communicating with a field programmable gate array (FPGA), 16 digital input channels, and 16 digital output channels. The four analog inputs have unity gain differential op amps for reducing electrical noise on the input. These

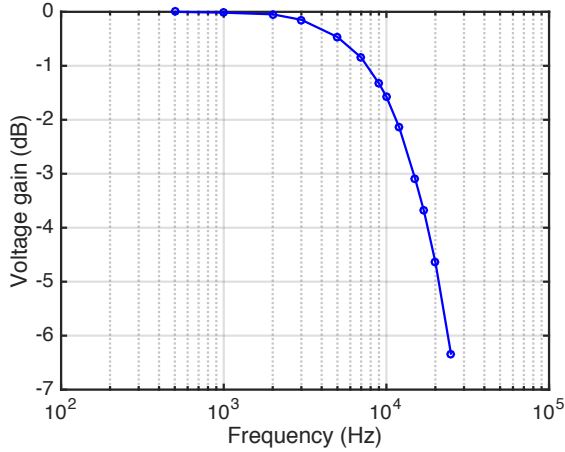


FIGURE 5.17: The gain of the high voltage DAC output as a function of frequency. The -3 dB bandwidth of the voltage controller is around 10 kHz, which is larger than the mechanical response bandwidth of the cavity mirror of around 2 kHz.

are connected to two analog to digital (ADC) converters (ADC122S101 from Texas Instruments), which are low power, 2 channel, 500 ksps to 1 Msps, 12 bit ADCs. These ADCs can read in an input signal of up to 3.3 V and convert it to a 12 bit digital value with a precision of $3.3\text{ V}/2^{12} \approx 0.8\text{ mV}$. The frequency response of this controller is characterized in the Bode plot shown in Fig. 5.17. The four analog inputs also have the option of being soldered directly to the amplifier to use the board as a simple high voltage amplifier. The digitized input voltages from the ADC are read into the FPGA at a clock rate of up to 1 Msps. The FPGA is an Altera Cyclone II model, which is a low cost FPGA with up to 1.1 Mbits of RAM and operates with a 50 MHz clock. I programmed this board with Quartus design software from Altera in the Verilog hardware description language (HDL). A sample of the Verilog code used to write the PI controller is shown in Appendix A.

5.9 Cavity Stabilization Results

Stabilizing the length of the micromirror cavities described in this work required both passive stabilization in the form of rigid and soft damping mechanisms as well as

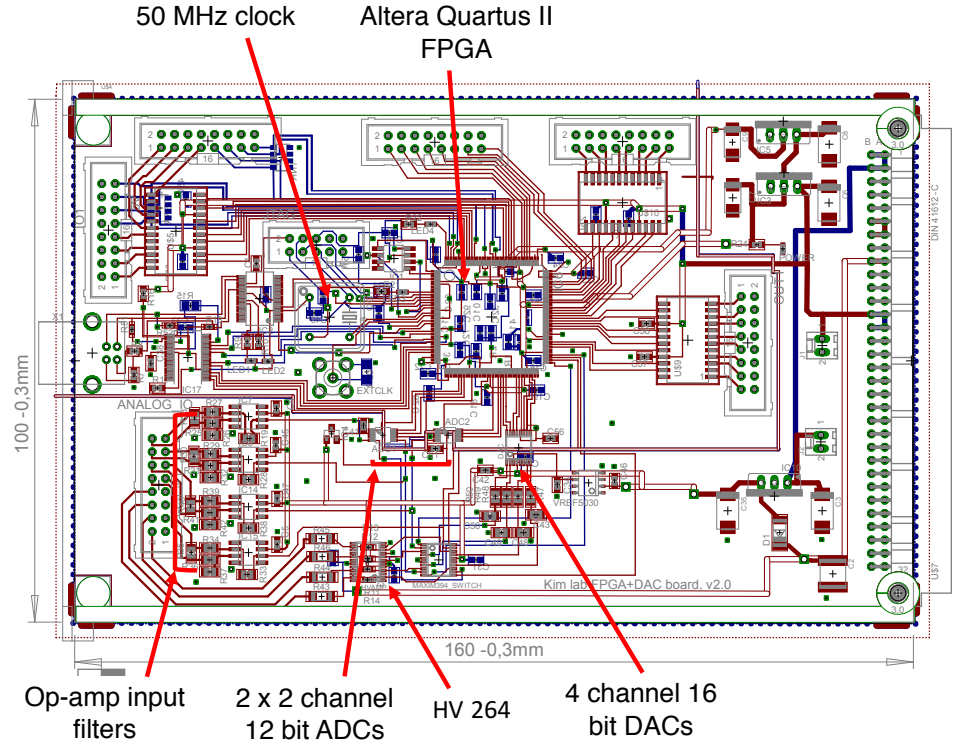


FIGURE 5.18: The integrated FPGA, DAC, ADC, and high voltage amplifier circuit board used to implement a digital control lock for the cavity.

active stabilization with a digital PI controller, as described in the previous sections. Such cavities present a challenge in this regard because of their relatively short length compared to conventional mirror cavities. From the relation $\delta l = -l\delta f/f$, we see that for a given cavity frequency f and linewidth δf , the degree to which the length must be stabilized to stay on resonance with the laser scales proportionally with the cavity length. Using the Rb locked 780 nm laser to generate an error signal with the PDH technique, I was able to stabilize the cavity length to within 1.8 ppm of the total length of 300 μ m. The cavity transmission signal measured over the course of several minutes is shown in Fig. 5.19. This data is shown in both length and frequency scales, and the lock performance is comparable to that shown in fiber cavities (Gallego et al., 2016). By also monitoring the frequency spectrum

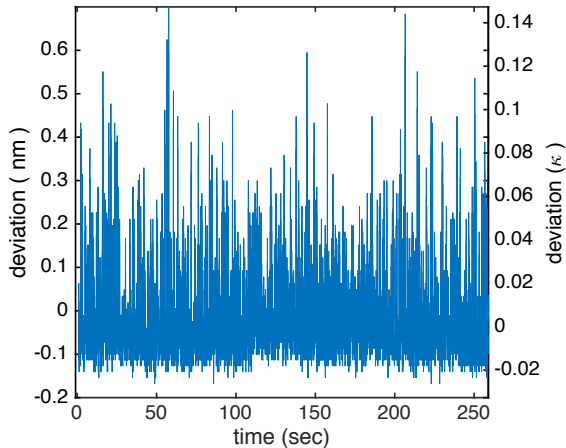


FIGURE 5.19: The cavity lock performance in units of fluctuation distance and linewidth (κ) monitored over a period of several minutes.

of the electrical noise on the feedback signal, I determined the lock bandwidth of the feedback loop from the frequency at which the feedback lags the error signal by 180° . This was indicated by characteristic peaks in the noise as the feedback switches sign from negative to positive. For our system, I measured the lock bandwidth to be around 1.93 kHz. This bandwidth was limited by the mechanical response time scales of the piezo electric transducer moving the mirror substrate. These findings represent some very promising results showing the feasibility of achieving the kind of length scale stabilization required for eventually locking the cavity resonance to the atomic transition line of a trapped $^{171}\text{Yb}^+$ ion.

5.10 Fiber Coupling

One of the unique features of our cavity design is that the laser ablated micromirrors are made on a fused silica substrate rather than on the tip of an optical fiber. This approach has several advantages, most significantly that it allows for easier integration with the ion trap and allows for much higher fiber coupling efficiencies, especially at UV wavelengths, as outlined in Sec. 5.3. The fiber mode matching factor for fiber

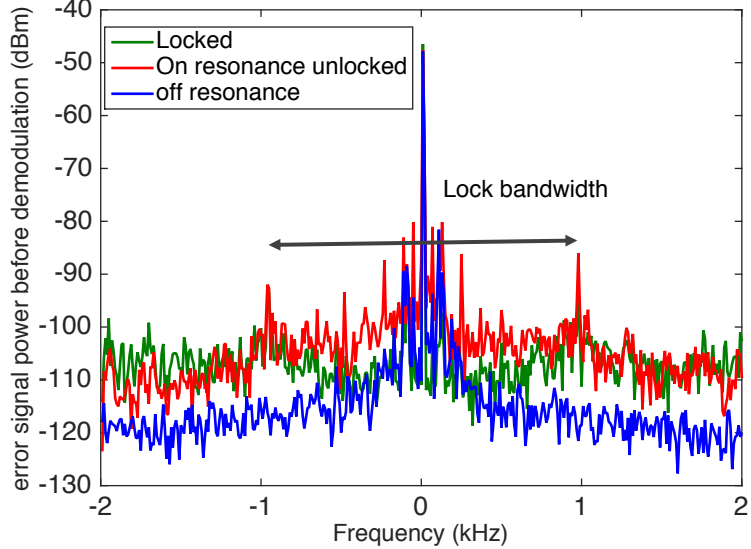


FIGURE 5.20: The frequency spectrum of the noise on the cavity lock feedback signal. When the feedback becomes 180° out of phase with the error signal, the sign of the feedback switches from negative to positive. For positive feedback, the noise increases and two spikes in the spectrum develop at these frequencies. The width between these peaks gives a measure of the lock bandwidth, which in our system was measured to be around 1.93 kHz.

Fabry-Perot (FFP) cavities scales as the beam size on the fiber, w_f , and the fiber's mode size, w_m , as

$$\epsilon = \frac{4w_f^2 w_m^2}{(w_f^2 + w_m^2)^2 + (\pi n_f w_f^2 w_m^2 / \lambda R)^2}, \quad (5.14)$$

where n_f is the index of refraction of the fiber and R is the mirror radius of curvature (Hunger et al., 2010). This mode matching factor scales as the square of the ratio of the fiber mode size to the beam size on the mirror, $\epsilon \sim (w_f/w_m)^2$. We are targeting a length of $l \approx 300 \mu\text{m}$ and a radius of curvature of $R \approx 370 \mu\text{m}$ for our cavities, and cavity solutions for this geometry have a waist of $w_m = 9 \mu\text{m}$. From Eqn. 5.14, the expected fiber mode matching for a single mode (SM) fiber at $\lambda = 370 \text{ nm}$ is found to be $\epsilon = 0.18$. As the cavity length is increased, this mode matching factor will decrease even further, which represents a significant drawback of the FFP approach

for our applications.

I built a setup to test the fiber coupling efficiency of our test cavity at 780 nm wavelength. I used a custom made triplet lens design to collimate the light from the cavity mode and then focus it back down into a SM fiber with a fiber collimation package from the vendor Schafter-Kirchoff. The triplet collimation lens consisting of a planar concave lens placed in between two planar convex lenses was secured to a 3-axis translation stage for alignment to the cavity. The lens design for this collimator was simulated with the Zemax Optical Simulation software to identify the best off-the-shelf lenses for collimation of the beam at a distance of about 50 mm away from the cavity. By comparing the detected optical power without the optical fiber to the power collected into the fiber (assuming negligible loss in the fiber of length 1 m), I found a fiber coupling efficiency of around $68.8 \pm 2\%$. This provides a factor of 3.5 times improvement over the value estimated for a FFP cavity. A Zemax simulation of this system predicts that we should be able to achieve a $\sim 95\%$ fiber coupling efficiency using the arrangement of lens just described if the cavity mode were a perfect Gaussian mode. However, we know from the beam profile measurements that the actual cavity mode is not only astigmatic but also has a non-ideal beam shape characterized by a M^2 factor greater than one. While limitations of the beam shape are partially determined by the cavity mirrors, the astigmatism can in principle be corrected with cylindrical lenses, for example, which should allow us to push this fiber coupling percentage closer to the targeted 90% level.

6

Quantum Performance Simulator

Quantum computation (QC) represents a new paradigm in computing capable of providing exponential speedup over classical computation approaches for certain algorithms, and has been an intense field of research from both a physical hardware and computer science perspective over the past two decades. Various quantum algorithms have been discovered to show the power of QC, including Shor’s factoring algorithm (Shor, 1994) and Grover’s unstructured search algorithm (Grover, 1997). Quantum assembly languages have been developed to formalize the process of compiling algorithms into basic executable logic elements (Metodi et al., 2006).

Just as with classical computers, effective mapping and optimized scheduling of the logic elements on practical quantum hardware platforms requires knowledge of the hardware architecture. QC poses additional challenges on this mapping and scheduling process as the physical systems representing quantum bits (qubits) suffer from decoherence processes and faulty gate operations, leading to a loss of quantum information during the computation. Fault-tolerant (FT) procedures based on quantum error-correcting codes (QECCs) were established to overcome this chal-

lence, which comes at the cost of additional physical resources, computation time and higher levels of operational complexity. FT requires that (1) the entire computation is performed on encoded qubits for protection against errors. For a given physical error probability p , it also requires that (2) all operations on the logical qubits keep the logical error probabilities within the range correctable by the QECC up to first order in p . Finally, (3) an error introduced by qubit measurement process should have probabilities of order p^2 (Nielsen and Chuang, 2000). We will refer to these as FT conditions. Furthermore, the *threshold theorem* proves that scalable QC is possible using error correcting codes, as long as (1) the error probability for the physical process is below a certain threshold value (*error threshold*), and (2) sufficient quantum and classical resources are available to implement the error correction codes necessary to ensure FT (Aharonov and Ben-Or, 1997). Although detailed procedures for achieving FT are well-established, quantitative estimates of the resource overhead, computation time and resulting performance gain (in terms of reduced error probability) require an automated software tool due to the complexity of these procedures. Previous work has proven the existence of a rigorous lower bound on the error threshold for distance-3 concatenated codes, such as the Steane code considered here (Cross et al., 2009; Aliferis et al., 2006). Our work serves as a generalization of this type of analysis by numerically finding an error threshold and tracking the individual error probabilities of qubits throughout the execution of a full quantum circuit. Tracking the logical qubit failure probability at any point in a circuit allows us to pinpoint circuit bottlenecks and failure points. This method overcomes the limitation of many Monte Carlo based analyses where simulating low error rates becomes prohibitively slow (Steane, 2003). Additionally, our quantum performance simulator keeps track of the resource and computation time overhead of running a given circuit and, combined with tracking the error probabilities, provides a means to evaluate the effectiveness and optimize the choice of FT strategy for a finite-size

quantum processor.

6.1 QUIPSIM Overview

We present here the design of our QUantum Information Processor SIMulator (QUIPSIM) which is a tool to analyze a FT implementation of a quantum algorithm to gain quantitative information about its effectiveness, efficiency, and feasibility. The primary goal of this tool is to elucidate the limitations imposed by faulty hardware and finite resources on quantum algorithms at a scale that is feasible for implementation. We establish performance metrics for fault tolerant quantum circuits based on the number of ancilla qubits necessary (representing resource overhead), time steps (representing execution time), and overall error probability of the qubits at the end of a computation.

We consider first a general set of gates necessary to construct an arbitrary quantum circuit. Pauli operators (gates) span the operator space of a single qubit, and consist of four operators (I , X , Y , and Z). Pauli operators on multiple qubits are defined as tensor product of Pauli operators acting on individual qubits. A set of Pauli operators form a group called Pauli Group, denoted by \mathcal{P} . Another important group is called the Clifford group \mathcal{C} consists of operators (gates) that satisfy

$$\mathcal{C} \equiv \{U | \forall P \in \mathcal{P}, UPU^\dagger \in \mathcal{P}\}. \quad (6.1)$$

\mathcal{C} contains Pauli operators, along with the Hadamard gate, the CNOT gate, and the phase gate, S.

The Gottesman-Knill theorem shows that it is possible to efficiently simulate a quantum circuit containing only Clifford group gates on a classical computer. In order to achieve the true speed up of a universal QC, one must be able to use at least one non-Clifford group gate, such as the $T = \begin{pmatrix} 1 & 0 \\ 0 & e^{i\pi/4} \end{pmatrix}$ gate (also known as

the $\pi/8$ gate) or the Toffoli gate (three qubit control-control-NOT gate, where the state of the target bit is flipped if and only if both control bits are $|1\rangle$).

We define the error probability of a qubit from its qubit *fidelity*, a metric used to characterize the degradation of an actual qubit from an ideal, error-free state. The qubit fidelity between a pure state $|\psi\rangle$, representing an ideal, error-free state, and a mixed state with density matrix $\hat{\rho}$, describing the actual qubit subject to various errors, is defined as $F(\hat{\rho}, |\psi\rangle) = \text{tr} \sqrt{\langle\psi|\hat{\rho}|\psi\rangle}$ (Nielsen and Chuang, 2000). A fidelity of one denotes that the actual qubit is identical to the ideal qubit indicating no error, while a reduction in fidelity corresponds to an error on the actual qubit. For example, an ideal quantum state $|\psi\rangle$, subject to a bit flip error with a probability of p , can be described by a density matrix ρ with a corresponding fidelity given by

$$\rho = (1-p)|\psi\rangle\langle\psi| + pX|\psi\rangle\langle\psi|X \quad (6.2)$$

$$F = \sqrt{(1-p) + p(\langle\psi|X|\psi\rangle\langle\psi|X|\psi\rangle)}. \quad (6.3)$$

We define the error probability as $\epsilon \equiv 1 - F^2$, representing the probability by which the qubit state differs from the ideal state. Similar concepts of fidelity and error probability can be extended to quantum logic gate operations. If one obtained a density operator ρ_U after applying a gate U on an initial state $|\psi\rangle$ instead of the ideal result $U|\psi\rangle$, the fidelity of the gate operation U is defined as $F(U) \equiv \min_{|\psi\rangle} F(U|\psi\rangle, \rho_U)$, where minimization is taken for all possible initial states $|\psi\rangle$. For example, if a quantum logic gate operation U is subject to a bit-flip error with a probability of p , the fidelity of the gate is given by $F(U) = \sqrt{1-p}$, and the error probability of the gate is adequately determined to be $\epsilon = 1 - F^2 = p$.

For a more complex quantum circuit, the upper bound of the error (or failure) probability for a given circuit can be estimated from the error probabilities of individual qubits and gates. The encoding, decoding (error correction), logic gate operation and detection procedure of logical qubits encoded with a QECC each constitute a

quantum circuit block, and these circuit blocks can be assembled to construct any encoded quantum circuit implementing a universal quantum computation. QUIPSIM tracks the failure probability of each logical qubit circuit block (defined as a probability of a failure occurring on the logical qubit that cannot be corrected by error correction procedure) throughout the entire algorithm as a way to optimize FT protocols and track circuit failure points. Using this approach, QUIPSIM provides a means to bridge the gap between theoretical proofs of FT and realistic error probabilities that must be reached for an experimental realization of a FT quantum processor.

The logical qubit states in QUIPSIM are encoded using a stabilizer code called the Steane [[7,1,3]] code (Steane, 1996). Stabilizer codes are an important class of QECCs where the symmetry of the codewords is described by a set of Pauli operators called *stabilizers*, which reflect the parity check properties of the code (Gottesman, 1998). Valid codewords of a stabilizer code are eigenstates of every stabilizer of the code with an eigenvalue of +1, analogous to the valid code words of a classical code that fulfills the parity check conditions. For the Steane [[7,1,3]] code used in QUIPSIM, $m = 7$ physical qubits are used to encode $k = 1$ bit of information in a logical qubit, with a “distance” between any codewords of $d = 3$ (i.e. a minimum of three bit-flip or phase-flip errors are needed before one codeword transforms into another). This code has the capability of identifying one bit-flip error and one phase-flip error on any of the constituent qubits of an encoded state from the results of the six stabilizer measurements. Furthermore, it has the property that all gates in the Clifford group can be performed *transversally*, defined as applying the gate in a bit-wise fashion to individual constituent qubits of the code. Since a single error from one constituent qubit does not propagate to become two errors on the same encoded qubit, transversal gates automatically satisfy the FT requirement. The procedures for ensuring FT in stabilizer measurement and non-Clifford group

gates are well established for the Steane code (Zhou et al., 2000). Implementing a quantum algorithm using a QECC such as the Steane code requires a finite set of encoded operations, or logical code blocks, that include ways to prepare, measure and error correct encoded quantum states.

QUIPSIM starts with a compiled quantum circuit, where the target algorithm is constructed using a universal set of logical circuit blocks. The implementation of QUIPSIM can be divided into two main parts. The first is a Fault Path Counter (FPC), which estimates the failure probability of each logical circuit block in the universal set by counting the number of error paths that lead to uncorrectable errors in the circuit block. The second part of the tool runs a simulation of the overall compiled quantum circuit by recording the execution time and order of each logical gate under finite resource limitations, and tracking each logical qubit's failure probability throughout the computation. Here I present in more detail the implementation of these two operations.

6.1.1 Fault Path Counter

The purpose of the FPC is to determine the overall likelihood of an uncorrectable error occurring for each of the encoded logical gate blocks in a quantum circuit. QUIPSIM keeps track of the logical failure probability to represent this quantity. The FPC computes the logical failure probability of the encoded circuit block from the failure probability of each physical qubit operation by counting the number of ways in which physical errors accumulate to yield an incorrect logical state of the qubit when error correction is performed. A fault tolerant circuit block constructed for an error correcting code of distance d can perfectly recover from k errors occurring anywhere in the block if $k \leq (d-1)/2$. However when $k > (d-1)/2$, error propagation can result in an incorrect logical state of the qubit with probability $O(p^k)$. Since our analysis is based on the Steane [[7,1,3]] code with $d=3$, all gates containing two or

more errors cause a logical failure and should be counted as a fault path. When p is small, the higher order terms in the logical failure probability (i.e. $O(p^3), O(p^4)$ and so on) can be neglected with nominal inaccuracy. Our FPC counts the number of failures resulting from only two-error events, and estimates the failure probability of a logical circuit block from this number. The counting procedure is repeated for all combinations of two-error events, each occurring at $\binom{n}{2}$ locations for a circuit block containing n possible fault sites. From this total number of fault paths C , the FPC outputs the logical failure probability of Cp^2 for each encoded operation. Fig 6.1 shows several examples of how error propagation is handled in the FPC.

Critical to the use of a FPC is that most quantum circuits can be broken up into a universal set of encoded operations which can be used to construct an arbitrary quantum circuit. By breaking down the circuit into its constituent blocks, we can run the FPC on a smaller subset of the full circuit, which makes fault path counting a tractable problem. These circuit blocks include logical state preparation of a $|0\rangle_L$ state (logical zero), error correction, CHP (controlled-not, Hadamard, and Pauli) gates, quantum measurement, and at least one non-Clifford group gate. The implementation details of these gates in QUIPSIM are discussed in Sec. 6.2.

A logical failure of an encoded qubit is an event of two or more bit flips, phase flips, or both in an encoded block of seven physical qubits. The FPC works by choosing a two-error event out of the n total physical operations and propagating those errors through the circuit block by commuting Pauli error operations through the constituent gates. A logical failure of the gate is counted if a logical error is detected at the end of propagation. Not all such two error events cause a logical failure. Fig 6.1b shows an example where error cancellation can occur. The FPC repeats the same procedure for all possible two-error events (nC_2) and computes the sum C as the total number of logical failures. Once C is obtained, the block is assigned the logical failure probability Cp^2 . While QUIPSIM can handle other

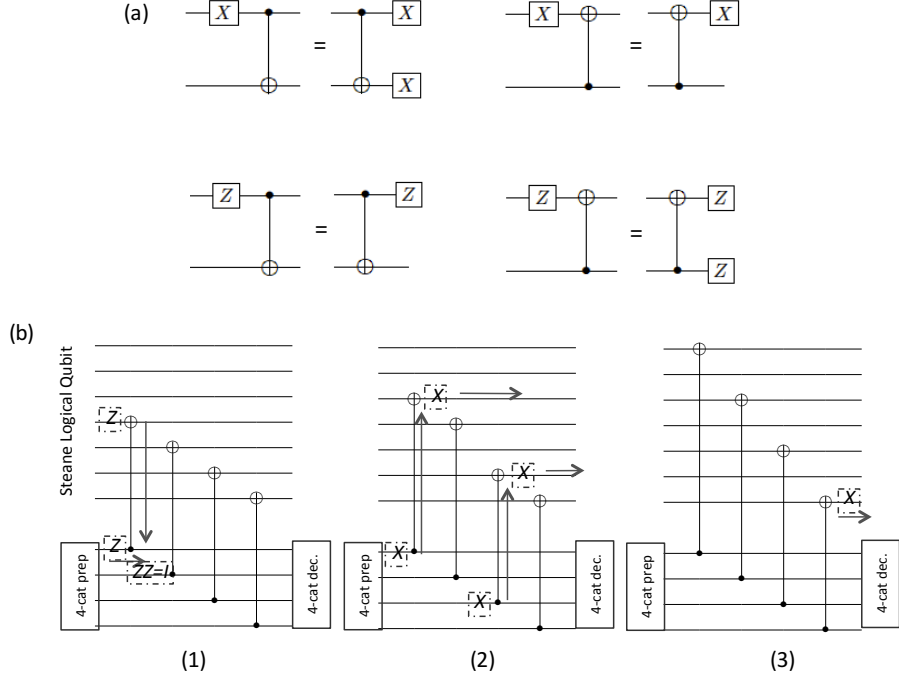


FIGURE 6.1: (a) Propagation of X and Z errors through CNOT gates. (b) Example run of the fault path counter for the Steane error correction block. An error event containing two Z errors (1) did not cause logical failure because they cancel out. An error event containing two X errors (2) propagated to cause a logical failure in the Steane logical qubit. A single error (3) is free to propagate but does not constitute a logical failure.

non-Clifford group gates, we use the Toffoli gate to form a universal gate set in all examples presented here.

6.1.2 Performance Simulation

The code organization for the scheduling part of the QUIPSIM program is shown in Fig. 6.2. We implement a hierarchical structure from the computer down to the individual physical qubits in the registers. The overall quantum computer class contains a sub-class of quantum registers to store the qubits, and a resource queue to store the available ancilla and physical resources to run parallel operations. Physical resources represent anything needed in physical hardware to perform gates, e.g.

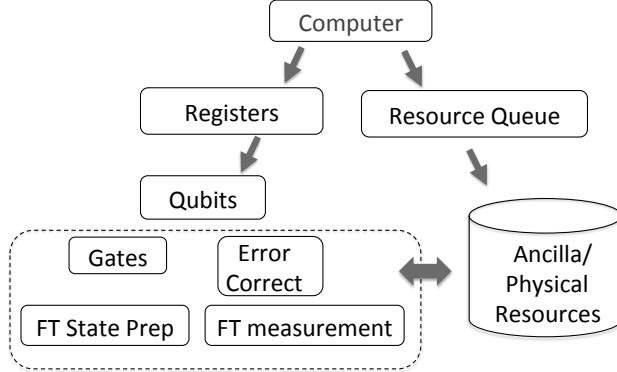


FIGURE 6.2: Code organization for the QUIPSIM program. The computer object is made up of registers which store qubits and a globally shared resource queue of available ancilla and physical resources. Qubit operations, including gates, error correction, state preparation, and state measurement, are executed under the constraints given by the availability of ancilla and physical operational resources.

lasers, controller hardware, any qubit interaction channels, etc.. Each register has its own hardware and ancilla. Inside the quantum register class is the qubit class, which stores the qubits inside the actual registers and performs all the logical and physical level gate operations. Each qubit keeps track of its availability time, logical error probability, and level of concatenation. This organization of smaller qubit registers connected with a low bandwidth bus is meant to model a modular approach to quantum computing hardware (Monroe and Kim, 2013).

6.2 Implementation of Quantum Operations

Here I summarize in more detail the procedures adopted in QUIPSIM to break a logical gate operation down into its constituent operations at a lower level of concatenation. I also describe how we account for the fidelity of the resulting qubits in each of these circuit blocks with logical error probabilities derived from running the FPC on each block. For this analysis, we consider the case that after each gate one performs an error correction step by measuring the stabilizers. While the circuit for error correction will be described in Sec. 6.2.5, the important consequence of this

operation is that the fidelity of each logical block can be found independent of which gates may have acted previously on a given qubit. That is, the error correction step allows the single qubit errors after the logical gate to be independent of the single qubit errors caused by the gate itself. This is because the error correction step will either fix the single error and possibly cause a new error, or else compound the error, which will then be two errors and will contribute to the error probability to $O(p^2)$. The logical gate fidelities found from the FPC after the error correction step are functions of this input single error probability per qubit, labeled as x . We estimate that the logical qubit has a probability of $70 \cdot p$ of containing a single error to $O(p)$ for the Steane error correction procedure implemented in QUIPSIM. This number is derived from the roughly 10 failure points of each of the six stabilizer measurements and single recovery operation involved in the error correction. The analysis presented here is for a single type of error, either X or Z, so the total error probability including both types of errors would be double the values shown here for an error model with equal occurrences of X and Z errors, such as the depolarizing channel.

6.2.1 Single Qubit Gates

A compete set of single qubit gates used in QUIPSIM include the Pauli operators and the Hadamard operator. Since each of these operators can be implemented transversally, each gate is replaced by the necessary bit-wise single qubit operations at the constituent level. The logical fault paths are for two errors from two of the individual single qubit gates with a logical error probability of $42p^2$, a single error from the gate and a preexisting error with a probability of $42xp^2$, and for two preexisting errors with a probability of $42x^2p^2$.

6.2.2 Two Qubit (CNOT) Gate

The CNOT gate is also transversal in Steane code, so the logical CNOT gate is replaced by bit-wise CNOT operations at the constituent level. Fig. 6.1a shows the circuit identities that describe the processes of error propagation through CNOT gate. A X (Z) error on the control (target) qubit propagates to the target (control) qubit, while a X (Z) error on the target (control) qubit is contained in the target (control) qubit and does not propagate to the control (target) qubit. The fault path counter uses these error propagation rules to find the number of combinations where the output logical qubits have two uncorrected errors. The three cases for logical failure to occur are with two errors by the CNOT gates with a probability of $42p^2$, when one preexisting error combines with one caused by the gate with probability of $84xp^2$, and when there are uncorrected existing errors on any two of the constituent qubits in the gate with a probability of $182x^2p^2$.

6.2.3 Cat State Preparation

One common procedure which must be implemented in stabilizer-based FT quantum computation is preparation of maximally entangled states called cat states, used primarily for FT measurement. The typical preparation scheme for a four qubit cat state is shown in Fig. 6.3. The first four qubits form a cat state after the Hadamard and first three CNOT gates are applied. The probability that the cat state generated contains errors is proportional to the error probability of a single gate p , and is not good enough for use in FT measurement. A fifth verification qubit is introduced to check the parity of the first and the last qubits in the cat state, using the last two CNOT gates and the measurement. If the parity is odd, the cat state is discarded and the cat state preparation is repeated. This measurement step is repeated three times for each cat state, and we take the majority vote of the measurement results as the parity. If the parity is even, the generated cat state has an error probability

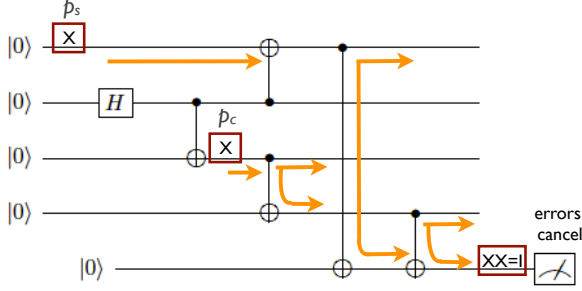


FIGURE 6.3: Preparation of a cat state with an example of error propagation through the circuit.

of $O(p^2)$ and is ready for use.

To verify the error probability of the cat state prepared in this way, we trace the fault paths of possible X and Z errors through the circuit in Fig. 6.3. Any single X error in the process will propagate to the verification qubit and be detected. The final fidelity of an l -qubit cat state is derived by counting the number of ways in which the verification qubit fails to detect one or more errors remaining in the prepared cat state. Fig. 6.3 shows an example of such an occasion, where the physical state preparation error in the first qubit is cancelled at the verification qubit by an error in the first CNOT operation (modeled as a X error on the target qubit following the CNOT gate), resulting in two qubits flipped in the cat state. We note that Z errors cannot be detected in this scheme, but show in the next section that these cat states can still be used to effectively perform FT stabilizer measurements.

6.2.4 State Preparation and Qubit Measurement

QUIPSIM uses the Steane encoding scheme to prepare the logical $|0\rangle_L$ states, achieved by measuring the six stabilizers on an arbitrary (mixed) state of seven physical qubits. Each stabilizer measurement uses a 4-qubit cat state, as shown in Fig. 6.4 (Nielsen and Chuang, 2000). We choose the approach that uses six separate 4-qubit cat states to measure the stabilizers simultaneously rather than recycling a single cat state, to

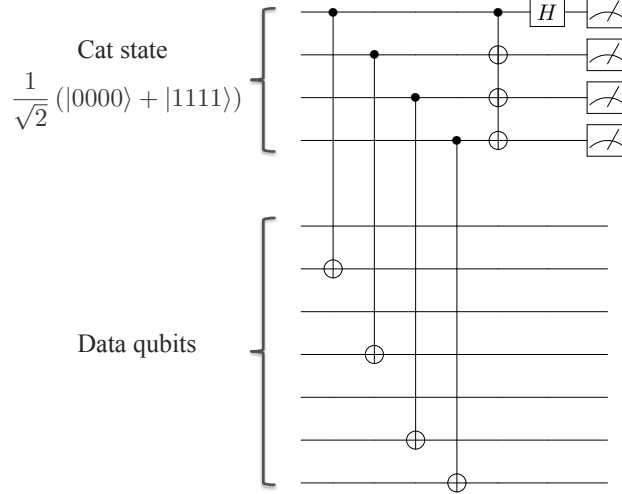


FIGURE 6.4: FT measurement of the $g_2 = IXXIIXX$ stabilizer of the Steane code using a 4-qubit cat state. In total, six stabilizer measurements such as this are used in both state preparation and logical error correction.

allow for execution in parallel at the cost of more ancilla resources. We note that an efficient protocol does exist that uses decoding circuits to correct any errors in the cat state after it has interacted with the data qubits, which can speed up the use of a single cat state for the stabilizer measurements (DiVincenzo and Aliferis, 2007). After all the CNOT gates are performed, we measure the first qubit in each of the six cat states to determine the eigenvalue of the stabilizer. From the six measurement results we can decode not only if there was an X or Z error in the logical qubit, but also on which physical qubit the error occurred (Gottesman, 1998), allowing for a correction operation to be applied.

If the cat state used for the measurement is prepared using the procedure shown in Fig. 6.3, the stabilizer measurement is FT against a single X error propagating into the data qubits. Any Z error in either the cat state preparation or the stabilizer measurement process does not propagate into the data qubits (due to the error propagation rules shown in Fig. 6.1), but will result in an error in the stabilizer readout. Errors in the measurement process itself lead to a similar result in the

stabilizer readout with error rate $O(p)$. Since correction operations on the data qubits are performed based on the result of the stabilizer measurement, this will lead to an error probability in the data qubit of $O(p)$, violating the FT condition. To overcome this, QUIPSIM performs the measurement of each stabilizer generator three times and uses the majority vote on the (classical) readout results to decide if the correction operation should be applied. This gives a logical error probability of $O(p^2)$ in the presence of Z errors.

The logical error probability found using the FPC on the six stabilizer measurements is $p_L = (3789 + 372x + 72x^2)p^2$. For logical state preparation, we take $x = 0$ since we are starting from randomized initial qubits. For any other stabilizer measurements, we take $x = 70/7 = 10$, which is the average error probability on each of the seven constituent qubits following an error correction step.

After all six stabilizer measurements, we must perform a logical Z measurement to see if the logical qubit is in the $|0\rangle_L$ or $|1\rangle_L$ state. This process is done by preparing a 3-qubit cat state and measuring the parity of the first three qubits, as in Fig. 6.5. The parity is measured three times to reduce the measurement-induced error to $O(p^2)$. If the Z measurement indicates a result 1, then the state $|1\rangle_L$ is prepared while a measurement result of 0 indicates the $|0\rangle_L$ state. This serves as the qubit state detection process.

By itself the logical Z-measurement as shown in Fig. 6.5 is susceptible to failure with the presence of a single Z error in the data qubits. This is because a single Z error in the data qubits can propagate to the measurement ancilla and flip the sign of the measurement result. Simply performing the measurement operation three times will not alleviate the effects of this single Z error in the data qubits since the error will propagate through to all three measurements. While a single Z error will not constitute a logical failure in the encoded qubit, it can cause the detection process to fail with $O(p)$, thereby violating the FT condition. Even if an error correction gate

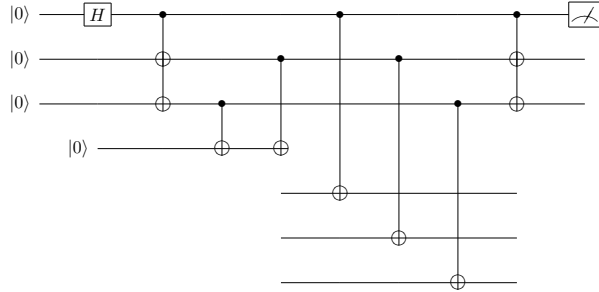


FIGURE 6.5: Typical state measurement in the Z basis. The measurement operation M_z shown here, even when performed three times, is not fault tolerant because a single Z error in the data qubits can spread to multiple physical measurements, thereby causing a logical error. For this to be fault tolerant, we need to implement a full Z stabilizer measurement between each M_z measurement.

is performed before the measurement, there is still a probability on the order of $70p$ that there remains a single Z error in the encoded qubit, which will cause a failure in the measurement. Adding a full error correction step before each measurement is one possible solution, but this performs many redundant operations since we are only concerned with checking for Z errors and not X errors. A simpler solution is to just perform the Z stabilizer measurement before each state measurement.

Using the notation of M_z for the Z basis state measurement shown in Fig. 6.5 and S_z for the Z stabilizer measurement, we can write our fault tolerant measurement procedure as

$$FTM = M_z S_z M_z S_z M_z S_z. \quad (6.4)$$

A single Z stabilizer measurement, S_z , can fail with probability $O(p)$ due to a Z error in the qubit or a simple failure of the physical measurement procedure. Therefore, we need to combine the results of the three Z measurements and the two Z stabilizer measurements to determine if, in fact, the data had a Z error and correct it before proceeding with subsequent operations. The value of interspersing these S_z measurements within the M_z measurements is that they make potential single Z

errors in the data independent between measurements. In other words, each error can affect at most one of the three M_z unless a subsequent error occurs in the data or the S_z measurement, which is then $O(p^2)$. This will allow the complete measurement operation to satisfy the FT conditions.

The final measurement result is interpreted from a majority vote of the three M_z and S_z measurements taken. If there was a Z error in the data qubits, it will show up in the stabilizer measurements and indicate that our Z measurement result was flipped. The entire measurement string must be taken into account when determining the measurement result. For example, a measurement string of '000111' from Eqn. 6.4, where a 1 for an S_z indicates an error was detected in the stabilizer and a 0 indicates no errors, means we can conclude that a Z error occurred in the data after the second S_z but before the second M_z . Furthermore, we conclude that the logical qubit was in the $|0\rangle$ state but contained a Z error which flipped the last two measurement results. Taking the majority vote of all measurements ensures that the outcome is protected against a single failure in the measurement process. The FPC logical error probability of this FT measurement is a combination of the stabilizer measurement errors and the logical qubit measurement errors, which combine to give a logical failure probability of $p_L = (796 + 83x + 16x^2)p^2$.

6.2.5 Error Correction

The part of the state preparation process which measures the six stabilizers and applies the associated correction factors is a sufficient error correction procedure. QUIPSIM uses the state preparation process of Sec. 6.2.4 less the logical Z measurement as the error correction procedure, which ensures that the qubit state is projected back into the code space without actually measuring the qubit itself. The fidelity of the qubits after error correction is calculated by adding the probability of two situations where (1) data qubits do have an error, and the syndrome measurement

does not detect an error, and (2) data qubits had no error but the syndrome detection detects one, and a correction procedure was applied. This estimation accurately reduces the remaining error probability after error correction is applied to $O(p^2)$. All other situations lead to error probabilities of $O(p^3)$, and can be safely ignored in the limit of low physical error probabilities. QUIPSIM implements this by calculating the probability that the stabilizer measurements during error correction have an error. Since measurements are repeated three times, the final fidelity is reduced to $f \approx 1 - 9p_{meas}^2$. While this is just an approximate expression, the implementation by the simulator computes a more accurate value by finding the measurement failure probability p_{meas} for each of the stabilizers, and combining them to get the probability that the error correction mistakenly finds an error when none is present or does not detect an error when one is present.

QUIPSIM performs an error correction step after each logical operation. This prevents errors from propagating between code blocks to $O(p^2)$ because any error is either caught by the correction step or else has a second error in the detection and is not caught. There remains, however, a probability that a single error exists in the data after the error correction is performed. This can be a result of the seven final stabilizer measurements or any of the potential correction operations applied by the error correction. This amounts to approximately a single error probability of $70p$ after error correction. These single errors coming into each block are accounted for with the FPC in calculating the logical fidelity of each gate with the x variable in the FPC results.

6.2.6 Fault Tolerant Toffoli Gate

Many of the simplest quantum operations necessary for stabilizer-based fault tolerant protocols, such as state preparations and measurements, fall into the category of Clifford group gates. As shown by the Gottesman-Knill theorem, it is possible to

efficiently simulate a quantum circuit containing only Clifford group gates (such as the Pauli gates, H, and CNOT) on a classical computer (Gottesman, 1998). In order to get to the true speed up of a quantum computer and achieve universal quantum computation, one must be able to use at least one gate from the set of non-Clifford group gates, such as the Toffoli gate or the T-gate. A Toffoli gate can be thought of as a controlled-controlled-not gate on three qubits. The question of achieving universal quantum computation relies on the ability to perform at least one non-Clifford unitary gate, such as the Toffoli gate. Here we evaluate the performance of a fault-tolerant Toffoli gate, since this is the operation in the universal gate set which has the largest error probability.

Unlike gates in the Clifford group, a fault tolerant version of the Toffoli gate cannot be implemented transversally. A fault tolerant version of the Toffoli gate considered here requires the preparation of what is called a Toffoli magic state, $|\phi_+\rangle$. This can be prepared using a 7-qubit cat state and three logical ancilla qubits in a known state $|000\rangle_L$, as shown in Fig. 6.6a (Zhou et al., 2000). These three ancilla are then used to create the magic state using fault tolerant CNOT, Hadamard, and Z measurement, with the addition of a bit-wise Toffoli gate. The resulting three qubit entangled state replaces the first two Hadamard gates and the Toffoli gate in the boxed part of the circuit shown in Fig. 6.6a. We assume for this analysis that the physical hardware can perform a Toffoli gate at the physical level, where experimental demonstrations exist (Monz et al., 2009). All remaining operations consist of CNOTs, controlled- Z gates (which can be implemented with one CNOT and two Hadamard gates), qubit measurements and single qubit gates, which can be simulated fault tolerantly by QUIPSIM.

Fig. 6.7 shows the error probability of the FT Toffoli gate circuit with one level of encoding as a function of the physical error probability. It shows that below physical error probabilities of $p_{th} \sim 7 \times 10^{-6}$, the encoded gate has a lower error probability

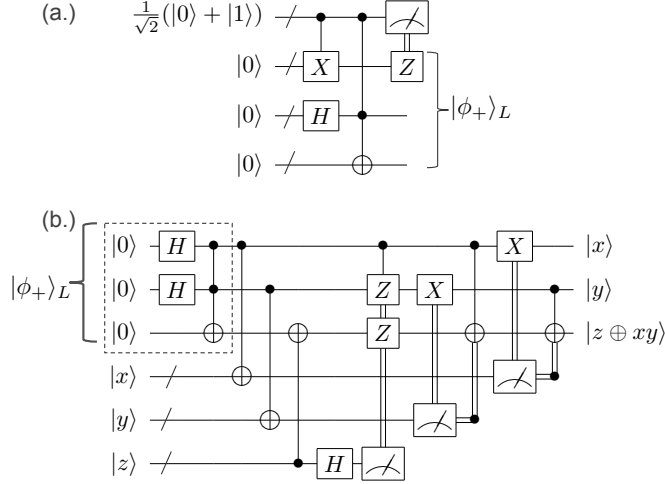


FIGURE 6.6: Fault tolerant circuit for the Toffoli gate. The first part of the full Toffoli circuit shown in (b) (boxed region) can be replaced with the magic state preparation of $|\phi_+\rangle_L$ shown in (a).

than the unencoded one. This data was taken in the no memory error limit where the decoherence rate is much longer than the gate time. Since the FT Toffoli gate has the highest error probability of all the gates in the universal set described here, this error value can be thought of as a threshold error probability since the FT implementation of any other gates decreases the overall error probability when the physical error probability is lower than this value.

Table 6.1: A summary of the error rates for common FT operations performed in QUIPSIM. Here $x \cdot p$ is the probability of a single error on each of the seven constituent qubits of a logical qubit. For the analysis presented here, I use $x = 70/7 = 10$.

| | |
|------------------|----------------------------|
| Single Qubit | $(42 + 42x + 42x^2)p^2$ |
| CNOT | $(149 + 98x + 196x^2)p^2$ |
| Error correction | $(7512 + 491x + 42x^2)p^2$ |
| FT Measurement | $(796 + 83x + 16x^2)p^2$ |
| Physical Toffoli | $(21 + 84x + 98x^2)p^2$ |

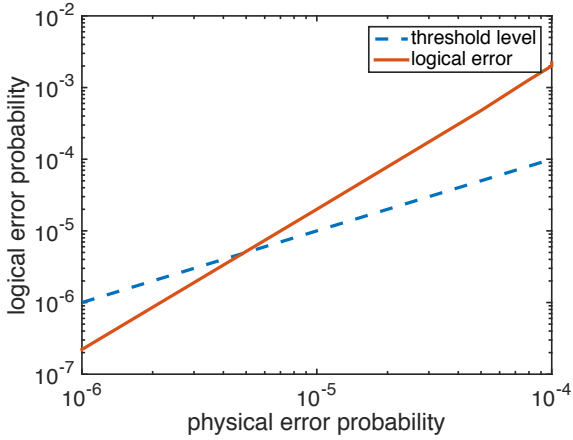


FIGURE 6.7: Logical error probability of the FT Toffoli gate as a function of the physical error probability. From this data, we estimate an error threshold of approximately 6×10^{-6} .

6.3 Quantum Adder Circuits

The most celebrated application of quantum computation is Shor’s algorithm, which involves modular exponentiation (ME) and quantum Fourier transform (QFT) (Shor, 1994). An n -bit ME is a classical arithmetic circuit, but requires $O(n^3)$ operations compared to the $O(n^2)$ operations for QFT and dominates the computation time. The algorithmic optimization of ME circuit has been considered, and the performance is dictated by the ability to implement efficient quantum adders (Van Meter and Itoh, 2005). Several authors have proposed optimized versions of various known adder circuits to fit into the quantum domain (Cuccaro et al., 2004; Draper et al., 2006; Draper, 2000; Gossett, 1998), reducing the number of resource-intensive Toffoli gates and depth of the circuit. As an example application of QUIPSIM, we compare the execution time, resource requirements and error properties of two adders: quantum ripple carry adder (QRCA) and the quantum carry look-ahead adder (QCLA). Optimized QRCA features $2n + O(1)$ Toffoli gates and has depth of $2n + O(1)$ for n -bit addition (Cuccaro et al., 2004). QCLA features $5n - O(\log n)$ Toffoli gates and

has $O(2 \log n)$ depth (Draper et al., 2006). Results are shown in Fig. 6.8 and Fig. 6.9 that verify a linear running time of QRCA and a logarithmic time for QCLA in our simulation tool.

6.4 Performance Evaluation

In this section we show examples of some performance simulations demonstrating the capabilities of QUIPSIM. Although QUIPSIM is capable of independently setting the operation times and error probabilities for each physical gate type, we made the simplifying assumption to normalize every physical gate time to one with an associated error probability of p in the examples shown here. This allows us to explore the more generic behavior of the circuits as a whole. QUIPSIM has the capability of adding in more specific details to a particular physical system, such as varying error rates, modular qubit registers, and qubit-photon entanglement operations. We also simplify the memory error by setting the decoherence rate to zero in order to isolate the effects of gate error in a system with no memory errors. Physical measurement times are assumed to be 200 times the gate time, to reflect the realities of ion trap experimental situations where state readout is significantly slower than qubit gates. One important assumption we made was regarding the connectivity of the qubits in the system. In any experimental setup, detailed physical implementation of a two qubit gate between a pair of qubits in the system may depend on their relative location, providing additional constraints on the performance measures. One should make assumptions about how to realize two qubit gates between distant pairs of qubits. In our model, we make the simplifying assumption that a two qubit gate can be applied between any pair of qubits in the system, i.e. the system has full connectivity.

The performance of QRCA and QCLA circuits is evaluated with and without the use of FT encoding. Fig. 6.8 shows the execution time of the two circuits measured in units of physical gate times. While the fault tolerant encoding of the circuits gives

a substantial increase in the execution time (around three orders of magnitude), it does not change the nature of the circuit depth. As a result, the QRCA still scales linearly in the adder size and the QCLA still scales logarithmically in the adder size with approximately the same scale factor as the unencoded adder. Fig. 6.9 shows the average error probability of the output qubits for the FT QCLA circuit as a function of the adder size. At error probabilities below threshold ($p_{th} \sim 7 \times 10^{-6}$), the final logical error probability of the circuit is lower than the physical error probability, as FT behavior would suggest. The transition above threshold corresponds to a sharp decline in logical final fidelity with increasing adder size.

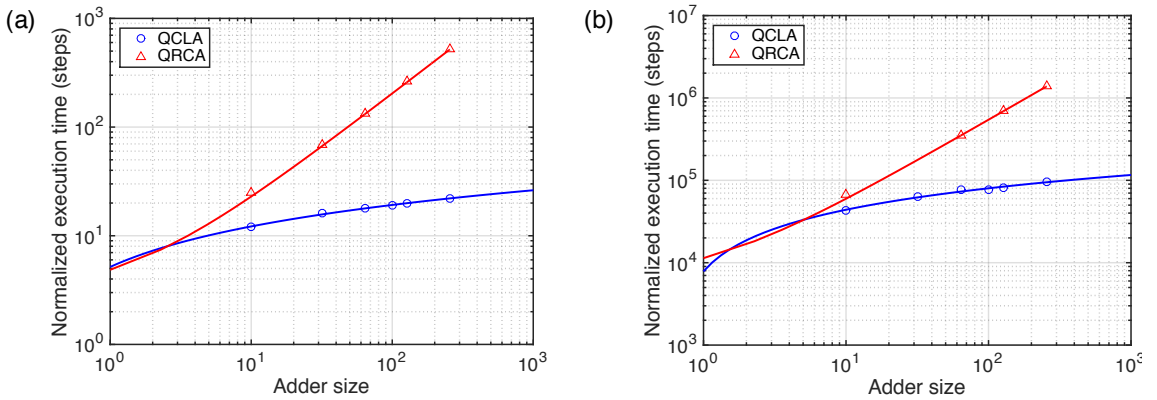


FIGURE 6.8: Simulation results of QRCA and QCLA circuits showing the execution time (a) without and (b) with FT encoding, in normalized units of the physical gate time.

6.5 Summary of the Performance Simulator

QUIPSIM is a software tool capable of simulating the performance of a complete set of fault tolerant QC protocols in the presence of faulty gates and low error rates. QUIPSIM tracks the error probability of each logical qubit over the course of the circuit by explicitly computing the number of fault paths that lead to erroneous outcomes of the FT circuit blocks. This approach provides a conservative estimate of the

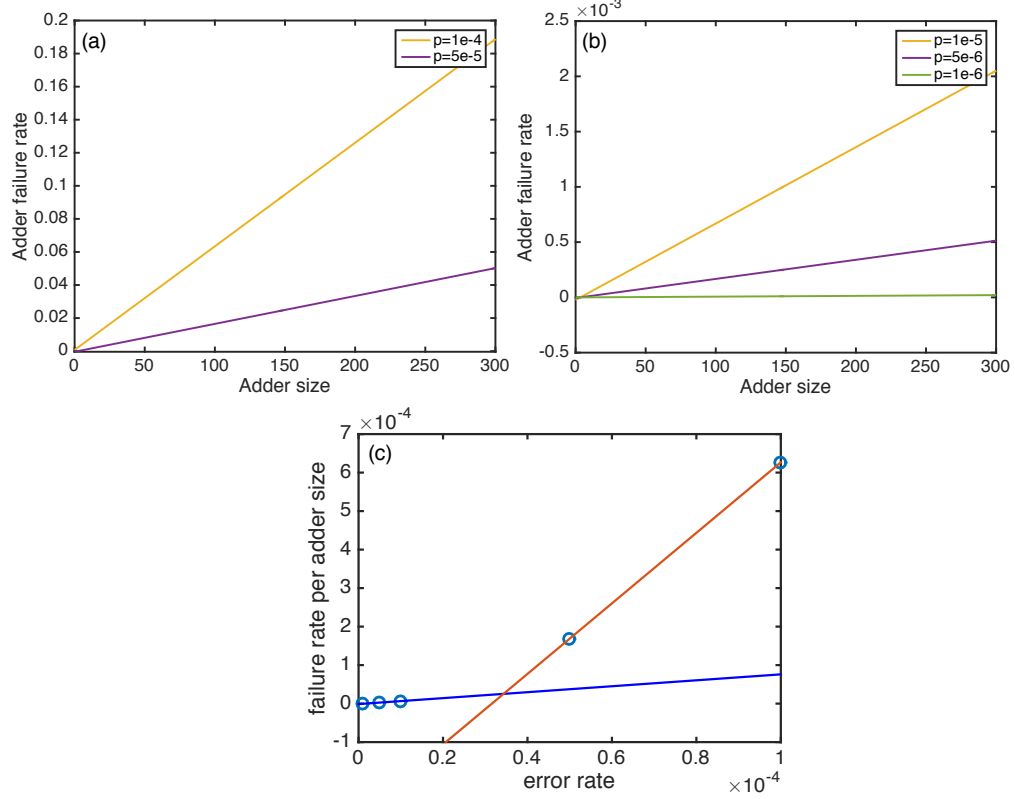


FIGURE 6.9: The overall adder failure probability for various physical error probability levels as a function of adder size for FT QCLA (a) above the threshold and (b) below the threshold. (c) The marginal failure probability defined as the change in the FT QCLA adder failure probability per bit size of the input numbers. The transition in the slope of the marginal failure probability per physical error rate shows the physical error rate below which implementing a FT adder becomes feasible.

error behavior of the overall circuit, but is very effective in low-error systems where other approaches like Monte-Carlo simulations take a very long time to converge. We used QUIPSIM to test the performance of two types of quantum adder circuits of various sizes, employing Steane code for the FT encoding.

While the results presented here are meant to highlight the generic properties of circuits, QUIPSIM also has the flexibility to add more realistic hardware models by defining the execution time and error probability for each gate type. We can further improve the FT protocol by utilizing a more efficient stabilizer measurement

processes. QUIPSIM can be used to study the relationship between physical gate parameters and the FT execution of a quantum circuit to optimize FT procedures. One such application has been presented in Sec. 6.2.4 by outlining how to perform a more efficient FT measurement operation in the Steane code. One limitation of the current QUIPSIM code is that the qubits are assumed to be fully connected. An important extension of this work will be to evaluate the performance of quantum circuits on physical hardware with added constraints like the limited connectivity of qubits and availability of resources, leading to the ability to optimize the hardware architecture of quantum processors based on actual system constraints.

7

Conclusions and Outlook

The field of trapped ion quantum computing has experienced tremendous progress over the last decade, and has demonstrated many of the necessary capabilities to be considered one of the leading candidates for realizing a quantum computer. Initial laboratory demonstrations of key protocols, including remote ion entanglement, high fidelity gates, and high fidelity readout have been shown during this time (Monroe and Kim, 2013). An experimental realization of a surface ion trap integrated with an optical cavity has been a longstanding goal in the field. The capabilities of such a system, including long range entanglement of ions and efficient qubit state detection, can provide order of magnitude improvements for several key quantum computing requirements. The work presented in this thesis is aimed at developing just such an enabling technology by demonstrating the functionality of a unique ion trap created on a mirror surface and the viability of small mode volume micromirror cavities.

The first part of this thesis, including Chapters 2 and 3, details the fabrication of a surface trap on a highly reflective UV mirror, the construction of the experimental apparatus needed for ion trapping, and the performance characterization of the ion trap towards its eventual use with an optical cavity. The mirror trap included an

extra set of RF electrodes (called the tweaker electrodes) which added the capability of fine tuning the ion's trap location to within several nanometers along all three trap axes. I have characterized one of the primary concerns of a mirror trap, which are the effects of the charging of the dielectric mirror surface. These results indicate that while charging may be a possible issue with the mirror trap, its eventual use for applications involving low UV exposure power for short time scales will mitigate the charging effects to the point where they do not affect the trap stability.

Chapters 4 and 5 of this thesis describe the construction of unique optical microcavities with the goal of achieving a small optical mode volume and strong coupling to ions trapped within the cavity. These chapters include detailed calculations of the expected cavity performance, experimental results from testing and optimization of the micromirror properties, and the development of a digital controller for cavity stabilization. The relative ease and repeatability of the micromirror fabrication process and the potential for strong coupling to trapped ions over a range of hundreds of microns in cavity length makes these micromirror cavities very advantageous when compared with the larger, traditional mirror cavities. Taken together, this work has shown the utility and effectiveness of these micromirrors for use as an optical cavity integrated with the mirror trap. As progress is made towards improving the surface quality and symmetry of these mirrors, we expect their performance to see significant improvements in the near future.

Finally, in Chapter 6, I take a much higher level view of the field of quantum computing and analyze what levels of qubit fidelity and quantum gate performance must be achieved in order to make quantum computing a practical reality. The field is now entering a stage where issues related to scalability and large scale system integration are coming to the forefront. To address some of these concerns, we have created a quantum computing performance simulator to predict the resource requirements and information fidelity of a large scale quantum computer executing

common fault tolerant protocols. Our simulation tool uses the approach of breaking down quantum circuits into smaller fault tolerant circuit blocks and defines a quantity called the logical fidelity to predict the reliability of the quantum information stored in logical qubits throughout the course of a computation. While the size of the quantum computers simulated with this tool is still well beyond the scope of what is currently realizable, our purpose with looking far ahead is to try and predict the requirements and limitations that a trapped ion quantum computer may ultimately have, and design the technologies of today to best meet those future challenges.

While we have not yet fully realized a complete cavity QED demonstration, the work we have done has set the foundation for such a system to be made in the near future. In fact, the results presented in this thesis have spurred a major effort to continue our approach towards utilizing optical cavities with surface traps. A new research program is currently under way in partnership with our collaborators at Sandia National Laboratories to utilize their world class clean room and microfabrication facilities for creating mirror ion traps based on our design. This future work will also use the micromirror cavity design we have developed, which offers several advantages over more conventional designs and has demonstrated a performance well suited for use with a mirror trap. The future plan for this experiment also calls for several new features to be added to our existing design to push the performance to even greater heights. Specifically, the next generation of cavity ion traps will be used in a low temperature environment inside a 4 K cryostat. This low temperature environment will reduce the ion heating rates and allow for the eventual integration of the ion trap and cavity with on chip superconducting single nanowire photon detectors. These are very high efficiency (up to 90%) single photon detectors which can be integrated directly below a mirror trap for potentially providing two orders of magnitude improvement in the photon detection efficiency of photons emitted by an ion inside the cavity. Much of this future work is already in the development

pipeline with the hopes of building a prototype system in the next one to two years. The continued progress of ion trap integration strategies and supporting technologies has the potential to enable the first generation of trapped ion quantum computers to exist in a matter of five to ten years. I expect the development of these devices to be driven by applications that harness the connectivity and reconfigurability of trapped ion qubits, for which optical cavities will play a significant role.

Appendix A

Digital PI Filter Code

```
// Does the math for PI(D) filter (D is not implemented)
module pid_filter2(clk , active , in , inready , out , outready ,
                     offset , pcoef , icoef , dc , e_in , out_prev );

input    clk ;           // clock
input    active;        // activate the Integral part
input    inready;        // input data ready pulse
input    [11:0] in ;      // ADC input
input    [15:0] dc;
input    [15:0] offset;   // offset for input signal
input    [23:0] pcoef;    // P coefficient
input    [23:0] icoef;    // I coefficient
output   [47:0] out;     // output
output reg [47:0] out_prev; // prev output accumulation
output reg     outready;   // output data ready pulse

wire    [24:0] k1;       //  $k_1 = pcoef + icoef$ ;  $k_2 = icoef$ 
output signed [47:0] e_in; // error input
reg signed  [47:0] e_prev;

subtractor sub(.dataa(offset), .datab({4'b0000, in}),
               .result(e_in));

assign k1 = pcoef + icoef;
assign out = out_prev + k1*e_in - pcoef*e_prev;
```

```
always @(posedge clk)
begin : activation
    case (active)
        1'b0: begin
            out_prev[32:17] <= dc;
        end
        1'b1: begin
            e_prev <= e_in;
            out_prev <= out;
        end
    endcase
end

endmodule
```

Bibliography

- Aharonov, D. and Ben-Or, M. (1997), “Fault-tolerant quantum computation with constant error,” in *Proc. Proceedings of the 29th Annual ACM Symposium on Theory of Computing*.
- Ahsan, M., Meter, R. V., and Kim, J. (2015), “Designing a Million-Qubit Quantum Computer Using a Resource Performance Simulator,” *J. Emerg. Technol. Comput. Syst.*, 12, 39:1–39:25.
- Aliferis, P., Gottesman, D., and Preskill, J. (2006), “Quantum Accuracy Threshold for Concatenated Distance 3 Quantum Codes,” *Journal of Quantum Information and Computation*, 6, 97–165.
- Awschalom, D. D., Bassett, L. C., Dzurak, A. S., Hu, E. L., and Petta, J. R. (2013), “Quantum Spintronics: Engineering and Manipulating Atom-Like Spins in Semiconductors,” *Science*, 339, 1174–1179.
- Bennett, C. and Brassard, G. (1984), “Quantum cryptography: Public key distribution and coin tossing,” in *Proceedings of IEEE International Conference on Computers, Systems and Signal Processing*, vol. 175, p. 8.
- Bennett, C. H., Brassard, G., Popescu, S., Schumacher, B., Smolin, J. A., and Wootters, W. K. (1996), “Purification of Noisy Entanglement and Faithful Teleportation via Noisy Channels,” *Phys. Rev. Lett.*, 76, 722–725.
- Berkeland, D. J., Miller, J. D., Bergquist, J. C., Itano, W. M., and Wineland, D. J. (1998), “Minimization of ion micromotion in a Paul trap,” *Journal of Applied Physics*, 83, 5025–5033.
- Black, E. D. (2001), “An introduction to Pound–Drever–Hall laser frequency stabilization,” *American Journal of Physics*, 69, 79–87.
- Burd, S. C., du Toit, P. J. W., and Uys, H. (2014), “Coupled optical resonance laser locking,” *Opt. Express*, 22, 25043–25052.
- Cetina, M., Bylinskii, A., Karpa, L., Gangloff, D., Beck, K. M., Ge, Y., Scholz, M., Grier, A. T., Chuang, I., and Vuletić, V. (2013), “One-dimensional array of ion chains coupled to an optical cavity,” *New Journal of Physics*, 15, 053001.

- Cirac, J. I., Blatt, R., Zoller, P., and Phillips, W. D. (1992), “Laser cooling of trapped ions in a standing wave,” *Phys. Rev. A*, 46, 2668–2681.
- Cirac, J. I., Blatt, R., Parkins, A. S., and Zoller, P. (1993), “Spectrum of resonance fluorescence from a single trapped ion,” *Phys. Rev. A*, 48, 2169–2181.
- Cirac, J. I., Garay, L. J., Blatt, R., Parkins, A. S., and Zoller, P. (1994), “Laser cooling of trapped ions: The influence of micromotion,” *Phys. Rev. A*, 49, 421–432.
- Colombe, Y., Steinmetz, T., Dubois, G., Linke, F., Hunger, D., and Reichel, J. (2007), “Strong atom-field coupling for Bose-Einstein condensates in an optical cavity on a chip,” *Nature*, 450, 272–276.
- Cross, A., DiVincenzo, D., and Terhal, B. (2009), “A comparative code study for quantum fault tolerance,” *Journal of Quantum Information and Computation*, 9, 541–572.
- Cuccaro, A., Draper, T. G., Kutin, S. A., and Moulton, D. P. (2004), “A new quantum ripple-carry addition circuit,” <http://arXiv.org/quant-ph/0410184>.
- Cui, G. and Raymer, M. G. (2005), “Quantum efficiency of single-photon sources in the cavity-QED strong-coupling regime,” *Opt. Express*, 13, 9660–9665.
- Dalibard, J. and Cohen-Tannoudji, C. (1985), “Dressed-atom approach to atomic motion in laser light: the dipole force revisited,” *J. Opt. Soc. Am. B*, 2, 1707–1720.
- Das, D., Barthwal, S., Banerjee, A., and Natarajan, V. (2005), “Absolute frequency measurements in Yb with 0.08 ppb uncertainty: Isotope shifts and hyperfine structure in the 399-nm $^1S_0 \rightarrow ^1P_1$ line,” *Phys. Rev. A*, 72, 032506.
- deLaubenfels, T. E., Burkhardt, K. A., Vittorini, G., Merrill, J. T., Brown, K. R., and Amini, J. M. (2015), “Modulating carrier and sideband coupling strengths in a standing-wave gate beam,” *Phys. Rev. A*, 92, 061402.
- DeVoe, R. G., Hoffnagle, J., and Brewer, R. G. (1989), “Role of laser damping in trapped ion crystals,” *Phys. Rev. A*, 39, 4362–4365.
- Devoret, M. H. and Schoelkopf, R. J. (2013), “Superconducting Circuits for Quantum Information: An Outlook,” *Science*, 339, 1169–1174.
- Diedrich, F., Bergquist, J. C., Itano, W. M., and Wineland, D. J. (1989), “Laser Cooling to the Zero-Point Energy of Motion,” *Phys. Rev. Lett.*, 62, 403–406.
- DiVincenzo, D. P. and Aliferis, P. (2007), “Effective Fault-Tolerant Quantum Computation with Slow Measurements,” *Phys. Rev. Lett.*, 98, 020501.

- Draper, T. G. (2000), “Addition on a Quantum Computer,” <http://arXiv.org/quantph/0008033>.
- Draper, T. G., Kutin, S. A., Rains, E. M., and Svore, K. M. (2006), “A Logarithmic-depth Quantum Carry-lookahead Adder,” *Quantum Info. Comput.*, 6, 351–369.
- Fox, A. G. and Li, T. (1968), “Computation of Optical Resonator Modes by the Method of Resonance Excitation,” *IEEE Journal of Quantum Electronics*, QE-4, 460–465.
- Gallego, J., Ghosh, S., Alavi, S. K., Alt, W., Martinez-Dorantes, M., Meschede, D., and Ratschbacher, L. (2016), “High-finesse fiber Fabry–Perot cavities: stabilization and mode matching analysis,” *Applied Physics B*, 122, 1–14.
- Gloger, T. F., Kaufmann, P., Kaufmann, D., Baig, M. T., Collath, T., Johanning, M., and Wunderlich, C. (2015), “Ion-trajectory analysis for micromotion minimization and the measurement of small forces,” *Phys. Rev. A*, 92, 043421.
- Gossett, P. (1998), “Quantum carry-save arithmetic,” <http://arXiv.org/quantph/9808061v2>.
- Gottesman, D. (1998), “Theory of fault-tolerant quantum computation,” *Phys. Rev. A*, 57, 127–137.
- Grover, L. K. (1997), “Quantum Mechanics Helps in Searching for a Needle in a Haystack,” *Phys. Rev. Lett.*, 79, 325–328.
- Gulde, S., Riebe, M., Lancaster, G. P. T., Becher, C., Eschner, J., Haffner, H., Schmidt-Kaler, F., Chuang, I. L., and Blatt, R. (2003), “Implementation of the Deutsch-Jozsa algorithm on an ion-trap quantum computer,” *Nature*, 421, 48–50.
- Harlander, M., Brownnutt, M., Hänsel, W., and Blatt, R. (2010), “Trapped-ion probing of light-induced charging effects on dielectrics,” *New Journal of Physics*, 12, 093035.
- Herskind, P. F., Wang, S. X., Shi, M., Ge, Y., Cetina, M., and Chuang, I. L. (2011), “Microfabricated surface ion trap on a high-finesse optical mirror,” *Opt. Lett.*, 36, 3045–3047.
- Hood, C. J., Kimble, H. J., and Ye, J. (2001), “Characterization of high-finesse mirrors: Loss, phase shifts, and mode structure in an optical cavity,” *Phys. Rev. A*, 64, 033804.
- Horak, P., Klappauf, B. G., Albrecht Haase, R. F., Schmiedmayer, J., Domokos, P., and Hinds, E. A. (2003), “Possibility of single-atom detection on a chip,” *Physical Review A*, 67.

- Hucul, D., Inlek, I. V., Vittorini, G., Crocker, C., Debnath, S., Clark, S. M., and Monroe, C. (2015), “Modular entanglement of atomic qubits using photons and phonons,” *Nat Phys*, 11, 37–42.
- Hunger, D., Steinmetz, T., Colombe, Y., Deutsch, C., Hänsch, T. W., and Reichel, J. (2010), “A fiber Fabry–Perot cavity with high finesse,” *New Journal of Physics*, 12, 065038.
- Itano, W. M., Bergquist, J. C., Bollinger, J. J., and Wineland, D. J. (1995), “Cooling methods in ion traps,” *Physica Scripta*, 1995, 106.
- Keller, J., Partner, H. L., Burgermeister, T., and Mehlstäubler, T. E. (2015), “Precise determination of micromotion for trapped-ion optical clocks,” *Journal of Applied Physics*, 118.
- Keller, M., Lange, B., Hayasaka, K., Lange, W., and Walther, H. (2004), “Continuous generation of single photons with controlled waveform in an ion-trap cavity system,” *Nature*, 431, 1075–1078.
- Kim, T., Maunz, P., and Kim, J. (2011a), “Efficient collection of single photons emitted from a trapped ion into a single-mode fiber for scalable quantum-information processing,” *Phys. Rev. A*, 84, 063423.
- Kim, T. H., Herskind, P. F., and Chuang, I. L. (2011b), “Surface-electrode ion trap with integrated light source,” *Applied Physics Letters*, 98.
- Kimble, H. J. (2008), “The quantum internet,” *Nature*, 453, 1023–1030.
- Kok, P., Munro, W. J., Nemoto, K., Ralph, T. C., Dowling, J. P., and Milburn, G. J. (2007), “Linear optical quantum computing with photonic qubits,” *Rev. Mod. Phys.*, 79, 135–174.
- Kreuter, A., Becher, C., Lancaster, G. P. T., Mundt, A. B., Russo, C., Häffner, H., Roos, C., Eschner, J., Schmidt-Kaler, F., and Blatt, R. (2004), “Spontaneous Emission Lifetime of a Single Trapped Ca^+ Ion in a High Finesse Cavity,” *Phys. Rev. Lett.*, 92, 203002.
- Ladd, T. D., Jelezko, F., Laflamme, R., Nakamura, Y., Monroe, C., and O’Brien, J. L. (2010), “Quantum computers,” *Nature*, 464, 45–53.
- Langer, C., Ozeri, R., Jost, J. D., Chiaverini, J., DeMarco, B., Ben-Kish, A., Blakestad, R. B., Britton, J., Hume, D. B., Itano, W. M., Leibfried, D., Reichle, R., Rosenband, T., Schaetz, T., Schmidt, P. O., and Wineland, D. J. (2005), “Long-Lived Qubit Memory Using Atomic Ions,” *Phys. Rev. Lett.*, 95, 060502.

- Lanyon., B., Whitfield, J. D., Gillett, G. G., Goggin, M. E., Almeida, M. P., Kassal, I., Biamonte, J. D., Mohseni, M., Powell, B. J., Barbieri, M., Aspuru-Guzik, A., and White, A. G. (2010), “Towards quantum chemistry on a quantum computer,” *Nat Chem*, 2, 106–111.
- Law, C. K. and Kimble, H. J. (1997), “Deterministic generation of a bit-stream of single-photon pulses,” *Journal of Modern Optics*, 44, 2067–2074.
- Lee, M. W., Jarratt, M. C., Marciniak, C., and Biercuk, M. J. (2014), “Frequency stabilization of a 369 nm diode laser by nonlinear spectroscopy of Ytterbium ions in a discharge,” *Opt. Express*, 22, 7210–7221.
- Leibfried, D., Blatt, R., Monroe, C., and Wineland, D. (2003), “Quantum dynamics of single trapped ions,” *Rev. Mod. Phys.*, 75, 281–324.
- Littman, M. G. and Metcalf, H. J. (1978), “Spectrally narrow pulsed dye laser without beam expander,” *Appl. Opt.*, 17, 2224–2227.
- Marsili, F., Verma, V. B., Stern, J. A., Harrington, S., Lita, A. E., Gerrits, T., Vayshenker, I., Baek, B., Shaw, M. D., Mirin, R. P., and Nam, S. W. (2013), “Detecting single infrared photons with 93% system efficiency,” *Nat Photon*, 7, 210–214.
- Maunz, P., Moehring, D. L., Olmschenk, S., Younge, K. C., Matsukevich, D. N., and Monroe, C. (2007), “Quantum interference of photon pairs from two remote trapped atomic ions,” *Nat Phys*, 3, 538–541.
- Merrill, J. T., Volin, C., Landgren, D., Amini, J. M., Wright, K., Doret, S. C., Pai, C.-S., Hayden, H., Killian, T., Faircloth, D., Brown, K. R., Harter, A. W., and Slusher, R. E. (2011), “Demonstration of integrated microscale optics in surface-electrode ion traps,” *New Journal of Physics*, 13, 103005.
- Metcalf, H. J. and van der Straten, P. (1999), *Laser Cooling and Trapping*, Springer Science+Business Media.
- Meter, R. V. and Oskin, M. (2006), “Architectural Implications of Quantum Computing Technologies,” *J. Emerg. Technol. Comput. Syst.*, 2, 31–63.
- Metodi, T. S., Thaker, D. D., Cross, A. W., Chong, F. T., and Chuang, I. L. (2006), “Scheduling physical operations in a quantum information processor,” in *Proceedings of SPIE*, 6244:62440T.
- Millo, J., Magalhães, D. V., Mandache, C., Le Coq, Y., English, E. M. L., Westergaard, P. G., Lodewyck, J., Bize, S., Lemonde, P., and Santarelli, G. (2009), “Ultradurable lasers based on vibration insensitive cavities,” *Phys. Rev. A*, 79, 053829.

- Moehrung, D. L., Maunz, P., Olmschenk, S., Younge, K. C., Matsukevich, D. N., Duan, L. M., and Monroe, C. (2007), “Entanglement of single-atom quantum bits at a distance,” *Nature*, 449, 68–71.
- Monroe, C. and Kim, J. (2013), “Scaling the Ion Trap Quantum Processor,” *Science*, 339, 1164–1169.
- Monroe, C., Raussendorf, R., Ruthven, A., Brown, K. R., Maunz, P., Duan, L.-M., and Kim, J. (2014), “Large-scale modular quantum-computer architecture with atomic memory and photonic interconnects,” *Phys. Rev. A*, 89, 022317.
- Monz, T., Kim, K., Hänsel, W., Riebe, M., Villar, A. S., Schindler, P., Chwalla, M., Hennrich, M., and Blatt, R. (2009), “Realization of the Quantum Toffoli Gate with Trapped Ions,” *Phys. Rev. Lett.*, 102, 040501.
- Monz, T., Nigg, D., Martinez, E. A., Brandl, M. F., Schindler, P., Rines, R., Wang, S. X., Chuang, I. L., and Blatt, R. (2016), “Realization of a scalable Shor algorithm,” *Science*, 351, 1068–1070.
- Mount, E., Kabytayev, C., Crain, S., Harper, R., Baek, S.-Y., Vrijen, G., Flammia, S. T., Brown, K. R., Maunz, P., and Kim, J. (2015), “Error compensation of single-qubit gates in a surface-electrode ion trap using composite pulses,” *Phys. Rev. A*, 92, 060301.
- Nielsen, M. A. and Chuang, I. L. (2000), *Quantum Computation and Quantum Information*, Cambridge University Press.
- Noek, R., Vrijen, G., Gaultney, D., Mount, E., Kim, T., Maunz, P., and Kim, J. (2013a), “High speed, high fidelity detection of an atomic hyperfine qubit,” *Opt. Lett.*, 38, 4735–4738.
- Noek, R., Kim, T., Mount, E., Baek, S.-Y., Maunz, P., and Kim, J. (2013b), “Trapping and cooling of $^{174}\text{Yb}^+$ ions in a microfabricated surface trap,” *Journal of the Korean Physical Society*, 63, 907–913.
- Olmschenk, S., Younge, K. C., Moehrung, D. L., Matsukevich, D. N., Maunz, P., and Monroe, C. (2007a), “Manipulation and detection of a trapped Yb^+ hyperfine qubit,” *Phys. Rev. A*, 76, 052314.
- Olmschenk, S., Younge, K. C., Moehrung, D. L., Matsukevich, D. N., Maunz, P., and Monroe, C. (2007b), “Manipulation and detection of a trapped Yb^+ hyperfine qubit,” *Phys. Rev. A*, 76, 052314.
- Petrak, B., Konthasinghe, K., Perez, S., and Muller, A. (2011), “Feedback-controlled laser fabrication of micromirror substrates,” *Review of Scientific Instruments*, 82.

- Petta, J. R., Johnson, A. C., Taylor, J. M., Laird, E. A., Yacoby, A., Lukin, M. D., Marcus, C. M., Hanson, M. P., and Gossard, A. C. (2005), “Coherent Manipulation of Coupled Electron Spins in Semiconductor Quantum Dots,” *Science*, 309, 2180–2184.
- Purcell, E. M. (1946), “Spontaneous emission probabilities at radio frequencies,” *Phys. Rev.*, 69, 681.
- Rosenband, T., Hume, D. B., Schmidt, P. O., Chou, C. W., Brusch, A., Lorini, L., Oskay, W. H., Drullinger, R. E., Fortier, T. M., Stalnaker, J. E., Diddams, S. A., Swann, W. C., Newbury, N. R., Itano, W. M., Wineland, D. J., and Bergquist, J. C. (2008), “Frequency Ratio of Al+ and Hg+ Single-Ion Optical Clocks; Metrology at the 17th Decimal Place,” *Science*, 319, 1808–1812.
- Saleh, B. E. and Teich, M. C. (2007), *Fundamentals of Photonics*, John Wiley & Sons, Inc., second edn.
- Shor, P. (1994), “Algorithms for quantum computation:Discrete logarithms and factoring,” in *Proceedings of the 35th Annual Symposium on Foundations of Computer Science*, ed. S. Goldwasser, pp. 124–134, Los Alamitos, CA., IEEE Computer Society Press.
- Siegman, A. E. (1986), *Lasers*, University Science Books.
- Simon, C. and Irvine, W. T. M. (2003), “Robust Long-Distance Entanglement and a Loophole-Free Bell Test with Ions and Photons,” *Phys. Rev. Lett.*, 91, 110405.
- Siversen, J. D., Simkins, L. R., Weidt, S., and Hensinger, W. K. (2012), “On the application of radio frequency voltages to ion traps via helical resonators,” *Applied Physics B*, 107, 921–934.
- Stajic, J. (2013), “The Future of Quantum Information Processing,” *Science*, 339, 1163–1163.
- Steane, A. M. (1996), “Error Correcting Codes in Quantum Theory,” *Phys. Rev. Lett.*, 77, 793–797.
- Steane, A. M. (2003), “Overhead and noise threshold of fault-tolerant quantum error correction,” *Phys. Rev. A*, 68, 042322.
- Steane, A. M. and Rieffel, E. G. (2000), “Beyond bits: the future of quantum information processing,” *Computer*, 33, 38–45.
- Steiner, M., Meyer, H. M., Deutsch, C., Reichel, J., and Köhl, M. (2013), “Single Ion Coupled to an Optical Fiber Cavity,” *Phys. Rev. Lett.*, 110, 043003.

- Tanaka, U., Masuda, K., Akimoto, Y., Koda, K., Ibaraki, Y., and Urabe, S. (2011), “Micromotion compensation in a surface electrode trap by parametric excitation of trapped ions,” *Applied Physics B*, 107, 907–912.
- Van Meter, R. and Itoh, K. M. (2005), “Fast quantum modular exponentiation,” *Phys. Rev. A*, 71, 052320.
- Van Rynbach, A., Todo, S., and Trebst, S. (2010), “Orbital Ordering in e_g Orbital Systems: Ground States and Thermodynamics of the 120° Model,” *Phys. Rev. Lett.*, 105, 146402.
- VanDevender, A. P., Colombe, Y., Amini, J., Leibfried, D., and Wineland, D. J. (2010), “Efficient Fiber Optic Detection of Trapped Ion Fluorescence,” *Phys. Rev. Lett.*, 105, 023001.
- Williams, C. J. (2004), “Neutral atom quantum computing,” in *Frontiers in Optics 2004*, p. FMI4, Optical Society of America.
- Wineland, D. J., Dalibard, J., and Cohen-Tannoudji, C. (1992), “Sisyphus cooling of a bound atom,” *J. Opt. Soc. Am. B*, 9, 32–42.
- Zhou, X., Leung, D. W., and Chuang, I. L. (2000), “Methodology for quantum logic gate construction,” *Phys. Rev. A*, 62, 052316.

Biography

Andre Jan Simoes Van Rynbach was born in Huntington, NY on August 20, 1985. After graduating from Providence High School in Charlotte, NC in 2003, he went on to attend Cornell University from August 2003 to June 2007. During his time at Cornell, he earned a Bachelor of Arts degree Cum Laude in Mathematics and Magna Cum Laude in Physics, and earned the Kieval Prize for the top undergraduate student in the physics department. After graduation, he moved to Santa Barbara, CA to attend a graduate program in Physics at UC Santa Barbara. There he spent time learning to surf, rock climbing, and studying theoretical condensed matter physics. His work on the study of phase transitions in transition metal oxides resulted in a publication (Van Rynbach et al., 2010). After completing his Master of Arts degree in Physics from UCSB in 2010, he moved to Duke University to begin a Ph.D. program in the Electrical and Computer Engineering Department under the direction of Professor Jungsang Kim, which he completed in May 2016. While at Duke he did research in the field of trapped ion quantum computing, and was awarded the ECE Department's Charles R. Vail Memorial Outstanding Teaching Award for the academic year 2012-13. Outside of his work in the lab, he enjoys spending time with family, hiking, and playing ice hockey as a goaltender.